From Signalling to Cell Behaviour: Modelling Multi-Scale Organization in Single and Collective Cellular Systems

by

Cole Zmurchok

B.Sc., University of Alberta, 2012

M.Sc., University of Alberta, 2014

A THESIS SUBMITTED IN PARTIAL FULFILLMENT
OF THE REQUIREMENTS FOR THE DEGREE OF

Doctor of Philosophy

in

THE FACULTY OF GRADUATE AND POSTDOCTORAL STUDIES
(Mathematics)

The University of British Columbia
(Vancouver)

July 2018

The following individuals certify that they have read, and recommend to the Faculty of Graduate and Postdoctoral Studies for acceptance, the dissertation entitled:

From Signalling to Cell Behaviour: Modelling Multi-Scale Organization in Single and Collective Cellular Systems

submitted by Cole Zmurchok in partial fulfillment of the requirements of the degree of

Doctor of Philosophy in Mathematics

Examining Committee:

Leah Edelstein-Keshet, Mathematics (Supervisor)
Eric Cytrynbaum, Mathematics (Supervisory Committee Member)
Andrew Rechnitzer, Mathematics (University Examiner)
Geoffrey Wasteneys, Botany (University Examiner)

Additional Supervisory Committee Members:

James J. Feng, Mathematics (Supervisory Committee Member)

Abstract

Individually and collectively, cells are organized systems with many interacting parts. Mathematical models allow us to infer behaviour at one level of organization from information at another level. In this thesis, I explore two biological questions that are answered through the development of new mathematical approaches and novel models.

(1) Molecular motors are responsible for transporting material along molecular tracks (microtubules) in cells. Typically, transport is described by a system of reaction-advection-diffusion partial differential equations (PDEs). Recently, quasi-steady-state (QSS) methods have been applied to models with linear reactions to approximate the behaviour of the PDE system. To understand how nonlinear reactions affect the overall transport process at the cellular level, I extend the QSS approach to certain nonlinear reaction models, reducing the full PDE system to a single nonlinear PDE. I find that the approximating PDE is a conservation law for the total density of motors within the cell, with effective diffusion and velocity that depend nonlinearly on the motor densities and model parameters. Cell-scale predictions about the organization and distribution of motors can be drawn from these effective parameters.

(2) Rho GTPases are a family of protein regulators that modulate cell shape and forces exerted by cells. Meanwhile, cells sense forces such as tension. The implications of this two-way feedback on cell behaviour is of interest to biologists. I explore this question by developing a simple mathematical model for GTPase signalling and cell mechanics. The model explains a spectrum of behaviours, including relaxed or contracted cells and cells that oscillate between these extremes. Through bifurcation analysis, I find that changes in single cell behaviour can be explained by the strength of feedback from tension to signalling. When such model cells are connected to one another in a row or in a 2D sheet, waves of contraction/relaxation propagate through the tissue. Model predictions are qualitatively consistent with developmental-biology observations such as the volume fluctuations in a cellular monolayer. The model suggests a mechanism for the organization of tissue-scale behaviours from signalling and mechanics, which could be extended to specific experimental systems.

Lay Summary

Cells are complex systems with many interacting parts. Multi-scale mathematical models are used to explore how organization emerges from constituent parts. I answer two biological questions by developing a new approximation method and by formulating a novel model.

In order to distribute cellular cargo, cells employ proteins called molecular motors for transport. The interactions and movement of motors within a cell is described using a system of partial differential equations. To more easily understand and determine the effect of nonlinear interactions on the overall transport of cargo, I develop a new approximation method to reduce the system of equations to a single equation.

Protein signalling is responsible for controlling cell size, and can also be affected by mechanical tension experienced by a cell. I develop a new model incorporating the two-way feedback between cell signalling to cell mechanics to explore and explain single and collective cell behaviours observed in experiments.

Preface

Chapter 1 and Chapter 4 were written by the author, Cole Zmurchok, for the purposes of this thesis.

Chapter 2 and Appendix A are based on the published work by Zmurchok, Small, Ward, and Edelstein-Keshet [106], of which I am the first author. I supervised Tim Small, who was an undergraduate research assistant involved in the computational and mathematical analysis in the early stages of this project. Michael Ward and Leah Edelstein-Keshet are joint supervisors for this project, and assisted in writing parts of the paper. I performed the research and wrote the paper under their supervision. Michael Ward suggested the numerical shooting scheme and used this method to produce figures, and performed the boundary layer analysis.

Chapter 3 and Appendix B is based on published work by Zmurchok, Bhaskar, and Edelstein-Keshet [107], of which I am the first author. Dhananjay Bhaskar was involved in the 2D implementation of the model using the cellular Potts framework (CPM), and is responsible for producing the figures using the CPM. I collaborated with Dhananjay Bhaskar throughout this process, and we worked closely to adapt, implement, and code the 2D implementation (including the Kuramoto order parameter study). I supervised Jim Shaw, an undergraduate research volunteer, who was responsible for performing an additional numerical bifurcation analysis of the Rac-Rho-tension model. Leah Edelstein-Keshet supervised the research and assisted in writing the paper.

Table of Contents

List of Figures

Glossary

BC boundary condition

CPM Cellular Potts model

FP Fokker-Planck

IVP initial value problem

IBVP initial-boundary value problem

MCS Monte-Carlo step

MT Microtubule

ODE ordinary differential equation

PDE partial differential equation

QSS quasi-steady-state

Acknowledgments

I would like to thank and acknowledge Leah Edelstein-Keshet for her continued mentorship and constant encouragement. Thank you, Leah. I am certain that your lessons and guidance will have an even greater and lasting impact in the coming years.

I would like to thank the many members of the UBC math biology, applied math, and math education community. I would especially like to thank Michael Ward for his mentorship and guidance, and Eric Cytrynbaum and Jimmy Feng for their mentorship and help as members of my supervisory committee. I would also like to acknowledge the members of the Keshet-Feng research group for their questions, suggestions, and for weekly group meetings.

for Annie

Chapter 1

Introduction

1.1 Multi-scale Modelling in Cellular Systems

The broad question that this thesis aims to address is how biological mechanisms combine to organize cell behaviours. Biological experiments and observations, allow for us to understand the mechanisms, facts, and theories about how various proteins, molecular motors, cell signalling molecules, and biophysical structures interact with each other. Multi-scale modelling and analysis from applied mathematics can serve as a tool for understanding how cell-scale or tissue-scale organization emerges from the interactions of the many different constituent parts.

This thesis is divided into two self-contained parts, Chapter 2 and Chapter 3. Each part describes a different example of multi-scale modelling in cell biology and utilizes different mathematical approaches. In this introduction, I provide context and background for each part with respect to the broader field, and preview the main questions, methods, and results. I end the introduction with a brief description of the thesis contents.

1.2 Intracellular Transport by Molecular Motors

In many cellular scenarios, diffusion alone is insufficient to transport cargo over the distances required to maintain cellular function. This is especially important when cargo needs to be transported over long distances, such as in neurons or fungal cells (Figure 1.1(a)). For a neuron to function, it is necessary to transport cargo over a long distance from the cell body down the axon to the synapses. In fungi, it is necessary to transport cargo to maintain and expand the cell wall during growth. Figure 1.1(b)–(c) depicts the distribution of cargo in both yeast-like and hyphal fungi cells in green against the cell membrane in red. In both neurons and fungi, the transport of cargo is mediated by proteins called molecular motors. Molecular motors are proteins that utilize energy in order to transport cargo by "walking"

along cellular "tracks". Molecular motors typically transport cargo in vesicles and move along protein filaments of the cytoskeleton (as in Figure 1.1(d)). Cytoskeletal filaments such as microtubules (MTs) or actin filaments give a cell structure and provide roads for the molecular motors to use [10]. Microtubules and actin filaments are asymmetric filaments with distinct "plus" and "minus" ends.

Different types of molecular motors such as kinesin, dynein, and myosin motors have different biophysical properties. For example, kinesin motors, which largely walk towards the plus ends of polarized MTs can also exist as unbound, cytosolic forms [5]. Dynein motors walk towards the minus ends of MTs. Motors may also be present in complexes, where more than one motor of any type can be bound to cargo. Myosin motors walk on actin filaments instead of MTs, and are mostly associated with muscle contraction. Some myosin motors are responsible for transporting cellular cargo [86, 101]. The interactions of many molecular motors, the protein filaments that they move along, and other cellular factors result in cell-scale distribution of molecular motors (and/or cargo).

Nonetheless, it is difficult to understand how a variation in a particular biophysical parameter will affect the cell-scale motor distribution in such a complicated system, more so if nonlinear effects are important. Many mathematical approaches have had success understanding the transport phenomena at different scales, e.g., several motors attached to a single cargo [4, 31, 40, 48, 55] or at the cell-scale using stochastic or partial differential equation approaches [11, 66, 72, 85]. A system of reaction-advection-diffusion partial differential equation (PDE) is often used to quantitatively describe transport by molecular motors within cells [16, 26, 58]. To understand the effect of parameters in such a system, I develop an approximation method to reduce the dimensionality of the system and reveal how the effective transport parameters depend on the biophysical parameters of the molecular motors. The approximation method relies on existence of two separate time-scales in the system: fast binding, unbinding and other reaction interactions, but slow spatial processes and conservation of molecular motors. Using methods from asymptotic analysis, I find a quasi-steady-state PDE, which acts as an approximation to the full reaction-advection-diffusion system.

The quasi-steady-state (QSS) approximation developed here extends the methods of Newby and Bressloff [58] and Bressloff and Newby [7], who primarily developed and used the quasi-steady-state approximation to determine the mean first passage time for molecular motor intermittent search, i.e., the average time for cargo to be transported to a specific cellular site by motors. From a PDE transport model for early endosome organization in fungal hyphae [26] with linear state transitions, Dauvergne and Edelstein-Keshet [16] utilized quasi-steady-state approximation methods to determine the effective velocity and effective diffusion parameters which describe the overall transport process. A limitation of

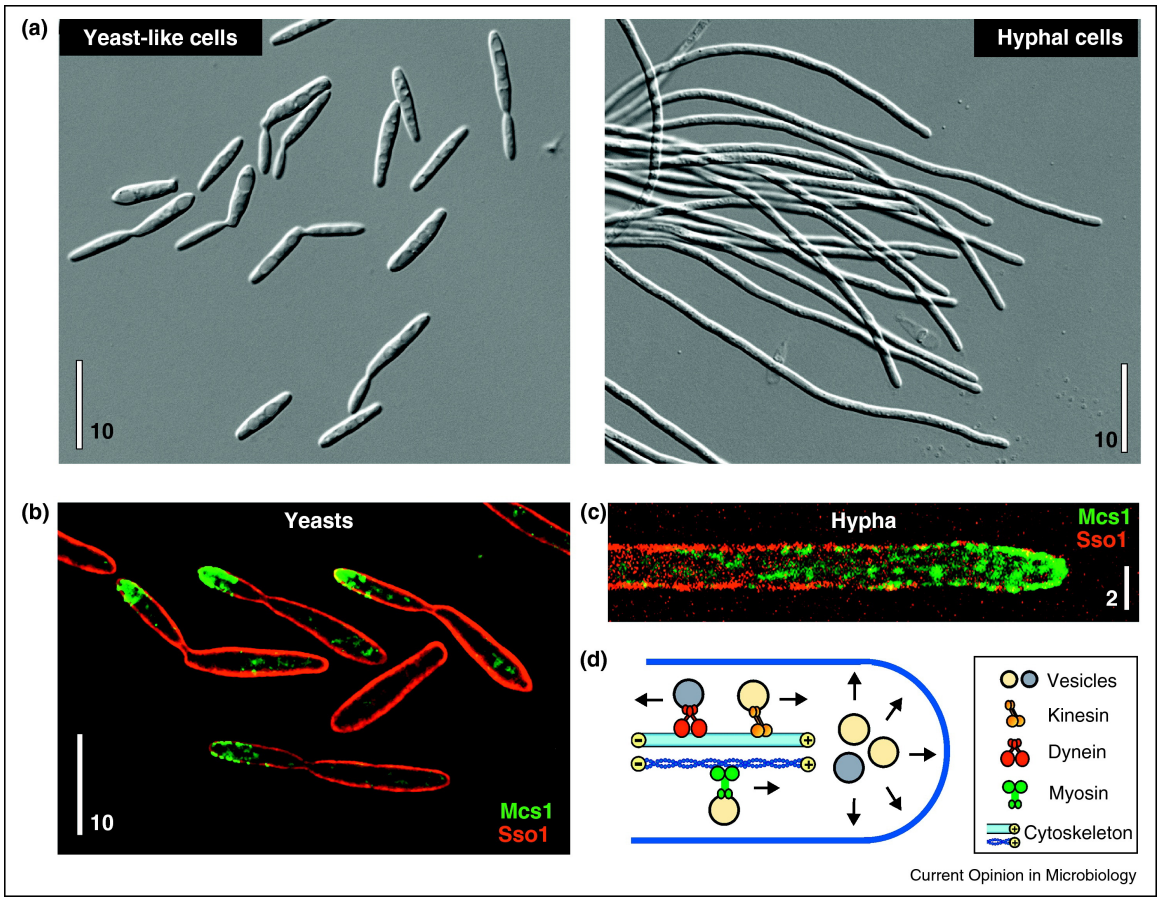

Figure 1.1: An overview of how molecular motor based intracellular transport supports growth in fungi. In (a), the two main growth modes of fungi are shown: yeast-like cells and filamentous fungi. In (b)–(c), the cell membrane is shown in red, while myosin motors transporting material necessary for the construction of the cell wall is shown in green. In (d), the roles of molecular motors and cytoskeleton are illustrated. Molecular motors are responsible for transporting vesicles containing cargo. Reprinted from Current Opinion in Microbiology, 14, Gero Steinberg, Motors in fungal morphogenesis: cooperation versus competition, 660–667, Copyright 2011, with permission from Elsevier.

this approach is that the methodology only applies to linear state transitions. Nonlinear interactions may be better motivated in some biological situations. For example, rates of motor binding to microtubules could be limited by competition for binding sites, or could be cooperative. Mass-action kinetics or other nonlinear interactions, such as "traffic-jam" cubic nonlinearities could play an important role in the organization of the transport process [102]. Here, I extend the quasi-steady-state methods from Newby and Bressloff [58] and Dauvergne and Edelstein-Keshet [16] to a class of models with nonlinear reaction kinetics.

I apply the QSS methodology to three different transport systems. These models consist

of (1) a model for kinesin motors with a saturating binding rate, (2) a model for kinesin-dynein-cargo complexes whose interactions on a microtubule can change the direction of transport, and (3) a model for unconventional myosin motors that stop moving (stall) upon encountering other stalled motors. Although the motors move at known speeds, I show that their interactions with MTs and each other lead to slower overall effective "speed" (transport rate) as well as spread (similar to diffusion) in their spatial distribution. The biological contribution is that I am able to relate the effective rate of transport and diffusion to the details of binding, MT polarity and nonlinear motor interactions. Mathematically, this manifests through a scalar conservation law for the density of motors within the cell, parametrized in terms of the density of motors in one of the states, e.g., the freely diffusing state. In this so-called "QSS PDE", the flux determines an effective velocity and effective diffusion coefficient that depend nonlinearly on the biophysical parameters and the motor density. From the effective velocity and effective diffusion, the overall cell-scale transport can be understood as a function of the motor-scale model parameters.

In the next section, I provide a short mathematical primer on the ideas behind the quasi-steady-state approximation.

1.2.1 A Primer on Quasi-steady-state Methods

The main mathematical idea behind the quasi-steady-state approximation is the notion of separation of time-scales. In a dynamical system, the time-scale associated with one variable or process may be slower than that of others. Consider, for example, the following ordinary differential equation (ODE) system for two species $u(t)$ and $v(t)$:

$$\frac{du}{dt} = f(u, v), \tag{1.1}$$

$$\frac{dv}{dt} = \frac{1}{\varepsilon}(v - a), \tag{1.2}$$

where f is some function describing the rate of change of u, a is the steady-state of species v, and $0 < \varepsilon \ll 1$ is a small parameter so that $\frac{1}{\varepsilon} \gg 1$ is large. Provided that the function f is not small, i.e., $f = \mathcal{O}(1)$, then u varies on a time-scale much faster than v. The details of the contribution of various terms in the dynamical system should be obtained through careful non-dimensionalization. As such, the quasi-steady-state approximation is

$$v \approx a \tag{1.3}$$

since v rapidly relaxes to its steady-state a. From this approximation, it is possible to study only the reduced system, which has fewer dynamical variables:

$$\frac{du}{dt} = f(u, a). \tag{1.4}$$

Theoretically, the parameter dependence of solutions $u(t)$ on a could be more easily deduced. This is the main idea behind the derivation of classical Michaelis-Menten kinetics (see [83] for a careful case study or Chapter 7 of [22] for an overview).

To illustrate the utility of the QSS approximation in a cellular context and to explain the utility of the approximation, I will discuss a variant of the QSS approximation from Marée et al. [49]. In this work, the authors use a multi-scale modelling approach to understand cell polarization and movement. In part of the model, regulatory proteins are found to bind and unbind from the cytosol onto the cell membrane, and the diffusion coefficients for proteins in either state are different—membrane bound proteins diffuse more slowly than in the cytosol. Owing to the fact that switching between the states is rapid, the authors use a QSS approximation to describe the effective diffusion of the protein. I review part of their approximation below.

Let $G_{\mathrm{C}}(x,t)$ and $G_{\mathrm{M}}(x,t)$ be the amounts of regulatory proteins in the cytosolic and membrane-bound states, respectively, and $G(x,t) = G_{\mathrm{C}}(x,t) + G_{\mathrm{M}}(x,t)$ the amount at spatial location x. Suppose that the cytosolic proteins bind to the membrane with rate coefficient k_{on} and unbind with rate coefficient k_{off}, and that the two classes of proteins have different diffusion coefficients, D_{C} and D_{M}, respectively. This scenario is illustrated in Figure 1.2.

For simplicity, consider a 1D geometry, i.e., $x \in \mathbb{R}$, with no-flux boundary conditions at either end of the cell. In this case, the dynamics of the proteins can be captured by the following reaction-diffusion system of partial differential equations:

$$\frac{\partial G_{\mathrm{M}}}{\partial t} = D_{\mathrm{M}} \frac{\partial^2 G_{\mathrm{M}}}{\partial x^2} + k_{\mathrm{on}} G_{\mathrm{C}} - k_{\mathrm{off}} G_{\mathrm{M}}, \tag{1.5}$$

$$\frac{\partial G_{\mathrm{C}}}{\partial t} = D_{\mathrm{C}} \frac{\partial^2 G_{\mathrm{C}}}{\partial x^2} - k_{\mathrm{on}} G_{\mathrm{C}} + k_{\mathrm{off}} G_{\mathrm{M}}. \tag{1.6}$$

Note that the total amount of protein within the entire cell is conserved by these equations, given no-flux boundary conditions, and that the proteins can only transition between the membrane bound and cytosolic states. This is a similarity which the models for molecular motor transport in Chapter 2 share. As this section is a "primer", I will not proceed formally and introduce a small parameter ε into this problem; instead, only focus on the idea. Owing to the separation of time-scales (slow spatial processes and rapid binding and unbinding), it is possible to think of the terms in the PDE system (1.5) contributing on different time-

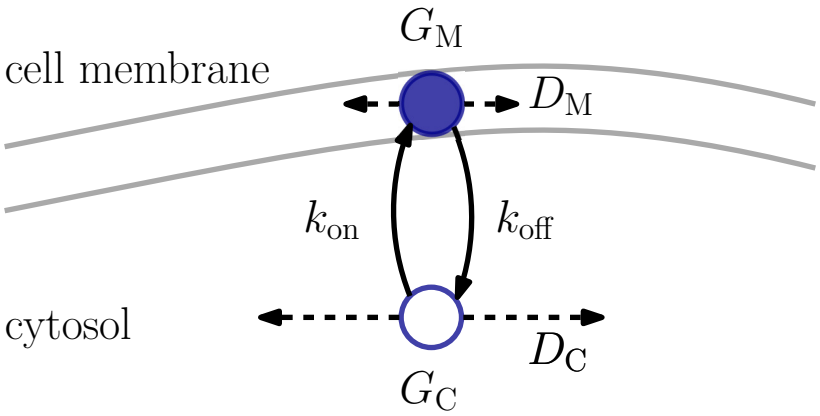

Figure 1.2: Some proteins convert between active, membrane-bound and inactive, freely diffusing cytosolic states (G_{M} and G_{C}, respectively). Proteins bind to the membrane and unbind from the membrane with rate coefficients k_{off} and k_{on} respectively. The diffusion coefficient D_{M} in the cell membrane is typically smaller than in the cytosol D_{C}. The QSS reduction method can be applied to a system of this type to derive an effective diffusion, which describes the diffusion of the total amount of protein.

scales. First, at any given spatial location, the amount of cytosolic and membrane-bound proteins will equilibrate on a short time-scale with essentially no diffusion. Second, on a slower time-scale, the diffusion will become significant. As such, it is helpful to think of a short time-scale denoted by τ (versus t), where the protein dynamics are dominated by the reaction-terms:

$$\frac{dG_{\mathrm{M}}}{d\tau} = k_{\mathrm{on}}G_{\mathrm{C}} - k_{\mathrm{off}}G_{\mathrm{M}}, \tag{1.7}$$

$$\frac{dG_{\mathrm{C}}}{d\tau} = -k_{\mathrm{on}}G_{\mathrm{C}} + k_{\mathrm{off}}G_{\mathrm{M}}. \tag{1.8}$$

The fact that these equations operate on a fast time-scale means that the variables rapidly equilibrate. On the short time-scale τ, this motivates the search for the steady-state of this system of ODEs. The steady-state of this ODE system is given by the linear relationship $G_{\mathrm{M}} = \frac{k_{\mathrm{on}}}{k_{\mathrm{off}}}G_{\mathrm{C}}$, hence the amount of membrane-bound proteins can be calculated from the amount of cytosolic proteins and vice versa. From this, I can make a quasi-steady-state approximation in the full system:

$$G_{\mathrm{M}}(x,t) \approx \frac{k_{\mathrm{on}}}{k_{\mathrm{off}}}G_{\mathrm{C}}(x,t). \tag{1.9}$$

Using this approximation, I find that $G(x,t) = \frac{k_{\mathrm{on}}+k_{\mathrm{off}}}{k_{\mathrm{off}}}G_{\mathrm{C}}(x,t) = \frac{k_{\mathrm{on}}+k_{\mathrm{off}}}{k_{\mathrm{on}}}G_{\mathrm{M}}(x,t)$ since

$G(x,t) = G_{\mathrm{M}}(x,t) + G_{\mathrm{C}}(x,t)$. For the same reason, note that adding the PDE in (1.5) gives

$$\frac{\partial G}{\partial t} = D_{\mathrm{M}} \frac{\partial^2 G_{\mathrm{M}}}{\partial x^2} + D_{\mathrm{C}} \frac{\partial^2 G_{\mathrm{C}}}{\partial x^2}. \tag{1.10}$$

Using the quasi-steady-state approximation $G = \frac{k_{\mathrm{on}}+k_{\mathrm{off}}}{k_{\mathrm{off}}} G_{\mathrm{C}} = \frac{k_{\mathrm{on}}+k_{\mathrm{off}}}{k_{\mathrm{on}}} G_{\mathrm{M}}$ in the PDE for G, I find that G satisfies a diffusion equation:

$$\frac{\partial G}{\partial t} = D_{\mathrm{M}} \frac{k_{\mathrm{on}}}{k_{\mathrm{on}} + k_{\mathrm{off}}} \frac{\partial^2 G}{\partial x^2} + D_{\mathrm{C}} \frac{k_{\mathrm{off}}}{k_{\mathrm{on}} + k_{\mathrm{off}}} \frac{\partial^2 G}{\partial x^2} \tag{1.11}$$

$$= \left(D_{\mathrm{M}} \frac{k_{\mathrm{on}}}{k_{\mathrm{on}} + k_{\mathrm{off}}} + D_{\mathrm{C}} \frac{k_{\mathrm{off}}}{k_{\mathrm{on}} + k_{\mathrm{off}}} \right) \frac{\partial^2 G}{\partial x^2} \tag{1.12}$$

$$= D_{\mathrm{eff}} \frac{\partial^2 G}{\partial x^2}, \tag{1.13}$$

where the effective diffusion coefficient, D_{eff} is a combination of the reaction rate coefficients, k_{on} and k_{off}, and the diffusion coefficients of proteins in either states, D_{M} and D_{C}. Increasing k_{off}, for example, would increase the contribution of the diffusion in the cytosolic state, to the overall distribution of proteins. In this case, the effective diffusion coefficient can also be interpreted as a weighted average of the original diffusion coefficients with the weights as the mean fraction residence time in either state. To see this, identify $\tau_{\mathrm{M}} = \frac{1}{k_{\mathrm{off}}}$ as the mean residence time on the membrane (before unbinding with rate k_{off}) and $\tau_{\mathrm{C}} = \frac{1}{k_{\mathrm{on}}}$ as the mean residence time in the cytosol (before binding to the membrane with rate k_{on}). With these definitions, note that

$$D_{\mathrm{eff}} = \frac{k_{\mathrm{on}} k_{\mathrm{off}}}{k_{\mathrm{on}} + k_{\mathrm{off}}} \left(\frac{D_{\mathrm{M}}}{k_{\mathrm{off}}} + \frac{D_{\mathrm{C}}}{k_{\mathrm{on}}} \right) \tag{1.14}$$

$$= \frac{1}{\tau_{\mathrm{M}} + \tau_{\mathrm{C}}} \left(D_{\mathrm{M}} \tau_{\mathrm{M}} + D_{\mathrm{C}} \tau_{\mathrm{C}} \right) \tag{1.15}$$

$$= D_{\mathrm{M}} \frac{\tau_{\mathrm{M}}}{\tau_{\mathrm{M}} + \tau_{\mathrm{C}}} + D_{\mathrm{C}} \frac{\tau_{\mathrm{C}}}{\tau_{\mathrm{M}} + \tau_{\mathrm{C}}}. \tag{1.16}$$

This calculation shows that the effective diffusion is a combination of diffusion on the membrane and diffusion in the cytosol, with the relative importance of each weighted by the fraction of time spent in the given state. The QSS not only reduces the complexity of the model but also provides insight into the biophysical processes.

In Chapter 2, the QSS approximation is applied to a model similar to (1.5); however, instead of a reaction-diffusion model, I will extend the QSS methodology to a class of three-component reaction-advection-diffusion system with nonlinear state transitions. In this case, I will show that the quasi-steady-state approximation is a PDE written in terms of one of the molecular motor states, denoted by $\alpha(x,t)$. The QSS PDE will be a balance

equation for the total amount of motors in the cell, with effective diffusion and effective transport terms that depend on the model parameters and on the amount of motors in the reference state α:

$$\frac{\partial}{\partial t} y(\alpha) = -\frac{\partial}{\partial x}\left(\mathcal{V}(\alpha) - \mathcal{D}(\alpha)\frac{\partial \alpha}{\partial x}\right). \tag{1.17}$$

In contrast with previous work, the dependence on α can be nonlinear. Here, $y(\alpha)$ is the total density of the motors in the cell, $\mathcal{V}(\alpha)$ is the effective transport term, and $\mathcal{D}(\alpha)$ is the effective diffusion. The QSS PDE is supplemented with no-flux boundary conditions at either end of the cell.

1.3 The Interplay Between Cell Signalling and Cell Mechanics

In the second part of the thesis, Chapter 3, instead of studying how sub-cellular interactions lead to cell-scale organization, I "zoom out" and study how cell-cell interactions can lead to emergent organization and behaviour at the tissue level.

The Rho-family GTPase proteins are central regulators within signalling networks of eukaryotic cells that are largely responsible for coordinating downstream signalling leading to changes in cell shape mediated by the actin cytoskeleton [73]. GTPases act as switches and exist in either an active (membrane-bound) or inactive (freely-diffusing cytosolic) state, as illustrated in Figure 1.3. When activated, GTPases transmit signals to other proteins that eventually lead to changes in cell behaviour. The activation and deactivation of GTPases is mediated by other proteins known as GTPase activating proteins (GAPs) and guanine nucleotide exchange factors (GEFs), respectively. There is a large body of literature addressing how GTPases spontaneously segregate to the front or back in a cell and how this can lead to cell polarization and movement [25, 54, 59, 64, 95, 99]. Here, I focus on a different aspect of GTPase activity and cell behaviour, namely how GTPase activity can cause a cell to contract or spread [3, 14, 78], and the resulting feedback with tension and mechanical forces.

Rho GTPases cycle between membrane-bound active forms, and freely-diffusing inactive forms. Their activation and deactivation is controlled by a large signalling network responsible for coordinating cellular responses to stimuli. The Rho-family GTPases Rac1, RhoA, and Cdc42 are central regulators of this network. Rac1 and RhoA (henceforth Rac and Rho) are downstream of cell-surface receptors that are sensitive to many different stimuli, including mechanical tension [18, 74, 97]. Moreover, there is increasing evidence for the specific molecular mechanisms and pathways by which Rac and Rho respond to mechanical signals [37, 62]. Of note is the effect that mechanical tension can have on activating or deactivating GTPase activity [15, 35]. Additionally, the feedback between mechanical signalling

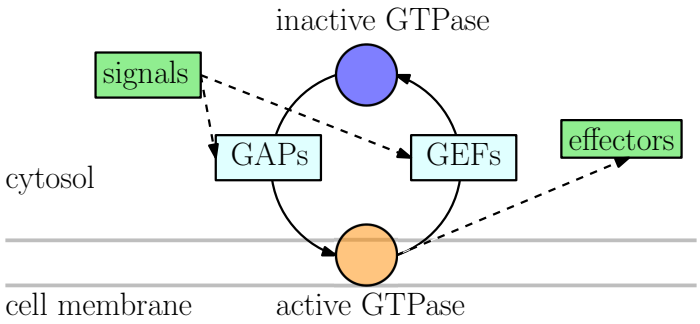

Figure 1.3: GTPases act as switches. They exist in a membrane-bound active or a freely diffusing inactive state. Activation and deactivation of GTPases are regulated by other proteins (GAPs and GEFs), which are activated by cellular signals. Once active, GTPases signal to downstream effectors.

and GTPase behaviour is two-way. While forces such as mechanical tension can influence GTPase activity, GTPase activity modifies cell shape through downstream signalling, which will subsequently affect the mechanical forces acting on a cell. This change in forces will then subsequently affect GTPase activity, and so on. It is this interplay—between signalling and mechanics—that I seek to understand.

Many recent experimental and modelling studies have provided evidence for the idea that cell behaviours (such as change in cell shape or polarity) can be explained as emergent properties of small subsets of large signalling networks [3, 9, 14, 78]. Mechanochemical interactions have been included in mathematical models of cell behaviour [60, 61, 63], and models consisting of GTPase modules can explain cell polarization [54], cell shape [33], and cell migration patterns [34, 65].

Using a minimal model for GTPase activity within a cell, I will explore the implications of the idea that mechanical tension on the cell is responsible for modifying the GTPase activation rate on cell behaviour. Specifically, I assume that GTPase can cycle between inactive and active forms, with some positive feedback upon activation. This is illustrated in Figure 1.4 with the active GTPase denoted by G and inactive by G_i. I also assume that active GTPase is responsible for contraction in the cell, and that mechanical tension on the cell is responsible for increasing the rate of activation of GTPase (purple boxes in Figure 1.4). Active GTPase leads to cell contraction, while tension is assumed to increase the activation rate of GTPase. If the cell is initially stretched, high tension will lead to the activation of GTPase, leading to contraction in turn. Once contracted, the initial stretch will no longer contribute to increasing the activation rate of GTPase, and the cell will return to rest. To implement this mechanochemical coupling, I use a mechanical model consisting of springs and dashpots to model cell length, and I propose and analyze a minimal GTPase-tension model. The simple two dimensional ODE model describes the dynamics of the GTPase

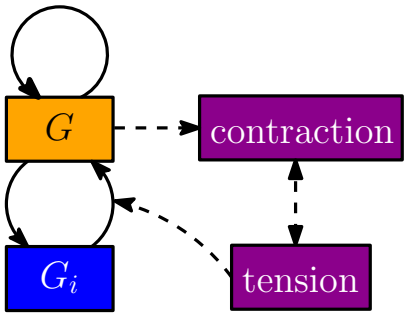

Figure 1.4: GTPase cycles between active and inactive forms, G and G_i, respectively, with positive feedback upon the active state. Active GTPase leads to cell contraction, while tension is assumed to increase the activation rate of GTPase. If the cell is initially stretched, high tension will lead to the activation of GTPase, leading to contraction in turn. Once contracted, the initial stretch will no longer contribute to increasing the activation rate of GTPase, and the cell will return to rest.

activity and the length of the cell. Thanks to the model simplicity it is possible to study the solution behaviour easily using numerical bifurcation analysis (as in Chapter 3), or by studying the phase plane (as illustrated in the next section). In short, the model exhibits three distinct behaviours dependent on the strength of coupling between tension and the GTPase activation rate: long, relaxed cells; short, contracted cells; and cells that oscillate between these two extremes. Building on this understanding, I next consider the dynamics of the minimal model when many cells are coupled together in a 1D array (representing an epithelial sheet), and finally using the Cellular Potts model (CPM) (reviewed in the next section) to explore the dynamics in a 2D epithelial tissue. In this way, the behaviour of the cell collective or tissue can be understood as emergent behaviour from cell-cell mechanical coupling and mechanochemical signalling in each cell.

In the next section, I provide a short mathematical primer for the modelling approaches used in Chapter 3, and draw comparisons to the new model I have developed with the mechanochemical model from the 1980s by Odell et al. [60].

1.3.1 Dynamical Systems for Cell Signalling and Cell Mechanics

In this section, I provide some preliminary results and explain some of the mathematical models used in Chapter 3. In particular, I will outline (1) a minimal model for GTPase activity, (2) compare my results with those of Odell et al. [60], and (3) briefly describe the Cellular Potts model (CPM).

A Minimal Model for GTPase Activity

I adapt the minimal GTPase model in Chapter 3 from the modelling work in [33, 34, 54], but ignore spatial effects and only consider the well-mixed model. The basic form of the equation is

$$\frac{dG}{dt} = (\text{rate of activation})\, G_i - (\text{rate of inactivation})\, G, \tag{1.18}$$

where G is the amount of active GTPase and G_i is the amount of inactive GTPase. Following previous work, I assume that the total amount of GTPase in the cell is roughly constant over the timescale of interest, i.e., that $G_T = G + G_i$ is constant, and that there is positive feedback from active GTPase to itself. This leads to an equation of the form

$$\frac{dG}{dt} = \left(b + \gamma \frac{G^n}{1+G^n}\right)(G_T - G) - G, \tag{1.19}$$

where b is the basal rate of activation, and γ gives the amplitude of the positive feedback. The Hill function $\frac{G^n}{1+G^n}$ is a saturating function of G. When G is much greater than 1, $\frac{G^n}{1+G^n} \approx 1$, but when G is much less than 1, $\frac{G^n}{1+G^n} \approx 0$. Note that time has been scaled so that the rate coefficient of deactivation of GTPase appears to be 1. This model has the requisite features for GTPase activity: a high-activity and a low-activity steady-state, and is bistable for a range of parameters. Bistability means that the GTPase activity G could tend toward the high-activity steady-state or low-activity steady-state depending on initial conditions. Moreover, the presence of bistability indicates the possibility of hysteresis, i.e., history-dependent transitions. Suppose, for example, that a stimuli can increase the GTPase activity. If the cell is at the low-activity steady-state, then a small, single stimuli would not automatically cause the cell to jump to the high-activity steady-state. Instead, thanks to the presence of bistability, the small stimuli would disappear as the cell returns to the low-activity steady-state. Only if the stimuli is sufficient to push the GTPase activity into the regime of high-activity will the cell transition away from the low-activity steady-state. The presence of bistability and hysteresis can also give rise to a relaxation oscillation, where the behaviour of the system slowly transitions through the low or high-activity steady-state region before "jumping" to the other (provided the system is coupled to another variable, such as cell length). Indeed, in Chapter 3, I will modify the activation rate to include a tension-dependent activation rate (later called $f(T)$), and the feedback from tension will drive the system into a low-activity, high-activity, or oscillatory state.

The Mechanical Basis of Morphogenesis

In the 1980s, Odell et al. [60] developed a mechanical model for cells in an epithelium during morphogenesis (development). The tissue undergoes shape changes as the cells bend

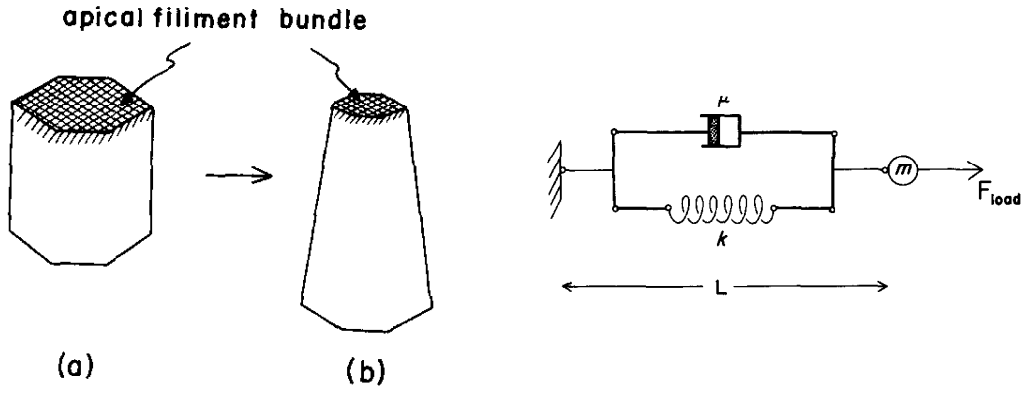

Figure 1.5: The apical filament bundle of an epithelial cell can contract (a)–(b). A viscoelastic element consists of a spring and a dashpot arranged in parallel and is used to model the apical filament bundle mechanics (right panel). Reprinted from Developmental Biology, 85, G.M. Odell, G. Oster, P. Alberch, and B. Burnside, The Mechanical Basis of Morphogenesis I. Epithelial Folding and Invagination, 446–462, Copyright 1981, with permission from Elsevier.

and deform themselves in order to undergo morphological processes such as invagination and neurulation. The main idea was to represent the deformable actin-based cortex of an epithelial cell as a spring-dashpot system with a rest-length that would depend on a protein or biochemical signalling. The actin cortex and the mechanical model used by Odell et al. [60] is illustrated in Figure 1.5. In (a)–(b), the apical filament bundle is illustrated at the top of an epithelial cell. This apical filament bundle can contract. Odell et al. [60] hypothesized that when the actin-based cortex is stretched beyond a critical length, the protein or biochemical signalling would become active and change the rest-length of the cell, making it smaller. Thus, when one cell is stretched, it will subsequently contract. In a tissue, when many such cells are coupled together, the contraction of one cell will impose a stretch on the neighbours and consequently induce size changes in neighbouring cells.

The spring-dashpot system used by Odell et al. [60] is what I adopt as a mechanical model in Chapter 3 (illustrated in the right panel of Figure 1.5). In such a system, the length of the cell is governed by the following equation, derived from Hooke's Law and from the fact that inertia is negligible in the deformation of cells:

$$\frac{dL}{dt} = -\frac{k}{\lambda}(L - L_0), \tag{1.20}$$

where L is the cell length, k is the spring constant, λ is the viscous damping coefficient, and L_0 is the rest-length of the spring. Note that μ is used for λ in Figure 1.5. This equation describes how a stretched or compressed spring will relax back towards its rest-length. Odell

et al. [60] assume that the baseline rest-length ε is decreased by the presence of a protein signal, C:

$$L_0 = \varepsilon + \frac{1}{1+\sigma C^n} \tag{1.21}$$

where σ and n are model parameters. At the same time, the protein signal C is assumed to be produced at a rate proportional to the cell length, decays linearly, and is auto-catalytic (positive feedback):

$$\frac{dC}{dt} = \frac{\alpha C^2}{1+\beta C^2} - \nu C + \gamma L. \tag{1.22}$$

In this equation, the Hill function $\frac{\alpha C^2}{1+\beta C^2}$ describes the auto-catalytic production of the protein signal C, and $-\nu C$ and γL describes the decay and production of the signal, respectively.

To understand the dynamics of the two-compartment ODE system above, it is possible to study the dynamics in the phase-plane (Figure 1.6). In this phase-plane the steady-states are identified as the intersections of the C and L nullclines (curves for which $\frac{dC}{dt} = 0$ and $\frac{dL}{dt} = 0$, respectively). Using parameters from [60], the system has three steady-states: (1) a high L low C stable steady-state, (2) a saddle point, and (3) a low L high C stable steady-state. The key feature of the system is that the stable manifold of the saddle point (purple curve in Figure 1.6) separates the phase-plane into two regions. Also shown are trajectories (grey curves) that start with different lengths, but no protein activity C. Only when the initial conditions are such that the length, $L(0)$ is above the stable manifold, will the cell "fire" and end in the contracted state (green "firing trajectory").

In Chapter 3, I use the same spring-dashpot system to model cell mechanics and a similar rest-length dependence. Instead of an unknown protein signal, C, I consider the effect of GTPase signalling G on cell length. I also assume that tension, proportional to the difference of the current length and the rest-length $T \propto L - L_0$, will increase the activation rate of the GTPase. As such, I suppose that

$$\frac{dG}{dt} = \left(b + f(T) + \gamma \frac{G^n}{1+G^n}\right)(G_T - G) - G, \tag{1.23}$$

where $f(T)$ describes how tension increase the activation rate. Depending on the strength of the feedback, $f(T)$, the coupled GTPase-length system can exist in a low-activity, relaxed-length steady-state; a high-activity, contracted steady-state; or continuously cycle between these extremes (limit cycle). I illustrate this limit cycle behaviour in Figure 1.7 which shows the phase-plane for the GTPase-tension model. The L nullcline has essentially the same shape as in Figure 1.6. For this set of parameters, the GTPase-length system is oscillatory with all trajectories (grey) converging to the limit cycle (shown in green). In Chapter 3, I study the effect of feedback strength on the behaviour of the GTPase-tension model.

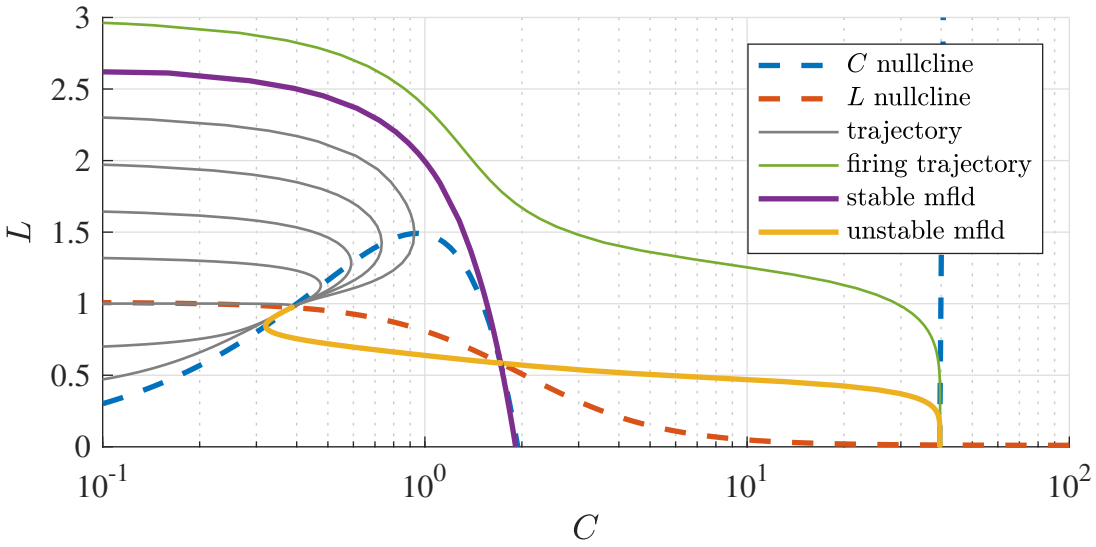

Figure 1.6: Phase-plane for the mechanochemical model from Odell et al. [60]. Note the logarithmic scale for the C-axis. Steady-states are found at the intersections of the C and L nullclines. Several trajectories are shown starting with various cell lengths L and with no protein signal C. Only if the cell is sufficiently stretched (above the stable manifold) will the cell end in the contracted state (high C, small L).

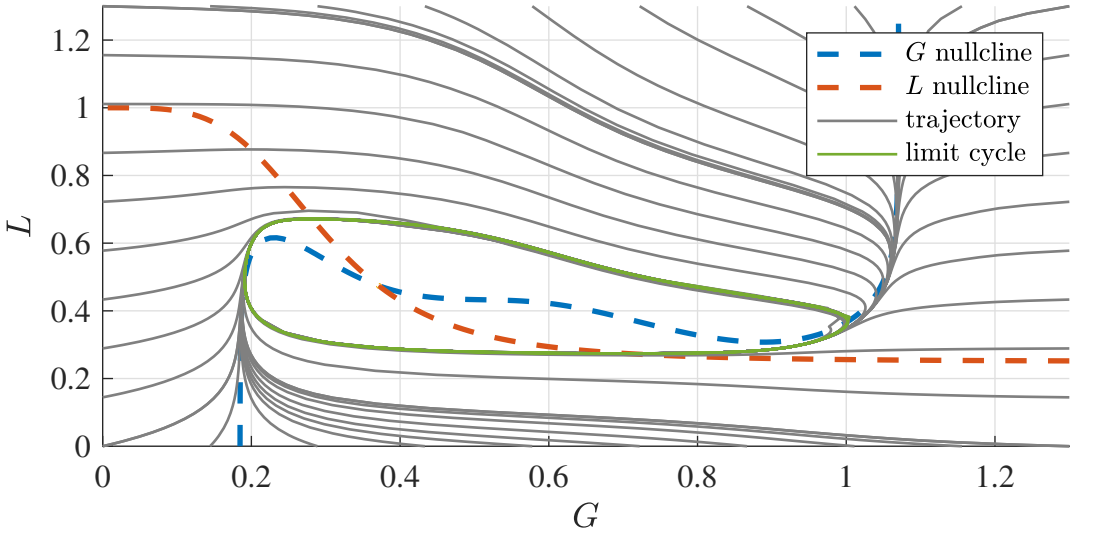

Figure 1.7: Phase-plane for the GTPase-tension model. For this set of parameters, there is one unstable steady-state (at the intersection of the G and L nullclines). There is a stable limit cycle (green trajectory) which corresponds to an oscillatory cell.

The Cellular Potts Model

The Cellular Potts model (CPM) is a lattice-based model for modelling cell behaviour. Cells are represented as a collection of lattice sites, which can grow and shrink by adding or removing sites. I use a freely available implementation of the CPM called CompuCell3D [90]. In the CPM, the movement of cells is controlled by a total system energy, called a Hamiltonian, $\mathcal{H}$. To simulate cells of a certain size, for example, a volume-dependent energy term is added to the Hamiltonian. When cells deviate from the target volume specified, the volume energy is high. The CPM then uses a Monte-Carlo method to accept changes that decrease the Hamiltonian, until the energy is minimized. Such changes include invasion or retreat at the edge of some region consisting of lattice sites that we identify as a cell. To mimic random fluctuations, even some changes that increase the Hamiltonian are accepted with some probability that is set by a parameter analogous to thermal energy. In this way, the cells attain their target volume.

A schematic of a typical CPM is shown in Figure 1.8. Each cell is a collection of lattice sites. At each step in the Monte-Carlo method (called a Monte-Carlo step (MCS)), one or more lattice sites are selected to change. If the proposed change decreases the overall energy of the system, i.e., $\Delta\mathcal{H} < 0$, then the change is accepted. If the proposed change increases the overall energy of the system, i.e., $\Delta\mathcal{H} \geq 0$, then the change is accepted as a small noise-induced fluctuation with probability $\exp(-\Delta H/T)$, where T is a numerical parameter known as the temperature. These changes are accepted to capture the noisy, stochastic nature of biophysical systems, and to avoid getting "trapped" in local energy minima of the Hamiltonian $\mathcal{H}$.

Other energies can be added to the Hamiltonian $\mathcal{H}$. For example, in Chapter 3, I will also include an adhesion energy that describes how cells "stick" together. The idea is that the adhesion energy depends on cell-cell contacts. For those cells which have large interfaces with their neighbours have stronger adhesion and therefore lower adhesion energy. In this way, the cells in the CPM tend to group together and remain contiguous. Additional details regarding the CPM simulations used in Chapter 3 can be found in Appendix B.

1.4 Thesis Outline

Using these mathematical and computational tools, I discuss two examples of multi-scale modelling in cell biology in the next chapters. In Chapter 2, I apply quasi-steady-state methods to models of intracellular transport by molecular motors. This chapter is self-contained (it has its own introduction and discussion) and is supplemented by Appendix A, which contains some additional details referenced in the main chapter text. In Chapter 3, I use a dynamical systems approach to explore the interplay between cell signalling and

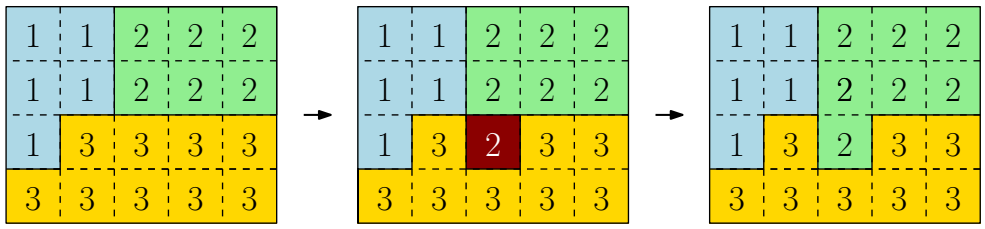

Figure 1.8: A schematic of a typical CPM. Each cell, labelled 1, 2, and 3, is a collection of lattice sites. A proposed change is accepted if the change reduces the overall energy in the system or with some small probability if it increases the overall energy.

cell mechanics, and the resulting implications on cell behaviour. Likewise, this chapter is self-contained and is supplemented by Appendix B, which contains some additional details. In Chapter 4, I conclude the thesis with a summary of the results, a discussion of the significance of the work, and present some questions and ideas for future work.

Chapter 2

Application of Quasi-Steady-State Methods to Nonlinear Models of Intracellular Transport

2.1 Intracellular Transport by Molecular Motors

Diffusion is a fast transport mechanism on the length scale of a typical cell, a few tens of micrometers. However, some specialized cells, including neurons, are up to 1 metre in length. This length scale imposes dramatic constraints on the transport of structural, metabolic, and signalling components from the neuronal cell body (the soma) to the ends of dendrites or axons. Molecular diffusion is extremely inefficient for transport at such length scales. Fortunately, cells have evolved active transport mechanisms consisting of molecular motors that bind to microtubule tracks and convey cargo packaged in vesicles across the cell [10].

Microtubules (MTs) are asymmetric, having distinct "plus" and "minus" ends. The two major types of molecular motors, kinesin and dynein, walk on microtubules in opposite directions: kinesin walks towards the plus ends, while dynein walks towards the minus ends of MTs. Although kinesin motors can also work towards the minus ends and have other roles within cells, I consider only those kinesin motors which walk towards the plus ends of MTs. Both motors exist in several states, including unbound, cytoplasmic forms [5], and MT-bound as well as bound singly or in groups to cargo. The overall transport of motors across the cell depends on the polarity and configuration of MTs, the rates of binding to and unbinding from MTs, and the motor speeds while bound. Transport also depends on molecular diffusion in the cytosol.

One convenient experimental system is *Ustilago maydis*, a fungus whose long filamentous

hyphae contain MTs of mixed polarity [23, 80, 81, 86, 87]. Microtubules of mixed polarity also occur in the proximal regions of neuronal dendrites [2, 8, 88]. In these systems, particularly in the fungal hyphae, motors have been observed to move bidirectionally: first towards one cell end, and then towards the opposite end. This observation can be explained in one of two ways. Either multiple motors (dynein and kinesin) bound to the same cargo can "take turns" pulling the load, or else a single motor, by detaching and binding to a MT of opposite polarity, would then change its direction of motion.

Modelling Motor-based Transport

An intriguing question is how to approach the multi-scale problem of bridging between the rates and events at the molecular level (binding, unbinding, and motor speeds) and the overall cargo distribution and effective transport speed at the cellular level [84]. This has motivated the development of a number of mathematical models at various levels of detail. A number of efforts have dealt with the tug-of-war or teamwork of several motors attached to a single cargo [4, 31, 40, 48, 55]. In many cases, such models mandate stochastic and computational approaches, that consider multiple states (n, m motors of distinct types attached to a cargo, etc.). Other approaches simplify the problem to consider only a few states, and formulate transport equations [85] or derive such PDEs from a master-equation approach to the stochastic motor behaviour. Examples of such approaches include (1) an analysis and mean-field approximation of the dynamics of the totally asymmetric simple exclusion process with Langmuir kinetics [66], (2) a study of the spontaneous formation of traffic "jams" resulting from transport on two parallel lanes (two parallel microtubule tracks) [72], (3) the incorporation of a kinetic model for motor stepping dynamics, and a study of the resulting effects on collective transport [11]. The approach here follows the novel and elegant linear theory developed by Bressloff and Newby [7, 57] for important insights into motor function by deriving a quasi-steady-state (QSS) Fokker-Planck equation. The Fokker-Planck equation describes the overall transport in the system through effective diffusion and effective velocity, which depend on the model parameters. Although this linear theory is based on simplifications and assumptions (e.g. that the binding/unbinding kinetics are fast on the timescale of transport across the cell), it provides a useful way to gain insight into the role of various parameters in determining the overall functionality of the transport system.

In recent work, [26] used the PDE approach to model the transport of early endosomes (cargo transported by kinesin and dynein) inside *Ustilago maydis*, arriving at good agreement with experimental observations, and posing several hypotheses for further experimental studies. A followup paper [16] applied the methods of [7, 57] to the examples motivated by [26]. In both these recent works, the models included microtubules of mixed

polarity, with and without a bias towards one end of the (1D) cell, and linear rates of binding and unbinding from the MT. Results in [16], for example, demonstrate that the effective velocity of transport is the average of motor velocities, weighted by the fraction of time spent in a given state, whereas the effective diffusivity is similarly such an average, but includes an additional term that represents the variance in velocities of motors in different states.

Linearity of the binding rates presumes that there is no interaction between groups of motors, and that binding sites are ample and unlimited. But in many biological situations, such assumptions are unwarranted. Complicated, possibly nonlinear, features have been observed in molecular motor traffic jams [44], and exclusion of one motor by others [79]. Another case is the effect of microtubule associated proteins (MAPS) such as tau that modulate the ability of motors to bind to MTs or to stay bound [19, 53]. MTs can also have various post-translational modifications that affect the availability or affinity of binding sites to motors. For example, kinesin-1 binds with higher affinity to MT that have been modified by acetylation [70]. Considering such effects leads to models in which the binding or unbinding is nonlinear and saturating, or to models that include mass-action-type reaction terms. The effect of spatially varying parameters resulting from non-homogeneous MT polarity, ATP gradients, and MAPS have been investigated in the context of intracellular transport in neuronal cells using quasi-steady-state methodology [57], yet the effect of nonlinear kinetic terms has been largely unexplored analytically. The need to generalize previous analysis to include models with such nonlinearities motivates the approach in this chapter.

The Quasi-steady-state Reduction Method

The main mathematical focus, discussed in detail in §2.3, is to extend the quasi-steady-state (QSS) reduction method introduced in [57] for reaction–advection–diffusion systems with linear reaction kinetics to a class of problems where the kinetics are nonlinear, but where a conservation condition is satisfied. The latter represents the fact that motors transit between states, but are conserved overall. The QSS method relies on the assumption that the nonlinear kinetics occur on a faster time-scale than the diffusion and advection processes. Owing to the conservation condition, in this limit of fast reaction kinetics, a one-parameter family of quasi-steady-state solutions is obtained from the equilibrium state of the kinetics. Simply put, this means that it is possible to approximate the solution of the full system with a single variable that will vary in space and time. When there are no eigenvalues of the linearization of the kinetics along this one parameter family that lie in the unstable right half-plane, this quasi-steady-state solution is referred to as a slow solution manifold for the full reaction–advection–diffusion system. When this condition on the Jacobian of

the nonlinear kinetics is satisfied, it is possible to use an asymptotic expansion together with a Fredholm alternative condition to derive a single scalar quasi-steady-state PDE, which effectively parameterizes the slow solution manifold, and approximates the solutions to the full system.

In §2.4, the asymptotic formalism of §2.3 is applied to analyze three specific nonlinear systems for the binding and unbinding of molecular motors. These models are formulated in §2.2 and consist of (1) a model for a single motor ("kinesin") transiting between motion along right-pointing MTs, diffusion in the cytosol, and motion along left-pointing MTs (with transitions only through the cytoplasmic pool), (2) a model for kinesin-dynein-cargo complexes moving left or right along MTs or diffusing in the cytosol (interactions on a MT are assumed to lead to motor swaps that also change the direction of motion), and (3) a model for motors ("unconventional myosin") whose encounters with each other on an actin filament lead to stalling. In all three cases, motors exchange between cytosolic diffusible states and states bound to a track (MT or actin). Nonlinearity stems from saturated binding kinetics in (1), mass-action motor interactions leading to swaps in (2), and from stalling in (3).

Overall, the QSS PDE is used to analyze the behaviour of steady-state solutions of the full reaction–advection–diffusion system as parameters are varied, and the results are then interpreted biologically. The main conclusion is that in all three cases studied, the resulting QSS PDE is a conservation law for the total motor density within the cell, with effective velocity and effective diffusion that depend nonlinearly on the model parameters and motor density. Predictions about the full model behaviour are made using the analytical insight gained through the QSS reduction, and the effective velocity and effective diffusion functions. To verify the QSS method and analysis, the steady-state and time-dependent behaviour of both the full models and the QSS PDE are studied numerically.

Summary of Results for the Molecular Motor Models

In the kinesin motor model, the nonlinear interactions depend on the density of cytosolic motors. The QSS PDE describes the bulk motor distribution through effective velocity and diffusion coefficients. These effective coefficients are related to the original velocity and diffusion coefficients weighted by the time spent in the directed-movement and random-movement states. Moreover, the polarity distribution of MTs affects the bulk motor distribution by changing the sign of the velocity, which can bias the distribution of motors to the right- or left-end of the cell.

Unlike the kinesin motor model, the nonlinear kinetics in the kinesin-dynein motor complex model arise due to a mass-action law which describes the rate at which motor complexes turn in response to motor complexes heading in the other direction. In this

case, the resulting QSS PDE is again a conservation law for the total density of motor complexes, with the advection speed dependent on the motor complex speed, the turning rate, and which motors in the complex are active. In addition to these parameters, the resulting diffusion coefficient is dependent on the binding affinity of the motor complex to MTs. A sufficiently high turning rate can reverse the distribution of motor complexes from one end of the cell to the other, even if the probability of moving to one end of the cell is high.

In the myosin motor model, two different QSS PDE arise from the nonlinear reaction kinetics. In the first case, the motors equilibrate between freely diffusing and walking on MT, without any motors in the stalled state. In the second case, there are some motors in the stalled state. In the first case, the QSS PDE is linear, with effective diffusion coefficient and effective velocity mediated by the binding rate of myosin motors. We find that the asymptotic solution compares favourably with full numerical simulations of the myosin model. In the second case, the resulting QSS PDE is nonlinear, but is a conservation law for the total density of myosin motor. The effective transport rate depends on the density of stalled motors, the velocity of stalled motors due to actin treadmilling, and the stalling rate. The effective rate of diffusion depends on all model parameters except for the velocity of stalled motors due to treadmilling. The second QSS is only valid for a range of parameter space and stalled motor density. Outside of this range, the QSS PDE is ill-posed. A further novel feature of the myosin model is that the full system always converges to the first QSS, where there are no stalled motors. Through a boundary layer analysis (§2.5), I determine that this results from the boundary conditions. I develop an alternate myosin model which has the same QSS approximations but, depending on initial conditions, can realize either case.

2.2 Models of Intracellular Transport

I model the cell as a 1D tube of length L_0, with its left-end at $x = 0$. The densities of motors are described as number per unit cell length, with the cross-sectional area of the cell assumed to be constant. Molecular motors exist in any number, n, of possible states within the cell, with $p_i(x,t)$ denoting the density of motors in state i.

A reaction–advection–diffusion system describes the evolution of the vector density $\mathbf{p} \equiv (p_1, \ldots, p_n)^T$ of motors as

$$\frac{\partial \mathbf{p}}{\partial t} = \mathbf{M}(\mathbf{p}) + \mathbf{f}(\mathbf{p}), \tag{2.1}$$

where $\mathbf{f} \equiv (f_1, \ldots, f_n)^T$ describes the state transition rates, and $\mathbf{M}$ is a diagonal matrix of linear differential operators characterizing the advection and diffusion of motors in each state. For example, a term on the diagonal in row i, $M_{ii} = -v_i \frac{\partial}{\partial x} + D_i \frac{\partial^2}{\partial x^2}$, would describe

the advection (v_i) and the diffusion (D_i) of motors in state f_i. We assume that the ends of the cells are closed, and hence impose an overall zero-flux condition at the cell ends. In addition, we assume that the motors are exchanged between states in such a way that there is no net loss or gain of motors, i.e., that

$$\sum_{i=1}^{n} f_i = 0. \tag{2.2}$$

These two assumptions result in conservation of the total density of molecular motor in the cell.

The goal is to develop a theoretical framework to analyze models of the form (2.1) where the reaction term $\mathbf{f}$ is nonlinear and the reactions occur on a time-scale that is fast relative to the time-scale of the advection and diffusion processes. This theory is then applied to three specific nonlinear binding mechanisms. In §2.2.1 and §2.4.1 a nonlinear kinesin model is considered, in §2.2.2 and §2.4.2 a nonlinear kinesin-dynein model is considered, while a nonlinear myosin model is considered in §2.2.3 and §2.4.3. This analysis extends the previous analysis for linear reaction models developed in [7, 16, 57] to allow for nonlinear reaction mechanisms.

2.2.1 Kinesin Model

In hyphae of the fungus, *Ustilago maydis*, for example, kinesin motors walk along microtubules within the cell or diffuse freely in the cytosol [16, 26, 81, 81, 86]. The density $p^{\mathrm{R}}(x,t)$ (respectively $p^{\mathrm{L}}(x,t)$) represents the population of kinesin bound to right-polarized (respectively left-polarized) MTs walking toward the end of the cell at $x = L_0$ (respectively $x = 0$). The population of freely diffusing cytosolic kinesin is modelled by the density $p^{\mathrm{U}}(x,t)$ (U for unbound). Inside this 1D domain, $0 \leq x \leq L_0$, the density of MTs is constant and nonzero, with the MT distribution described by $0 \leq P(x) \leq 1$, representing the fraction of MTs pointing to the right at a point x. Since kinesin always walks towards a MT plus end, it can reverse its direction of motion only by unbinding from a given MT and rebinding to a MT of opposite polarity. For this reason, we can assume that, in this model, motor transitions occur only through the cytosolic state. We describe the spatiotemporal evolution of the kinesin densities by the transport equations (see the schematic diagram in

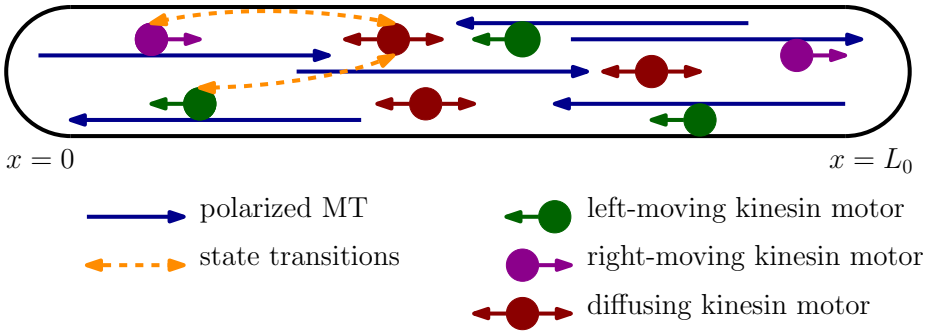

Figure 2.1: A schematic diagram of kinesin-based intracellular transport in a 1D cell of length L_0. Kinesin motors can bind to polarized microtubules (MTs, blue arrows), and move to the right (purple circles with right-pointing arrows) or to the left (green circles with left-pointing arrows). While unbound, kinesin motors are free to diffuse in the cell's cytoplasm (red circles with right and left-pointing arrows). State transitions (orange dashed arrows) occur through the freely diffusing cytosolic state.

Figure 2.1):

$$\frac{\partial p^{\mathrm{R}}}{\partial t} = -v\frac{\partial p^{\mathrm{R}}}{\partial x} + Pk_{\mathrm{b}}g(p^{\mathrm{U}}) - k_{\mathrm{u}}p^{\mathrm{R}}, \tag{2.3a}$$

$$\frac{\partial p^{\mathrm{L}}}{\partial t} = v\frac{\partial p^{\mathrm{L}}}{\partial x} + (1-P)k_{\mathrm{b}}g(p^{\mathrm{U}}) - k_{\mathrm{u}}p^{\mathrm{L}}, \tag{2.3b}$$

$$\frac{\partial p^{\mathrm{U}}}{\partial t} = D_0\frac{\partial^2 p^{\mathrm{U}}}{\partial x^2} - k_{\mathrm{b}}g(p^{\mathrm{U}}) + k_{\mathrm{u}}p^{\mathrm{R}} + k_{\mathrm{u}}p^{\mathrm{L}}. \tag{2.3c}$$

In Eqs. (2.3), bound kinesin moves to the right or to the left with velocity v, and D_0 is the diffusion coefficient for cytosolic kinesin. The unbinding rate constant is k_{u}, while the binding rate constants for kinesin binding to right-polarized and left-polarized MTs are $k_{\mathrm{b}}Pg(p^{\mathrm{U}})$ and $k_{\mathrm{b}}(1-P)g(p^{\mathrm{U}})$, respectively. Here, $P = P(x)$ is the fraction of MTs polarized towards the right in the cell. Here we have assumed a constant density of MTs across the cell (absorbed into the constant k_{b}). We discuss a generalization to nonuniform MT density $m(x)$ in Appendix A.3.1. The function $g(p^{\mathrm{U}})$, possibly nonlinear, describes how other processes such as competition for binding sites or binding co-operativity are modelled. For instance, saturated binding due to a limited number of binding sites could be depicted by a term of the form

$$g(p^{\mathrm{U}}) = g_{\mathrm{m}}\frac{p^{\mathrm{U}}}{K + p^{\mathrm{U}}}, \tag{2.4}$$

for some parameters $K > 0$ and $g_{\mathrm{m}} > 0$. Forms such as (2.4) are obtained by assumptions typical of Michaelis-Menten kinetics. Conservation of the kinesin motors within the cell implies that zero-flux boundary conditions are required to model the impermeable cell

ends:

$$\left(vp^{\mathrm{R}} - vp^{\mathrm{L}} - D_0\frac{\partial p^{\mathrm{U}}}{\partial x}\right)\Bigg|_{x=0,L_0} = 0. \tag{2.5}$$

The two additional boundary conditions are that there is no right-moving kinesin at the left endpoint of the cell and no left-moving kinesin at the right endpoint. These boundary conditions result from the fact that to create a flux of right-moving kinesin at a given point, there had to be a kinesin bound to a MT to the left of that point—which is impossible at $x = 0$, the leftmost point in the cell. A similar argument at the rightmost point in the cell establishes the right endpoint. Thus, the following two Dirichlet conditions must hold:

$$vp^{\mathrm{R}}(0) = 0 \quad \text{and} \quad vp^{\mathrm{L}}(L_0) = 0. \tag{2.6}$$

2.2.2 Kinesin-Dynein Model

The three-state kinesin model, formulated in §2.2.1, is a simplification of intracellular cargo transport. Cargo in fungal hyphae is typically bound to one dynein and four or five kinesin motors at a time [81]. In this case, the entire kinesin-dynein-cargo complex may be transported toward or away from the cell tip, depending on which motors are actively involved in the transport process and the polarity of the MTs to which they are bound. In this section, I describe a simple model for the organization and transport of cargo bound to a kinesin-dynein motor complex.

The populations of kinesin-dynein-cargo complexes are divided into right-moving, left-moving, and freely diffusing sub-classes, regardless of the molecular motors active in the transport process. In the three-state kinesin model, the nonlinearities are restricted to binding and unbinding interactions. To explore the effect of nonlinear interactions between motors in distinct sub-classes, consider linear binding and unbinding interactions, but allow for nonlinear interaction terms between the right- and left-moving species when they are in proximity on a MT. Yochelis et al. [101, 102] have recently used a model with a similar nonlinear interaction to describe the spatial organization and dynamics of unconventional myosin motors in actin-based cellular protrusions. I ask whether the QSS theory can be applied to a model of this type.

The population of right-moving (respectively left-) motor complexes walking toward the end of the cell at $x = L_0$ (respectively $x = 0$) is described by density $p^{\mathrm{R}}(x,t)$ (respectively $p^{\mathrm{L}}(x,t)$). The population of freely diffusing cytosolic motor complexes is described by density $p^{\mathrm{U}}(x,t)$. Here, a "binding bias" function, Q, represents the probability that when a free motor complex binds to a MT, it becomes a right-moving motor complex. Then (assuming no stalled states on the MT) the probability of becoming a left-moving motor complex, upon binding to a MT, is $(1-Q)$. Since kinesin walks towards the plus ends, while

dynein walks towards the minus ends of MTs, the function $Q(x)$ actually comprises several biological quantities, including local MT polarity, ratio of kinesin and dynein molecules in a complex, as well as respective affinities to MT of these two motors. In Appendix A.3.2, I discuss how this simplification by a single function can be related to such biological factors. An important distinction between this and the previous model is that now direction-switching can take place on a microtubule, and does not require unbinding into the cytosol.

The above simplification allows for the detailed study of a nonlinear interaction between right- and left-moving populations. One possible interaction between these two populations is that a direction change results upon an encounter with a motor-complex travelling in the opposite direction. Assume that when a right-moving complex meets a left-moving complex, the right-moving complex changes direction with rate coefficient k_{rl}. Similarly, when a left-moving complex meets a right-moving complex, the right-moving complex changes direction with rate coefficient k_{lr}. These direction changes are due to a swap between a motor that is actively walking, e.g., dynein, and its passive partner motor kinesin, or vice versa, in the given complex.

Freely diffusing motor complex binds to MTs at rate k_{b}, and diffuses in the cytosol with diffusion coefficient D_0. Bound motor complexes can move to the right (or left) with velocity v_{r} (or v_{l}) or they can unbind from MTs with rate k_{u}. These assumptions lead to the following reaction-diffusion-advection system on $0 \leq x \leq L_0$ (see the schematic diagram in Figure 2.2):

$$\frac{\partial p^{\mathrm{R}}}{\partial t} = -v_{\mathrm{r}}\frac{\partial p^{\mathrm{R}}}{\partial x} + k_{\mathrm{b}}Qp^{\mathrm{U}} - k_{\mathrm{u}}p^{\mathrm{R}} - k_{\mathrm{rl}}p^{\mathrm{R}}p^{\mathrm{L}} + k_{\mathrm{lr}}p^{\mathrm{L}}p^{\mathrm{R}}, \tag{2.7a}$$

$$\frac{\partial p^{\mathrm{L}}}{\partial t} = v_{\mathrm{l}}\frac{\partial p^{\mathrm{L}}}{\partial x} + k_{\mathrm{b}}(1-Q)p^{\mathrm{U}} - k_{\mathrm{u}}p^{\mathrm{L}} + k_{\mathrm{rl}}p^{\mathrm{R}}p^{\mathrm{L}} - k_{\mathrm{lr}}p^{\mathrm{L}}p^{\mathrm{R}}, \tag{2.7b}$$

$$\frac{\partial p^{\mathrm{U}}}{\partial t} = D_0\frac{\partial^2 p^{\mathrm{U}}}{\partial x^2} - k_{\mathrm{b}}p^{\mathrm{U}} + k_{\mathrm{u}}(p^{\mathrm{R}} + p^{\mathrm{L}}). \tag{2.7c}$$

With $k_{\mathrm{c}} \equiv k_{\mathrm{rl}} - k_{\mathrm{lr}}$, this model can be written as

$$\frac{\partial p^{\mathrm{R}}}{\partial t} = -v_{\mathrm{r}}\frac{\partial p^{\mathrm{R}}}{\partial x} + k_{\mathrm{b}}Qp^{\mathrm{U}} - k_{\mathrm{u}}p^{\mathrm{R}} - k_{\mathrm{c}}p^{\mathrm{R}}p^{\mathrm{L}}, \tag{2.8a}$$

$$\frac{\partial p^{\mathrm{L}}}{\partial t} = v_{\mathrm{l}}\frac{\partial p^{\mathrm{L}}}{\partial x} + k_{\mathrm{b}}(1-Q)p^{\mathrm{U}} - k_{\mathrm{u}}p^{\mathrm{L}} + k_{\mathrm{c}}p^{\mathrm{R}}p^{\mathrm{L}}, \tag{2.8b}$$

$$\frac{\partial p^{\mathrm{U}}}{\partial t} = D_0\frac{\partial^2 p^{\mathrm{U}}}{\partial x^2} - k_{\mathrm{b}}p^{\mathrm{U}} + k_{\mathrm{u}}(p^{\mathrm{R}} + p^{\mathrm{L}}). \tag{2.8c}$$

As before, conservation of the motor complexes within the cell implies that zero-flux bound-

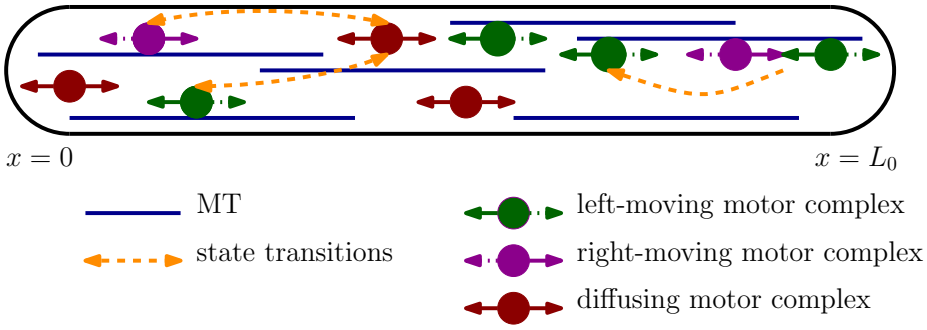

Figure 2.2: As in Figure 2.1 but for the kinesin-dynein motor complexes. Color code as before for MT, and for left-moving, right-moving, or diffusing complexes. A new feature is that state transitions can also occur through the collision of a left- and right-moving motor complex (orange dashed arrows, right).

ary conditions are required to model the impermeable cell ends:

$$\left(v_{\mathrm{r}} p^{\mathrm{R}} - v_{\mathrm{l}} p^{\mathrm{L}} - D_0 \frac{\partial p^{\mathrm{U}}}{\partial x} \right) \Bigg|_{x=0,L_0} = 0. \tag{2.9}$$

The remaining two boundary conditions are that

$$v_{\mathrm{r}} p^{\mathrm{R}}(0) = 0 \quad \text{and} \quad v_{\mathrm{l}} p^{\mathrm{L}}(L_0) = 0. \tag{2.10}$$

2.2.3 Myosin Model

Like kinesin and dynein motors, unconventional myosin motors are also responsible for intracellular transport in actin-based cellular protrusions, such as filopodia and stereocilia [56]. Filopodia are long, thin cellular protrusions with actin filaments at their core. These structures are involved in cell motility, adhesion, and communication [51]. Stereocilia are highly organized protrusions on hair-cells of the inner ear, responsible for hearing [82]. The actin-based filamentous scaffold that supports these protrusions is known to undergo turnover. The actin-based scaffold is maintained by the delivery of new actin monomer subunits to the distal ends of the protrusions, and the disassembly of the actin bundle at its base [76]. The apparent motion of the actin filament bundle due to continual assembly and disassembly at opposite ends is called treadmilling. The transport of those monomers and other material is facilitated by unconventional myosin motors [56]. In [101, 102], a reaction–advection–diffusion model was employed to describe the self-organization of waves and pulse trains in myosin motor distribution along cell protrusions. Inspired by this model, I consider a simplified system with the same nonlinear cross-species interaction term to demonstrate that the QSS method can be applied.

Consider three populations of myosin motors: bound (p^{B}), walking (p^{W}), and unbound (freely diffusing) (p^{U}) in a 1D geometry. Suppose that the base of the protrusion of length L_0 is at $x = 0$, but assume that the protrusion is self-contained and impose zero total-flux boundary conditions at both ends. Adapted from [101, 102], the myosin dynamics are described by the following set of reaction–diffusion–advection equations on $0 \leq x \leq L_0$:

$$\frac{\partial p^{\mathrm{W}}}{\partial t} = -v_{\mathrm{w}} \frac{\partial p^{\mathrm{W}}}{\partial x} - \hat{k}_{\mathrm{bw}} \left(p^{\mathrm{B}}\right)^2 p^{\mathrm{W}} + \hat{k}_{\mathrm{b}} p^{\mathrm{U}} - k_{\mathrm{u}} p^{\mathrm{W}}, \tag{2.11a}$$

$$\frac{\partial p^{\mathrm{B}}}{\partial t} = v_{\mathrm{b}} \frac{\partial p^{\mathrm{B}}}{\partial x} + \hat{k}_{\mathrm{bw}} \left(p^{\mathrm{B}}\right)^2 p^{\mathrm{W}} - k_{\mathrm{u}} p^{\mathrm{B}}, \tag{2.11b}$$

$$\frac{\partial p^{\mathrm{U}}}{\partial t} = D_{\mathrm{f}} \frac{\partial^2 p^{\mathrm{U}}}{\partial x^2} - \hat{k}_{\mathrm{b}} p^{\mathrm{U}} + k_{\mathrm{u}} (p^{\mathrm{B}} + p^{\mathrm{W}}). \tag{2.11c}$$

Due to actin treadmilling, bound (stalled) motors are effectively transported toward the base of the actin bundle with the treadmiling velocity v_{b}. Bound motors unbind with rate k_{u} and walking motors can become bound if they encounter a sufficiently high density of bound motors ($\hat{k}_{\mathrm{bw}} \left(p^{\mathrm{B}}\right)^2 p^{\mathrm{W}}$). Walking motors, on the other hand, move to the distal end of the cell protrusion with velocity v_{w}. Walking motors may also unbind to become freely diffusing motors. The freely diffusing motors have diffusion coefficient D_{f}, and can reattach to an actin filament and transition to a walking motor with rate coefficient $\hat{k}_{\mathrm{b}}$.

Assume that the total flux of myosin is zero at either end of the protrusion, which gives the boundary condition

$$\left(v_{\mathrm{w}} p^{\mathrm{W}} - v_{\mathrm{b}} p^{\mathrm{B}} - D_{\mathrm{f}} \frac{\partial p^{\mathrm{U}}}{\partial x} \right) \Bigg|_{x=0,L_0} = 0. \tag{2.12}$$

As before, there are two additional boundary conditions:

$$v_{\mathrm{w}} p^{\mathrm{W}}(0) = 0 \qquad \text{and} \qquad v_{\mathrm{b}} p^{\mathrm{B}}(L_0) = 0, \tag{2.13}$$

which ensures that there is no right-moving and left-moving myosin at the left and right endpoints, respectively.

2.3 Quasi-steady-state Reduction

The quasi-steady-state (QSS) reduction method, developed in [7] for the case where the vector $\mathbf{f}$ of state transitions is linear, will be extended to allow for nonlinear $\mathbf{f}$. Here, the nonlinearities can encode nonlinear biological phenomena, such as the affect of saturated binding due to competition for binding sites or traffic jam-style interactions as mentioned in §2.2. In this asymptotic approach, the key assumption is that the timescale associated with transitions between states, represented by binding and unbinding mechanisms, is short

relative to the time it takes for motors to move across the cell. This is warranted, for example, in long cells such as fungal hypha. The separation of time scales introduces a small dimensionless parameter $\varepsilon \approx v/(L_0 k)$, where v is the motor velocity, L_0 is the cell length, and k is a typical transition rate.

Using the QSS approximation, the aim is to reduce the system of transport equations to a scalar nonlinear PDE describing the dynamics of the system for small ε. To this end, consider rescaling space and time so that the non-dimensional length of the cell is 1 and so that one of the motor subpopulations moves with non-dimensional speed 1, scaling distance by the cell length, and scaling time by the time it takes for a walking motor to move across the cell. That is, introduce the new dimensionless variables

$$x^\star = \frac{x}{L_0}, \qquad t^\star = \frac{t v_i}{L_0}. \tag{2.14}$$

Under this scaling, and with the assumption that the timescale associated with transitions between states is short, the system (2.1) can be written, upon dropping the stars, as

$$\frac{\partial \mathbf{p}}{\partial t} = \mathbf{M}(\mathbf{p}) + \frac{1}{\varepsilon}\mathbf{f}(\mathbf{p}), \tag{2.15}$$

where $\mathbf{f}(\mathbf{p})$ represents the $\mathcal{O}(1)$ nonlinear motor state transition kinetics. Here $\mathbf{M}$ is the linear $n \times n$ matrix differential operator in the re-scaled coordinates, with zero off-diagonal entries, so that $\mathbf{M}_{ij} = 0$ for $i \neq j$, and diagonal entries $\mathbf{M}_{ii} = -v_i \partial/\partial x + D_i \partial^2/\partial x^2$ for $i = 1, \ldots, n$, with v_i possibly not all unity if the right- and left-moving motors have different speeds. Details of the scaling leading to (2.15) for the three specific models are given in Appendix A.4.

The QSS reduction method exploits the assumed small parameter ε in (2.15). On a short time scale, where $t = \mathcal{O}(\varepsilon)$ so that $\tau = t/\varepsilon$, (2.15) yields

$$\frac{\partial \mathbf{p}}{\partial \tau} = \mathbf{f}(\mathbf{p}) + \mathcal{O}(\varepsilon). \tag{2.16}$$

Ignoring $\mathcal{O}(\varepsilon)$ terms, this nonlinear ODE system describes the spatially-decoupled dynamics to leading-order on a short time-scale. Define the quasi-steady-state, $\mathbf{p}^0$, of (2.15) to be the steady-state of this system, i.e., $\mathbf{f}(\mathbf{p}^0) = \mathbf{0}$. For a general nonlinear function $\mathbf{f}$, a solution to $\mathbf{f}(\mathbf{p}^0) = \mathbf{0}$ is not guaranteed, and here consider only $\mathbf{f}$ such that (2.16) has a steady-state solution. Due to the conservation (2.2) of motors within the cell, to solve $f_1(\mathbf{p}^0) = ... = f_n(\mathbf{p}^0) = 0$, it suffices to solve the under-determined algebraic system $f_1(\mathbf{p}^0) = ... = f_{n-1}(\mathbf{p}^0) = 0$, and automatically find $f_n(\mathbf{p}^0) = 0$. As such, generically, when a steady-state exists it can be written parametrically as $\mathbf{p}^0 = \mathbf{p}^0(\alpha)$ in terms of some scalar quantity $\alpha = \alpha(x, t)$. As there may be more than one solution to $\mathbf{f}(\mathbf{p}^0) = \mathbf{0}$, in order to

ensure that the system converges to a steady-state, I introduce the following concept of a *slow manifold*:

Definition 2.3.1 *Let* $\mathbf{p}^0(\alpha)$ *be a solution to* $f_1 = \ldots = f_{n-1} = 0$. *Then* $\mathbf{p}^0(\alpha)$ *is a slow manifold of* (2.15) *provided that the Jacobian matrix*

$$\mathbf{J} = \mathbf{J}(\alpha) \equiv \left.\begin{pmatrix} f_{1p_1} & \cdots & f_{1p_n} \\ \vdots & \ddots & \vdots \\ f_{np_1} & \cdots & f_{np_n} \end{pmatrix}\right|_{\mathbf{p}=\mathbf{p}^0(\alpha)}, \tag{2.17}$$

has all eigenvalues satisfying $\Re(\lambda) \leq 0$ *for all* α *on the range of definition. Moreover,* $\lambda = 0$ *is always an eigenvalue of* $\mathbf{J}$ *for any* α, *i.e.* $\mathbf{J}\phi = 0$ *for some* $\phi \neq \mathbf{0}$.

To motivate the need for such a criterion, consider the new time-scale $\tau = t/\varepsilon$, so that (2.15) reduces to leading-order to

$$\frac{\partial \mathbf{p}}{\partial \tau} = \mathbf{f}(\mathbf{p}). \tag{2.18}$$

In order for the ODE dynamics (2.18) to have the limiting behavior

$$\lim_{\tau \to \infty} \mathbf{p}(\tau) = \mathbf{p}^0(\alpha_0), \tag{2.19}$$

at least for initial conditions near the slow manifold $\mathbf{p}^0$, where α_0 is determined by the initial condition, the eigenvalues of the Jacobian $\mathbf{J}(\alpha)$ must satisfy $\Re(\lambda) \leq 0$ for all values of α. By differentiating

$$\mathbf{f}(\mathbf{p}^0(\alpha)) = \mathbf{0},$$

with respect to α, it follows that $\mathbf{J}$ must always have a zero eigenvalue, i.e., that

$$\mathbf{J}\phi = 0, \qquad \text{where} \qquad \phi = \frac{d\mathbf{p}^0}{d\alpha}(\alpha). \tag{2.20}$$

The remaining eigevnalues of $\mathbf{J}(\alpha)$ must satisfy $\mathrm{Re}(\lambda) < 0$, which leads to the key assumption on the nonlinearity $\mathbf{f}$.

Assumption 2.3.2 *Assume that the vector* $\mathbf{f}$ *of state transitions is such that there is exactly one solution branch* $\mathbf{p}^0(\alpha)$ *to* $\mathbf{f} = \mathbf{0}$ *for which the condition on the Jacobian* $\mathbf{J}$ *in Definition 2.3.1 holds. Further, assume that the zero eigenvalue of* $\mathbf{J}$ *has multiplicity one for any* α *on its range of definition.*

With this assumption, it is now possible to derive a nonlinear PDE for the evolution of $\alpha(x,t)$ in the quasi-steady-state $\mathbf{p}^0(\alpha)$. To do so, I propose an asymptotic expansion for

the solution to the full model consisting of correction terms of smaller order about the QSS. That is, I expand $\mathbf{p}$ as a series in ε about the quasi-steady-state as

$$\mathbf{p} = \mathbf{p}^0(\alpha) + \varepsilon \mathbf{p}^1 + \cdots . \tag{2.21}$$

Substituting this expansion into (2.15) gives

$$\mathbf{p}_t^0 + \varepsilon \mathbf{p}_t^1 + \cdots = \frac{1}{\varepsilon}\mathbf{f}(\mathbf{p}^0 + \varepsilon \mathbf{p}^1) + \mathbf{M}\mathbf{p}^0 + \varepsilon \mathbf{M}\mathbf{p}^1 + \cdots . \tag{2.22}$$

With a Taylor expansion for the nonlinear term, together with the fact that $\mathbf{f}(\mathbf{p}^0) = \mathbf{0}$, the $\mathcal{O}(1)$ terms result in:

$$\mathbf{J}\mathbf{p}^1 = \mathbf{p}_t^0 - \mathbf{M}\mathbf{p}^0. \tag{2.23}$$

By Assumption 2.3.2, there exists a unique (up to scalar multiple) ϕ such that $\mathbf{J}\phi = \mathbf{0}$. Since the eigenvalues of $\mathbf{J}$ and $\mathbf{J}^T$ are identical, $\lambda = 0$ is also an eigenvalue of $\mathbf{J}^T$ of multiplicity one. This guarantees the existence of a unique (up to scalar multiple) ψ such that $\psi^T \mathbf{J} = \mathbf{0}^T$. In fact, the eigenvalue $\psi = (1, \ldots, 1)^T$ is easily identified, as a result of the fact that (2.2) holds. From the Fredholm alternative, a solution to (2.23) exists if and only if $\psi^T(\mathbf{p}_t^0 - \mathbf{M}\mathbf{p}^0) = 0$. This solvability condition yields

$$\psi^T \mathbf{p}_t^0 = \psi^T \mathbf{M}\mathbf{p}^0, \tag{2.24a}$$

which is a scalar nonlinear PDE for $\alpha(x,t)$. This PDE (2.24a) for $\alpha(x,t)$ is called the QSS PDE and the boundary conditions for α can be readily obtained from a conservation condition (see the examples in §2.4.1, §2.4.2, and §2.4.3 below). In terms of $\alpha(x,t)$, the leading-order asymptotics

$$\mathbf{p} \sim \mathbf{p}^0(\alpha(x,t)) + \mathcal{O}(\varepsilon), \tag{2.24b}$$

then provides an approximate solution to the full system (2.15) when $t = \mathcal{O}(1)$ and away from any boundary layers near the endpoints $x = 0, 1$. The system (2.24b) is supplemented by appropriate boundary conditions (BCs). For the three-component molecular motors systems of §2.4, appropriate BCs are presented below. A boundary layer analysis for these models is presented in §2.5.

For the case where $\mathbf{f}$ is linear, as studied in [57] and [16], the $\mathcal{O}(\varepsilon)$ term in (2.24b) can be calculated explicitly. However, in the extension of the theory to allow for a nonlinear $\mathbf{f}$, it is in general analytically intractable to calculate this correction term. This difference results from the nonlinear interactions in the class of models studied here. To highlight the difference, the geometry of the QSS approximation with both linear and nonlinear reactions is illustrated in Figure 2.3. Here, p_1, p_2, and p_3 generically reference the three different

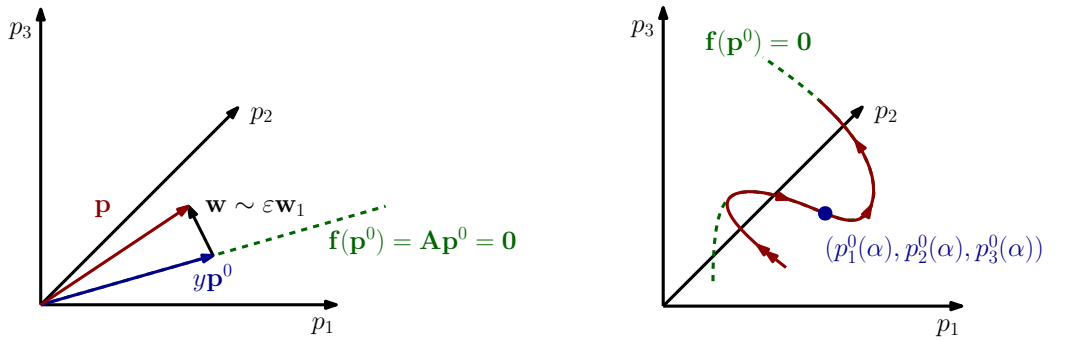

(a) Geometry with linear reactions

(b) Geometry with nonlinear reactions

Figure 2.3: Geometry of the QSS approximation in the linear and nonlinear cases. In (a), with linear interactions, the solution to the full model $\mathbf{p}$ can be decomposed into a component satisfying $\mathbf{f}(\mathbf{p}^0) = \mathbf{A}\mathbf{p}^0 = \mathbf{0}$, for reaction matrix $\mathbf{A}$ into a small correction, $\mathbf{w} \sim \varepsilon \mathbf{w}_1$. In (b), with nonlinear reactions, the full model converges to the QSS $\mathbf{f}(\mathbf{p}^0) = \mathbf{0}$ quickly. On the slow manifold, the solution is parametrized by $\alpha(x,t)$.

motor states considered in the models in §2.2. In the linear case (Figure 2.3(a)), the quasi-steady-state satisfies a linear system of equations $\mathbf{f}(\mathbf{p}^0) = \mathbf{A}\mathbf{p}^0 = \mathbf{0}$. Due to conservation, $\mathbf{A}$ has a one-dimensional kernel. As such, the solution $\mathbf{p}$ can be decomposed into two components: one component in the kernel, $y\mathbf{p}^0$, and a correction term orthogonal to the kernel, $\mathbf{w}$. In the linear case, the QSS approximation describes the time evolution of y and explains how the correction term $\mathbf{w} = \mathcal{O}(\varepsilon)$. In the nonlinear case, this projection method no longer applies, and the solution to $\mathbf{f}(\mathbf{p}^0) = \mathbf{0}$ is more complicated. Nonetheless, the QSS approximation in the nonlinear case suggests that the solution to the full model will quickly converge to the slow manifold described by $\mathbf{f}(\mathbf{p}^0) = \mathbf{0}$, and that the slow manifold can be parametrized (due to conservation) by some scalar quantity α. The QSS approximation, in the nonlinear case, describes the spatiotemporal evolution of the parameter $\alpha(x,t)$ from which the distribution of motors among the three states p_1, p_2, and p_3 can be ascertained.

2.4 Examples of the QSS Theory

In this section, the QSS reduction method is appplied to the molecular motor models that were described in §2.2.

2.4.1 QSS Reduction: Kinesin Model

As shown in Appendix A.4.1, the kinesin model (2.3) of §2.2.1 can be scaled to a system of the form (2.15) where

$$\mathbf{p} = \begin{pmatrix} p^{\mathrm{R}} \\ p^{\mathrm{L}} \\ p^{\mathrm{U}} \end{pmatrix}, \qquad \mathbf{f}(\mathbf{p}) = \begin{pmatrix} k_{\mathrm{a}} P(x) g(p^{\mathrm{U}}) - p^{\mathrm{R}} \\ k_{\mathrm{a}}(1 - P(x)) g(p^{\mathrm{U}}) - p^{\mathrm{L}} \\ -k_{\mathrm{a}} g(p^{\mathrm{U}}) + p^{\mathrm{R}} + p^{\mathrm{L}} \end{pmatrix}, \qquad \mathbf{M} = \begin{pmatrix} -\frac{\partial}{\partial x} & 0 & 0 \\ 0 & \frac{\partial}{\partial x} & 0 \\ 0 & 0 & D\frac{\partial^2}{\partial x^2} \end{pmatrix}, \tag{2.25}$$

where $D = \frac{D_0}{vL_0}$, $\varepsilon = \frac{v}{L_0 k_{\mathrm{u}}}$, and $k_{\mathrm{a}} = \frac{k_{\mathrm{b}}}{k_{\mathrm{u}}}$ if g is linear and $k_{\mathrm{a}} = \frac{k_{\mathrm{b}} g_{\mathrm{m}}}{k_{\mathrm{u}} \rho}$ or $k_{\mathrm{a}} = \frac{k_{\mathrm{b}} g_{\mathrm{m}}}{k_{\mathrm{u}} K}$ if g is either a Hill or Michaelis-Menten nonlinearity, respectively. For the case of unbiased MT distribution, with $P(x) = 0.5$, and linear binding function g, $k_{\mathrm{a}} = k_{\mathrm{b}}/k_{\mathrm{u}}$. In this case, k_{a} represents the ratio of time spent in the unbound (diffusive) state to the time spent in the bound state (directed motor motion on MTs). As shown in (A.16), if g is nonlinear, then that ratio gets modified by other parameters reflecting the nonlinear interactions.

Following the method described in §2.3, the quasi-steady-state $\mathbf{p}^0(\alpha)$ is found from the condition that $\mathbf{f} = \mathbf{0}$. Set $f_1 = f_2 = 0$ in (2.25) to get

$$p^{\mathrm{R}} = P(x) k_{\mathrm{a}} g(p^{\mathrm{U}}), \qquad p^{\mathrm{L}} = (1 - P(x))\, k_{\mathrm{a}} g(p^{\mathrm{U}}), \tag{2.26}$$

which are two nonlinear equations in three unknowns. It is convenient to parameterize the free variable by a scalar, and I set $p^{\mathrm{U}} = \alpha$. This gives the quasi-steady-state solution branch as

$$\mathbf{p}^0(\alpha) = \begin{pmatrix} P(x) k_{\mathrm{a}} g(\alpha) \\ (1 - P(x)) k_{\mathrm{a}} g(\alpha) \\ \alpha \end{pmatrix}, \tag{2.27}$$

where the parameter $\alpha = \alpha(x, t)$ is the unknown cytosolic motor density. A calculation of the Jacobian $\mathbf{J}$ in Definition 2.3.1 shows that $\mathbf{J}$ has the eigenvalues

$$\lambda = 0, \qquad \lambda = -1, \qquad \lambda = -1 - k_{\mathrm{a}} g'(\alpha). \tag{2.28}$$

Therefore, a sufficient condition for $\mathbf{p}^0$ to be a slow manifold in the sense of Definition 2.3.1 is that g is a monotonically increasing function. This condition is biologically sensible, and implies that the rate of motors binding to MT increases with the cytosolic motor concentration: the more motors are in the cytosol, the more binding can take place (increasing, possibly up to some saturation level).

To derive the QSS PDE for $\alpha(x,t)$, I use the solvability condition (2.24) to find

$$(1,1,1)\frac{\partial}{\partial t}\begin{pmatrix} P(x)k_{\rm a}g(\alpha) \\ (1-P(x))k_{\rm a}g(\alpha) \\ \alpha \end{pmatrix} = (1,1,1)\mathbf{M}\begin{pmatrix} P(x)k_{\rm a}g(\alpha) \\ (1-P(x))k_{\rm a}g(\alpha) \\ \alpha \end{pmatrix}.$$

By using (2.25) for the matrix differential operator $\mathbf{M}$, this expression reduces to

$$\frac{\partial}{\partial t}\left(k_{\rm a}g(\alpha)+\alpha\right) = -\frac{\partial}{\partial x}\left(P(x)k_{\rm a}g(\alpha)\right) + \frac{\partial}{\partial x}\left((1-P(x))k_{\rm a}g(\alpha)\right) + D\frac{\partial^2\alpha}{\partial x^2},$$

which yields the QSS PDE

$$\frac{\partial}{\partial t}\left(k_{\rm a}g(\alpha)+\alpha\right) = \frac{\partial}{\partial x}\left(D\frac{\partial\alpha}{\partial x} - (2P(x)-1)k_{\rm a}g(\alpha)\right). \tag{2.29}$$

As shown in (2.80) of Appendix 2.5, to determine the boundary conditions for (2.29), substitute (2.21) into the original boundary conditions (2.5) and retain terms up to $\mathcal{O}(\varepsilon)$. This leads to

$$\left(D\frac{\partial\alpha}{\partial x} - (2P(x)-1)k_{\rm a}g(\alpha)\right)\Big|_{x=0,1} = 0, \tag{2.30}$$

which are zero-flux boundary conditions for the QSS PDE (2.29). Moreover, by integrating the PDE (2.29) across the domain, and using the boundary conditions, the QSS PDE can be recognized as a conservation law for the total density of kinesin motors:

$$\frac{\partial}{\partial t}\int_0^1 y(x,t)\,dx = \frac{\partial}{\partial t}\int_0^1 \left(k_{\rm a}g(\alpha)+\alpha\right)\,dx = 0, \tag{2.31}$$

where, with $\mathbf{e}\equiv(1,\ldots,1)^T$, I have defined

$$y(x,t) \equiv \mathbf{e}^T\mathbf{p}^0(\alpha(x,t)) = k_{\rm a}g(\alpha(x,t)) + \alpha(x,t), \tag{2.32}$$

as the total density of kinesin motor in any state at (x,t). Therefore, from (2.31), the total motor mass satisfies $\int_0^1 y(x,t)\,dx = \int_0^1 y(x,0)\,dx$.

The QSS PDE (2.29) describes the bulk behaviour of cytosolic motors, $p^{\rm U}=\alpha$, throughout the cell, but away from any boundary layers near the domain endpoints, when $\varepsilon \ll 1$. In terms of α, using (2.27) in (2.24b) determines the behaviour of the densities of right- and left-moving kinesin motors in the bulk region away from any boundary layers near either $x=0$ or $x=1$. The boundary-layer analysis, given in Appendix 2.5, and summarized in (2.85) for the kinesin model, shows that the right-moving and left-moving motors have a classic boundary layer structure near $x=0$ and $x=1$, respectively, with a boundary layer

width of $\mathcal{O}(\varepsilon)$.

In the case where $P(x) = P$ is constant, the QSS PDE (2.29) reduces to

$$\frac{\partial \alpha}{\partial t} = \mathcal{V}(\alpha)\frac{\partial \alpha}{\partial x} + \mathcal{D}(\alpha)\frac{\partial^2 \alpha}{\partial x^2}, \tag{2.33a}$$

where the effective velocity $\mathcal{V}(\alpha)$ and effective diffusion coefficients $\mathcal{D}(\alpha)$ are defined by

$$\mathcal{V}(\alpha) \equiv \frac{(1-2P)k_{\mathrm{a}}g'(\alpha)}{k_{\mathrm{a}}g'(\alpha)+1}, \qquad \text{and} \qquad \mathcal{D}(\alpha) \equiv \frac{D}{k_{\mathrm{a}}g'(\alpha)+1}. \tag{2.33b}$$

If $P(x)$ is a smooth spatially varying function, then an additional nonlinear source/sink term in α, proportional to $P'(x)$, would appear in (2.33a).

For a general $g(\alpha)$, the QSS PDE (2.33) provides an opportunity to make predictions regarding the bulk behaviour of the molecular motors within the cell. The effective velocity and effective diffusion coefficients $\mathcal{V}(\alpha)$ and $\mathcal{D}(\alpha)$ are velocity and diffusion coefficients weighted by the fraction of time spent in directed (motor) and random (diffusive) motion, respectively. These effective velocity and diffusion coefficients depend on the model parameters.

A bias in the MT polarity proportion, P, results in a corresponding bias in the effective velocity $\mathcal{V}(\alpha)$, in such a way that $\mathcal{V}(\alpha)$ is positive when $P > \frac{1}{2}$ and is negative when $P < \frac{1}{2}$. Although α represents the density of cytosolic motors, it influences the behavior in the other states due to the assumption of rapid transitions between states. This bias agrees with the intuition that in areas where more MTs are biased to the right, more motors will be directed towards the right end of the cell. When the MT polarity is unbiased, i.e., $P = \frac{1}{2}$, then the QSS PDE (2.33) reduces, as expected, to a nonlinear diffusion equation with no advection.

In addition, when $g(\alpha)$ is monotone increasing, $\mathcal{V}(\alpha)$ is a saturating function of k_{a} and $\mathcal{D}(\alpha)$ is a saturating function of $1/k_{\mathrm{a}}$. Increasing k_{b}, corresponding to increasing k_{a}, increases the effective velocity $\mathcal{V}(\alpha)$, while decreasing the effective diffusion coefficient $\mathcal{D}(\alpha)$. Similarly, increasing k_{u}, which decreases k_{a}, causes an increase in the effective diffusion, but decreases the effective velocity. In the molecular motor system, when $k_{\mathrm{b}} \gg k_{\mathrm{u}}$, so that $k_{\mathrm{a}} \gg 1$, the expectation is that the advective processes to dominate over diffusion as motors spend more time being transported on MTs than diffusing in the cytosol. Conversely, when $k_{\mathrm{u}} \gg k_{\mathrm{b}}$, so that $k_{\mathrm{a}} \ll 1$, we expect diffusion to dominate over advective processes, as the motors spend less time walking on MTs than diffusing in the cytosol. The parameter dependence of $\mathcal{V}(\alpha)$ and $\mathcal{D}(\alpha)$ on k_{a} in the QSS PDE (2.33) reflects this tradeoff.

In the following subsections, I will explore how specific choices of the interaction function $g(\alpha)$ and the MT polarity $P(x)$ affects the QSS PDE, and further explore the parameter-dependencies discussed briefly above.

Saturated binding model

Consider the kinesin model with a saturated binding rate:

$$g(\alpha) \equiv \frac{\alpha}{1+c\alpha}. \tag{2.34}$$

This choice models the basic Michaelis-Menten biochemical kinetics with $1/c$ representing the motor density at which the binding rate is $1/2$ of its maximal magnitude. This choice of g represents the idea that binding sites on MTs are limited. As cytosolic motor density α increases, those MT sites become saturated so that $g \to 1$. When $c = 0$, the binding rate is linear and the model reduces to that studied in [16].

From (2.27), the quasi-steady-state $\mathbf{p}^0(\alpha)$ for this saturated binding kinesin model with constant polarity P is

$$\mathbf{p}^0(\alpha) = \begin{pmatrix} P\frac{k_a\alpha}{(1+c\alpha)} \\ (1-P)\frac{k_a\alpha}{(1+c\alpha)} \\ \alpha \end{pmatrix}. \tag{2.35}$$

Since $g(\alpha)$ is monotone increasing, the condition in Definition 2.3.1 holds, and $\mathbf{p}^0(\alpha)$ is a slow manifold. Therefore, from (2.29), the QSS PDE for $\alpha(x,t)$ reduces to

$$\frac{\partial}{\partial t}\left(\frac{k_a\alpha}{(1+c\alpha)} + \alpha\right) = \frac{\partial}{\partial x}\left(D\frac{\partial \alpha}{\partial x} - (2P-1)\frac{k_a\alpha}{(1+c\alpha)}\right). \tag{2.36}$$

Using (2.30), and as shown in (2.80) of §2.5, this QSS PDE inherits its zero-flux boundary conditions from the full system as

$$D\frac{\partial \alpha}{\partial x} - (2P-1)\frac{k_a\alpha}{(1+c\alpha)} = 0, \qquad \text{at} \quad x = 0, 1. \tag{2.37}$$

To compare the QSS approximation with numerical approximations of the full kinesin model (2.15) with (2.25) and (2.34), the initial condition $\alpha(x,0) = \alpha_0$ needs to be chosen such that the total density y is the same for the full system and the QSS PDE. Conservation of mass with the initial condition $p^R = 0$, $p^L = 0$ and $p^U = 1$ at $t = 0$ for the full system implies that

$$\int_0^1 \left(p^R(x,t) + p^L(x,t) + p^U(x,t)\right)\, dx = 1, \tag{2.38}$$

for all t. Recall that the QSS PDE is a conservation law for $y(x,t) = k_a g(\alpha) + \alpha$, which is the total amount of kinesin in the cell. Therefore, one correct initial condition is to choose α_0 to be the unique solution of

$$y(x,0) = k_a g(\alpha_0) + \alpha_0 = 1. \tag{2.39}$$

The steady-state solution $\alpha(x)$ of the QSS PDE (2.36) is the solution to the nonlocal problem

$$\frac{\partial \alpha}{\partial x} = \frac{k_{\mathrm{a}}}{D}(2P-1)g(\alpha), \qquad \int_0^1 \left(k_{\mathrm{a}} g(\alpha) + \alpha\right) dx = 1, \tag{2.40}$$

where $g(\alpha)$ is defined in (2.34). There are a few special cases for which explicit solutions to (2.40) can be found. Explicit solutions can be found if $\frac{1}{g(\alpha)}$, $P(x)$, and $g(\alpha)$ are integrable (using separation of variables to solve the differential equation). In particular, when $P = 0.5$, so that $\alpha = \alpha_c$, where α_c is a constant, (2.40) reveals that

$$\alpha_c = \frac{1}{k_{\mathrm{a}}+1}, \quad (c=0); \qquad \alpha_c = \frac{1}{2c}\left(c - (k_{\mathrm{a}}+1) + \sqrt{(c-(k_{\mathrm{a}}+1))^2 + 4c}\right), \quad (c>0). \tag{2.41}$$

For the linear binding case $c = 0$, where $k_{\mathrm{a}} = k_{\mathrm{b}}/k_{\mathrm{u}}$, observe that the expression for α_c is

$$\alpha_c = \frac{\frac{1}{k_{\mathrm{b}}}}{\frac{1}{k_{\mathrm{u}}} + \frac{1}{k_{\mathrm{b}}}}.$$

which represents the fraction of time spent in the unbound state (k_{b} gives the rate at which a freely diffusing motor binds to MTs, so $\frac{1}{k_{\mathrm{b}}}$ gives the mean residence time in the unbound state). In addition, for linear binding where $c = 0$ so that $g(\alpha) = \alpha$, then $\alpha(x) = \alpha_c e^{\beta x}$ where $\beta \equiv (2P-1)k_{\mathrm{a}}/D$. Substituting this form into the nonlocal condition of (2.40) gives

$$\alpha(x) = \alpha_c e^{\beta x}, \qquad \text{where} \qquad \alpha_c = \frac{\beta}{(k_{\mathrm{a}}+1)}\frac{1}{(e^{\beta}-1)}, \qquad \beta = \frac{(2P-1)k_{\mathrm{a}}}{D}. \tag{2.42}$$

When the MT polarity $P \neq 0.5$ is also constant across the cell, this case reduces to simple exponential distributions of all kinesin states; that distribution is biased towards the left ($P < 0.5$) or towards the right ($P > 0.5$), as previously described in [16]. However, in general, the solution to the nonlocal problem (2.40) must be obtained numerically. As shown in Appendix A.2, by recasting this nonlocal problem into an initial value problem, its solution can be computed using a simple numerical shooting procedure.

In Figure 2.4(a-d), numerical approximations of the steady-state solution to the full transport model (dashed) and the QSS PDE (solid) for both linear binding ($c = 0$) and saturated nonlinear binding ($c = 1$), for two constant values of the MT polarity are shown. For $P = 0.5$, and for $c = 0$ and $c = 1$, the advection term in (2.33) vanishes, leaving purely diffusive motion. For $P = 0.6$, the MT polarity is biased to the right. Consequently, the distributions of bound and cytosolic motors are also biased towards the right end of the cell at $x = 1$. From Figure 2.4(c,d), observe that the saturated binding term with $c = 1$ slows the rate at which kinesin leaves the cytosolic compartment, causing more kinesin to be sequestered in the middle of the cell. Further observe that the QSS approximation is not

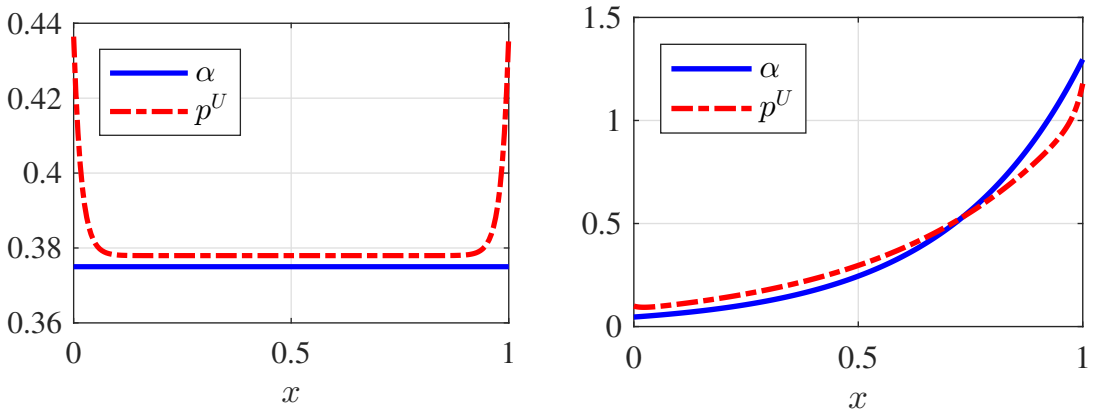

(a) $P = 0.5$, $c = 0$

(b) $P = 0.6$, $c = 0$

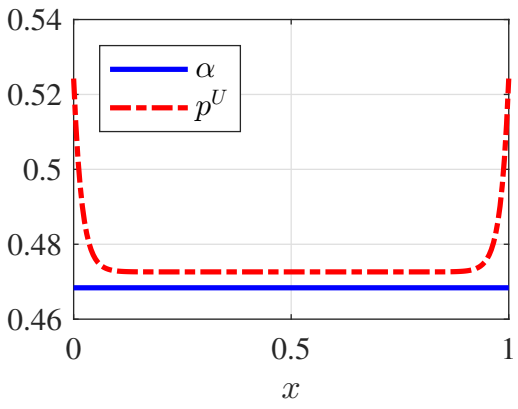

(c) $P = 0.5$, $c = 1$

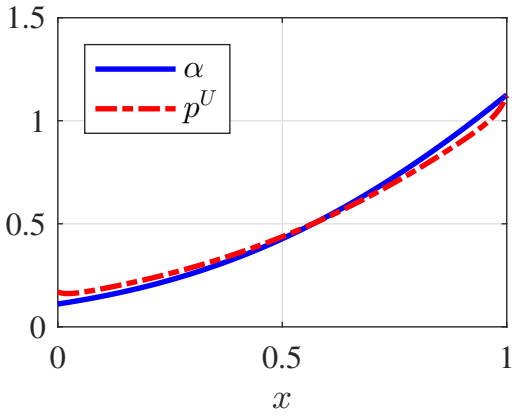

(d) $P = 0.6$, $c = 1$

Figure 2.4: Effect of nonlinear binding and microtubule polarity. A comparison for $P = 0.5$ (unbiased MT polarity, left panels) and for $P = 0.6$ (MT biased to the right, right panels) of the steady-state cytosolic density $p^{\mathrm{U}}(x)$ (dashed curves) of the full model (2.15), (2.25), and (2.34), with the steady-state $\alpha(x)$ (solid curves) from the QSS PDE (2.36). (a,b) linear binding ($c = 0$). (Results in agreement with [16]). (c,d) Saturated nonlinear binding with $c = 1$. The parameters are $k_{\mathrm{a}} = 5/3$, $\varepsilon = 0.02$, and $D = 0.1$. The total mass was initially fixed at $\int_0^1 y(x,t)\,dx = 1$, and is preserved in time. Notice the different vertical scales between (a) and (b), and between (c) and (d). The QSS approximation describes the bulk behaviour of the system well, but does not capture the boundary behaviour.

valid in thin boundary layers near the two edges of the cell. These boundary layers result from the reduction of the full three-equation model with four boundary conditions, to a single PDE with two boundary conditions. The results from the boundary layer analysis given in (2.85) of §2.5 show that the unbound kinesin motor density p^{U} near the two boundaries differs from its outer approximation $p^{\mathrm{U}} \sim \alpha$ by an error $\mathcal{O}(\varepsilon/D)$.

In Figure 2.5, I compare the steady-state solution to the QSS approximation in the linear binding ($c = 0$) and saturated binding case ($c = 1$), for the parameter range where

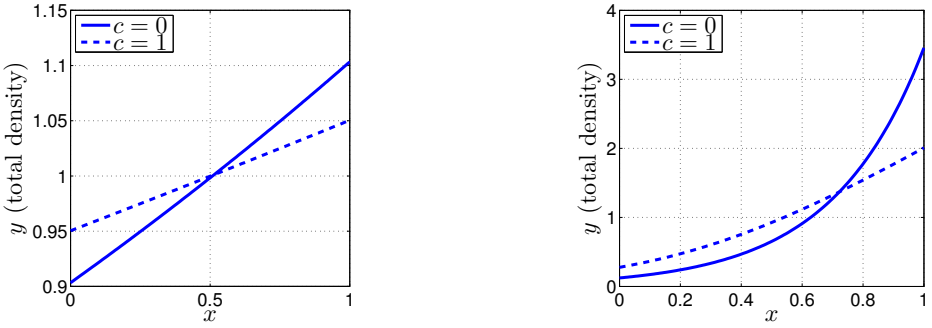

(a) $k_{\mathrm{a}} = 0.1$ (b) $k_{\mathrm{a}} = 5/3$

Figure 2.5: Effect of the relative magnitudes of binding and unbinding rates $k_{\mathrm{b}}, k_{\mathrm{u}}$. Steady-state solutions $y(x) = \mathbf{e}^T \mathbf{p}^0(\alpha(x))$, obtained from the steady-state $\alpha(x)$ of the QSS PDE (2.36) with linear binding ($c = 0$, solid) and saturated binding ($c = 1$, dashed) when $k_{\mathrm{a}} < 1$ (a) and $k_{\mathrm{a}} > 1$ (b). The other parameters are $P = 0.6$, and $D = 0.1$, and the total mass was $\int_0^1 y(x)\, dx = 1$. In general, saturated binding results in a shallower gradient of motors across the cell. The steady-state behavior illustrates the effects of k_{b} and k_{u}. For example, for large k_{u} (relative to k_{b}) as in (a) where $k_{\mathrm{a}} = 0.1$, the effective velocity, $\mathcal{V}(\alpha)$, is much smaller than the effective diffusion coefficient, $\mathcal{D}(\alpha)$. This leads to a comparatively more uniform density of motors than in (b), where k_{b} is larger than k_{u}, and the advection term dominates.

$k_{\mathrm{a}} < 1$ (a) and $k_{\mathrm{a}} > 1$ (b) with $P = 0.6$. In general, saturated binding results in a shallower gradient of cytosolic motors across the cell. This result agrees with the intuition that saturated binding restricts the rate of binding for large motor density. This consequently restricts the total number of motors walking to the right-end of the cell ($P = 0.6$), and in turn, saturated binding restricts the total number of motors that accumulate at the cell end.

Saturated binding with a spatially variable MT polarity

Next, consider a spatially varying MT polarity throughout the cell, $P = P(x)$, in the corresponding system of transport equations for the case of saturated binding. In this case, the quasi-steady-state $\mathbf{p}^0(\alpha)$ is

$$\mathbf{p}^0(\alpha) = \begin{pmatrix} P(x) k_{\mathrm{a}} g(\alpha) \\ (1 - P(x)) k_{\mathrm{a}} g(\alpha) \\ \alpha \end{pmatrix}, \qquad g(\alpha) = \frac{\alpha}{1 + c\alpha}. \tag{2.43}$$

The QSS PDE, from (2.29), is

$$\frac{\partial}{\partial t}\left(\frac{k_{\mathrm{a}}\alpha}{(1+c\alpha)}+\alpha\right)=\frac{\partial}{\partial x}\left(D\frac{\partial\alpha}{\partial x}-(2P(x)-1)\,\frac{k_{\mathrm{a}}\alpha}{(1+c\alpha)}\right). \tag{2.44}$$

Observe that the sign of the advection term depends only on the sign of $(2P(x)-1)$. If $P(x)<0.5$, then advection is to the left, while if $P(x)>0.5$, then advection is to the right. Biologically, if the MT polarity changes across the cell, the bulk molecular motor behaviour will change correspondingly. If $P(x)>0.5$ on some subinterval, the MT bias is to the right. This leads to a collection of motors walking to the right in this subinterval. Moreover, if $P(x)<0.5$ on some subinterval, then the bulk movement of motors in this subinterval is to the left.

To explore the effect of non-constant $P(x)$ on the QSS PDE (2.44), consider two hypothetical MT polarity functions. First, consider

$$P(x)=\frac{1}{2}\left[1-\tanh\left(x-\frac{1}{2}\right)\right], \tag{2.45}$$

for which $P(0)\approx 1$, $P(1)\approx 0$, $P(\frac{1}{2})=\frac{1}{2}$, and $P'(x)=-\frac{1}{2}\operatorname{sech}^2(x-\frac{1}{2})$. For $x\in[0,\frac{1}{2})$, we have $P(x)>\frac{1}{2}$, which indicates that the MT polarity is biased to the right in the left part of the cell. Similarly, for $x\in(\frac{1}{2},1]$, $P(x)<\frac{1}{2}$, which indicates that the MT polarity is biased to the left in the right part of the cell. As a result of this MT polarity bias, the effective velocity coefficient in the QSS PDE changes signs at $x=\frac{1}{2}$. From this, it is expected that kinesin will walk toward the centre of the cell and become "trapped" there. In Figure 2.6 (a) depicts an aggregation of kinesin motors in the centre of the cell at steady-state as predicted by the QSS PDE for both linear ($c=0$) and saturated binding ($c=1$). The steady-state problem was solved numerically by the shooting method outlined in Appendix A.2.

Following [16] and [26], where molecular motor movement in the hyphae of the fungus *Ustilago maydis* was studied, the second choice is to consider a MT polarity bias near $x=0$ and $x=1$ that is polarized towards these cell ends, while the MTs near the cell centre point to the right and to the left with (roughly) equal probability. As a model of such a polarity consider

$$P(x)=\frac{1}{2}\left(1+\tanh\left[2\left(x-\frac{1}{2}\right)\right]\right). \tag{2.46}$$

From the numerical computations of the steady-state of the QSS PDE, as shown in Figure 2.6(b), observe that with such a $P(x)$ most of the kinesin motors are pushed towards the boundaries of the cell for both linear ($c=0$) and saturated binding ($c=1$). This results from the highly left-biased region at the left end of the cell and the highly right-biased

region at the right end of the cell. Moreover, saturated binding sequesters more kinesin in the cytosolic compartment in the middle of the cell with a non-zero density persisting throughout the cell at steady-state.

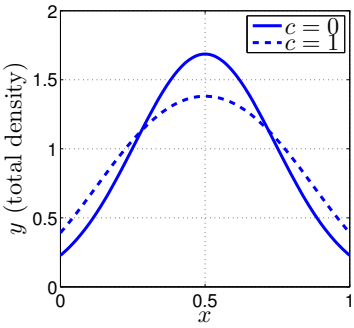

(a) $P(x) = \frac{1}{2}\left(1 - \tanh\left(x - \frac{1}{2}\right)\right)$

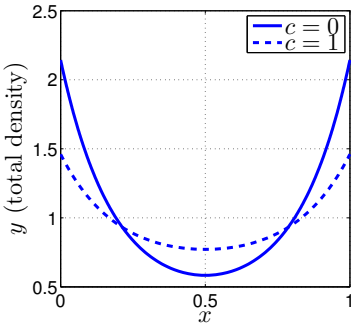

(b) $P(x) = \frac{1}{2}\left(1 + \tanh\left(2\left(x - \frac{1}{2}\right)\right)\right)$

Figure 2.6: Effects of two spatially dependent MT bias functions, $P(x)$. Steady-states $y(x) = \mathbf{e}^T\mathbf{p}^0(\alpha(x))$, obtained from the steady-state $\alpha(x)$ of the QSS PDE (2.44) with spatially varying MT polarity where (a) MT "point towards" the cell center (described by $P(x)$ in (2.45)) and (b) "point towards" the cell ends ($P(x)$ as given in (2.46)). Both panels depict linear ($c = 0$, solid) and saturated binding ($c = 1$, dashed). In (a), observe an accumulation of kinesin at the center of the cell whereas in (b) the accumulation is at the cell ends. Saturated binding sequesters more kinesin motors in the cytosolic compartment, which results in the shallower, diffusion-dominated, motor distributions in the case $c = 1$ in both (a) and (b). Other parameters are $k_a = 5/3$, and $D = 0.1$. The total mass was fixed at $\int_0^1 y(x)\,dx = 1$.

Hill function binding

Next, consider a general Hill function for the binding rate, $g(\alpha)$, given by

$$g(\alpha) = \frac{\alpha^n}{K^n + \alpha^n}, \tag{2.47}$$

where $n \geq 1$ and $K > 0$. Hill functions with $n \geq 2$ are typically used to model positive feedback or cooperative binding in biological systems. In this case, suppose that kinesin motors binding cooperatively to the MTs in such a way that for low densities of motors the binding rate is slow, at intermediate densities ($\alpha \approx K$) binding is rapid, while for high densities of motors the binding rate saturates to some maximal level. The parameter K describes the value of α at which $g(\alpha)$ reaches half of its maximum value, while the parameter n describes the "sharpness" of the switch.

With this choice (2.47) of monotonically increasing $g(\alpha)$, the quasi-steady-state slow

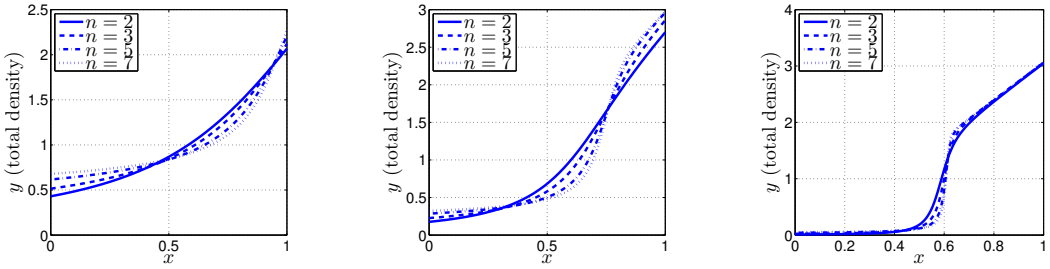

(a) $K = 1$ (b) $K = 0.5$ (c) $K = 0.1$

Figure 2.7: Effect of the Hill function parameters K and n. Steady-states $y(x) = \mathbf{e}^T\mathbf{p}^0(\alpha(x))$, obtained from the steady-state $\alpha(x)$ of the QSS PDE (2.44) with a Hill function binding rate (2.47) for $P = 0.6$. The parameter K represents the density of motors p^{U} that leads to $g(p^{\mathrm{U}}) = 1/2$ whereas the Hill coefficient n governs the "sharpness" of the Hill function. Other parameters are $k_{\mathrm{a}} = 5/3$ and $D = 0.1$. The total mass was fixed at $\int_0^1 y(x)\,dx = 1$.

manifold is given in terms of $g(\alpha)$ by (2.43). In addition, the QSS PDE is given by (2.29) with boundary conditions (2.30). Below, I numerically examine the role of the Hill parameters n and K, and discuss the effects that these parameters have on the bulk-behaviour of kinesin within the cell.

Figure 2.7 depicts numerical approximations to the steady-state solution of the QSS PDE for different values of n and K when P is fixed at $P = 0.6$. In particular, in Figure 2.7(a), steady-state solutions are shown for a fixed $K = 1$ and for increasing n. At motor density $\alpha = K$ the binding rate is half-maximal, so that $g(\alpha) < \frac{1}{2}$ for $\alpha < K$. This implies that the advection term, $k_{\mathrm{a}}(2P - 1)g(\alpha)$, remains relatively small for $\alpha < K$. This makes sense, since motors hardly bind to MT at that low density. As K decreases from panel (a) to (c) of Figure 2.7, the switch to rapid binding is made possible wherever α exceeds K. For $\alpha > K$, the advection term is near maximal resulting in an aggregation of kinesin motor at the right-end of the cell. Hence, decreasing K from the value 1 shifts the system from slow-advection to fast-advection, as seen by a comparison of the bulk distribution of motors across the cell in panels (a), (b) and (c). The parameter n controls the "sharpness" of the transition zone near $\alpha \approx K$ in the Hill function. As n increases, the approximation $g(\alpha) \approx 0$ for $\alpha < K$ and $g(\alpha) \approx 1$ for $\alpha > K$ improves. In Figure 2.7(b), $K = 0.5$. As n increases, the switch from slow-advection to fast-advection becomes shaper. Hence, for large n, in regions where the cytosolic motor density α is larger than K, advection dominates over diffusion. Increasing n results in a sharper distribution of motors across the cell in the steady state solution.

2.4.2 QSS Reduction: Kinesin-Dynein Model

As shown in Appendix A.4.2, the kinesin-dynein model (2.8) of §2.2.2 can be scaled to a system of the form (2.15), where

$$\mathbf{p} = \begin{pmatrix} p^{\mathrm{R}} \\ p^{\mathrm{L}} \\ p^{\mathrm{U}} \end{pmatrix}, \quad \mathbf{f}(\mathbf{p}) = \begin{pmatrix} k_{\mathrm{a}} Q p^{\mathrm{U}} - p^{\mathrm{R}} - k p^{\mathrm{R}} p^{\mathrm{L}} \\ k_{\mathrm{a}}(1-Q) p^{\mathrm{U}} - p^{\mathrm{L}} + k p^{\mathrm{R}} p^{\mathrm{L}} \\ p^{\mathrm{R}} + p^{\mathrm{L}} - k_{\mathrm{a}} p^{\mathrm{U}} \end{pmatrix}, \quad \mathbf{M} = \begin{pmatrix} -\frac{\partial}{\partial x} & 0 & 0 \\ 0 & v\frac{\partial}{\partial x} & 0 \\ 0 & 0 & D\frac{\partial^2}{\partial x^2} \end{pmatrix}. \tag{2.48}$$

Here the positive dimensionless parameters v, k_{a}, k, and D, are defined in terms of the original parameters of (2.8) by

$$v \equiv \frac{v_{\mathrm{l}}}{v_{\mathrm{r}}}, \qquad D \equiv \frac{D_0}{v_{\mathrm{r}} L_0}, \qquad \varepsilon \equiv \frac{v_{\mathrm{r}}}{k_{\mathrm{u}} L_0}, \qquad k_{\mathrm{a}} \equiv \frac{k_{\mathrm{b}}}{k_{\mathrm{u}}}, \qquad k \equiv \frac{k_{\mathrm{c}}\rho}{k_{\mathrm{u}}} = \frac{(k_{\mathrm{rl}} - k_{\mathrm{lr}})\rho}{k_{\mathrm{u}}}. \tag{2.49}$$

Without loss of generality, assume that $k_{\mathrm{rl}} > k_{\mathrm{lr}}$, so that $k > 0$, since the cell ends are interchangeable. It is convenient to parameterize the quasi-steady-state solution in terms of $p^{\mathrm{L}} = \alpha$. In Appendix A.4.2, I determine that there is a unique quasi-steady-state solution satisfying $\mathbf{f} = \mathbf{0}$ given by

$$\mathbf{p}^0(\alpha) = \begin{pmatrix} p^{\mathrm{R}} \\ p^{\mathrm{L}} \\ p^{\mathrm{U}} \end{pmatrix} = \begin{pmatrix} \frac{Q\alpha}{k\alpha + 1 - Q} \\ \alpha \\ \frac{1}{k_{\mathrm{a}}}\left(\alpha + \frac{Q\alpha}{k\alpha+1-Q}\right) \end{pmatrix}. \tag{2.50}$$

To determine whether this quasi-steady-state solution is a slow manifold in the sense of Definition 2.3.1, it is necessary to calculate the eigenvalues λ of the Jacobian of $\mathbf{f}$ at $\mathbf{p} = \mathbf{p}^0$. The first eigenvalue is $\lambda = 0$ and the other two eigenvalues $\lambda_\pm$ satisfy the quadratic equation

$$\lambda^2 - \sigma_1 \lambda + \sigma_2 = 0; \qquad \sigma_1 \equiv -2 - k_{\mathrm{a}} + k\left(p^{\mathrm{R}} - p^{\mathrm{L}}\right), \quad \sigma_2 \equiv 1 + k_{\mathrm{a}} + k(1+k_{\mathrm{a}})(p^{\mathrm{L}} - p^{\mathrm{R}}). \tag{2.51}$$

By using (2.50) for p^{L} and p^{R}, σ_1 and σ_2 are given explicitly:

$$\sigma_1 = -2 - k_{\mathrm{a}} - k\alpha H(Q), \quad \sigma_2 = 1 + k_{\mathrm{a}} + k\alpha(1+k_{\mathrm{a}})H(Q); \tag{2.52}$$

where $H(Q) \equiv 1 - \frac{Q}{1+k\alpha-Q}$. A necessary and sufficient condition for $\mathrm{Re}(\lambda_\pm) < 0$ is that $\sigma_1 < 0$ and $\sigma_2 > 0$ in (2.52). In Appendix A.4.2, I show that these inequalities hold for any Q on $0 \le Q \le 1$. Therefore, $\mathbf{p}^0$ is a slow manifold in the sense of Definition 2.3.1.

Next, to determine the QSS PDE for $\alpha(x,t)$ governing the dynamics on the slow manifold, it is necessary to calculate the terms in the solvability condition (2.24a). This leads

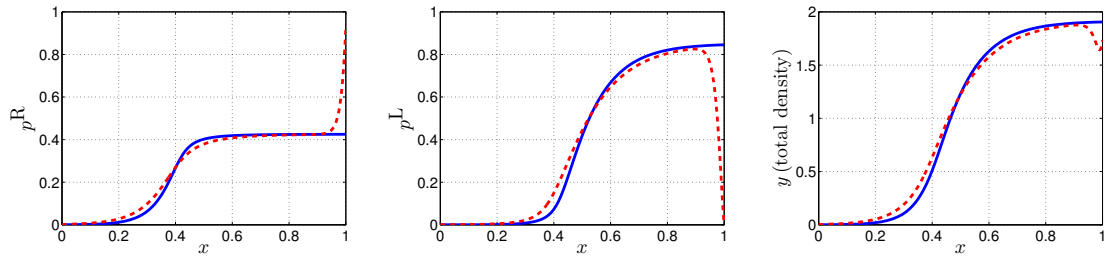

(a) p^{R} versus x (b) p^{L} versus x (c) y versus x

Figure 2.8: Comparison of the full solution with the QSS solution. Shown are the steady-state of the full model (2.15) and (2.48) (dashed curve) for $\varepsilon = 0.02$ and the solution of the QSS PDE (2.53) (solid curve) for p^{R} (a), p^{L} (b), and the total density y at position x. The parameters are $D = 0.1$, $k_{\mathrm{a}} = 2$, $k = 2$, $Q = 0.9$, and $v = 0.5$. The total mass in the cell was fixed at $\int_0^1 y(x)\,dx = 1$. The QSS approximation agrees well with the full solution except near the boundary layers at the ends of the cell.

to the QSS PDE for $\alpha(x,t)$, given by

$$\frac{\partial}{\partial t}\left(\left(1+\frac{1}{k_{\mathrm{a}}}\right)\left(\frac{k\alpha+1}{k\alpha+1-Q}\right)\alpha\right) = \frac{\partial}{\partial x}\left(\mathcal{V}(\alpha)\alpha + \mathcal{D}(\alpha)\frac{\partial \alpha}{\partial x}\right), \tag{2.53a}$$

where the "effective transport rate" and the "effective rate of diffusion" are given by

$$\mathcal{V}(\alpha) = \left(v - \frac{Q}{k\alpha+1-Q}\right), \qquad \mathcal{D}(\alpha) = \frac{D}{k_{\mathrm{a}}}\left(1 + \frac{(1-Q)Q}{(k\alpha+1-Q)^2}\right), \tag{2.53b}$$

together with the zero-flux boundary conditions (see (2.80) of §2.5)

$$\mathcal{V}\alpha + \mathcal{D}\frac{\partial \alpha}{\partial x} = 0, \qquad \text{at} \quad x = 0, 1. \tag{2.53c}$$

In Figure 2.8, numerical results for the motor densities p^{R}, p^{L}, and the total density y, in the steady-state solution of the full transport model [(2.15) and (2.48) with $\varepsilon = 0.02$] and in the corresponding steady-state of the QSS PDE (2.53) are compared. As shown, the full solution and the QSS solution agree well in the middle of the cell, but, as before, the QSS does not capture the boundary layer behavior near the cell ends. §2.5 provides a qualitative phase-plane analysis of the boundary-layer solutions and, in particular, predicts that $p^{\mathrm{R}} \approx 0.82$ at $x = 1$, which agrees well with the result in Figure 2.8(a).

How do solutions of the QSS PDE (2.53) behave? What is the role of parameters in the original model in the overall transport process? First observe from (2.50) that the density

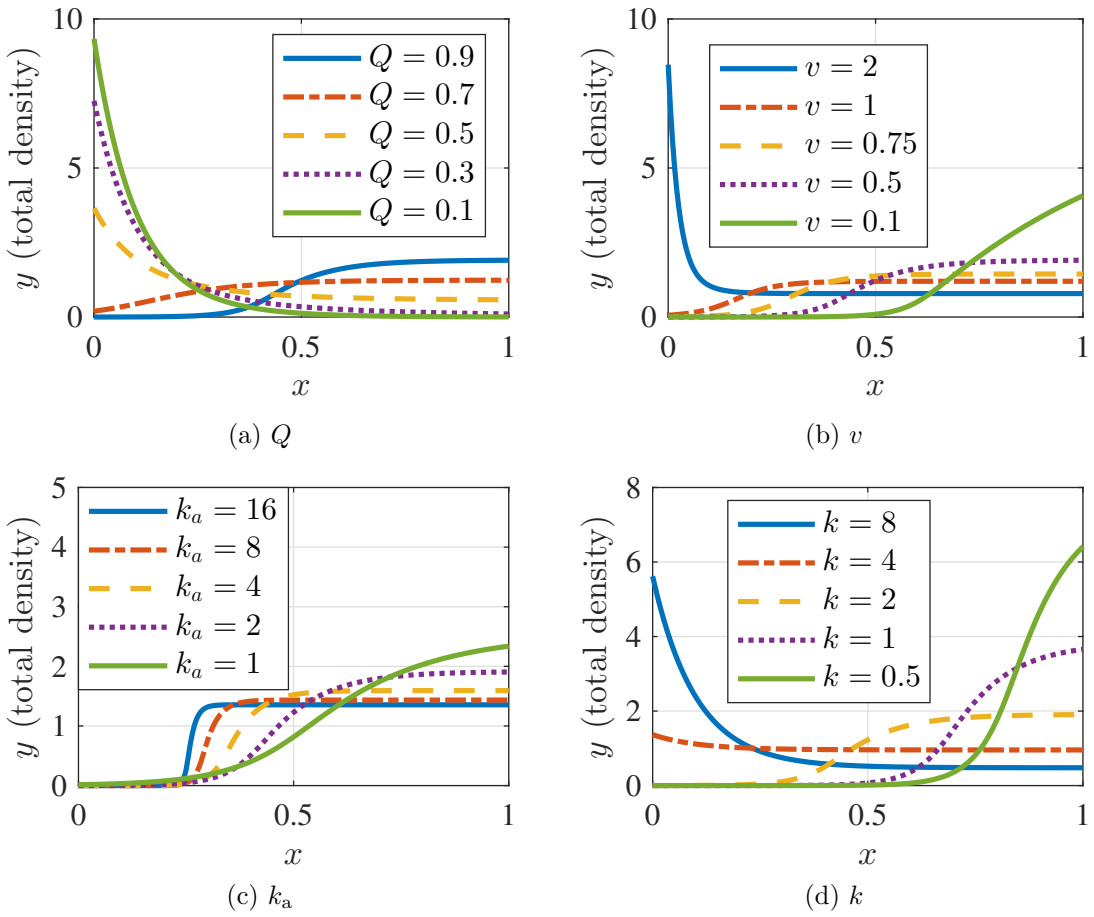

(a) Q (b) v

(c) k_{a} (d) k

Figure 2.9: The effect of parameters Q, v, k_{a}, k on the total density. The total density is $y(x) = \mathbf{e}^T \mathbf{p}^0(\alpha(x))$, obtained from the steady-state $\alpha(x)$ of the QSS PDE (2.53). Baseline parameters are $k = 2$, $k_{\mathrm{a}} = 2$, $D = 0.1$, $v = 0.5$, $Q = 0.9$. This value of Q biases the bulk motor distribution to the right (top labelled curve in (a)). In (a), decreasing the binding bias Q, (probability of binding to the right) results in a shift in right-biased movement to left-biased movement. In (b), an increase in v (the ratio of the velocites of left-moving to right-moving complexes) biases net movement towards the left. In (c), an increase in k_{a} (which represents the ratio of binding to unbinding rates $k_{\mathrm{b}}/k_{\mathrm{u}}$) sharpens the interface between the regions of high- and low-density of motors. In (d), increasing the turning rate constant, k, also biases the net movement to the left end of the cell. The total mass was set to $\int_0^1 y(x)\,dx = 1$.

of freely diffusing motors is a weighted average of the left-moving and right-moving motors with weight $1/k_{\mathrm{a}}$ (ratio of mean time spent bound to mean time spent freely diffusing). The density of right-moving motors at QSS, given by $\frac{Q\alpha}{k\alpha+1-Q}$, saturates up to Q/k, as the density of left-moving motors, α, increases. From (2.53a) the sign of the effective transport velocity $\mathcal{V}$ in (2.53b) determines the direction of motion, with the motion being to the left

if this quantity is positive. The net movement is to the left when the density of left-moving motors, α, exceeds a threshold, i.e., when $\alpha > \frac{v(Q-1)+Q}{vk}$. For example, with fixed v and k, changing Q (which is the probability that a freely diffusing motor complex binds into the right-moving state) will change this condition. Lowering Q increases the probability that a freely diffusing motor binds into the left-moving state, which should bias the net advection to the left. The "effective diffusivity" $\mathcal{D}$ of the system in (2.53b) is influenced by the parameters D, $k_{\rm a}$, k and Q. Increasing $k_{\rm a}$ decreases the effective diffusion coefficient in (2.53a), which should lead to steeper solution profiles across the cell (as usual, increasing D has the opposite effect). Increasing the turning parameter k also decreases the diffusivity of the motors. The binding bias parameter Q appears in the diffusion coefficient in two ways. First, as $Q \to 0$ or $Q \to 1$, the diffusion coefficient approaches the limiting value $D/k_{\rm a}$. Second, there exists a critical Q-value that maximizes the effective rate of diffusion, given a fixed motor density α and fixed k (this critical Q-value is $\frac{k\alpha+1}{2\alpha k+1}$).

In Figure 2.9, I plot steady-state solutions to the QSS PDE (2.53) for a range of values of several parameters. These steady-states are readily calculated numerically by using a numerical shooting method (see Appendix A.2). The top labelled curve in panel (a) is produced with a baseline parameter set ($k = 2$, $k_{\rm a} = 2$, $D = 0.1$, $v = 0.5$, $Q = 0.9$) to which parameter variations can be compared. The total mass of kinesin-dynein complex is fixed as $\int_0^1 y(x)\,dx = 1$, where $y(x) = \mathbf{e}^T\mathbf{p}^0(\alpha(x))$ and $\mathbf{p}^0$ is defined in (2.50). Decreasing the probability, Q, of binding to the right-moving state (panel (a)) allows for more freely diffusing motors to bind to the left-moving state, and a shift in right-biased movement to left-biased movement. Increasing the velocity ratio of left-moving to right-moving motor complexes v (panel (b)), biases net movement towards the left end of the cell, as expected. In (c), an increase in $k_{\rm a}$, which decreases the "effective diffusivity" $\mathcal{D}$, sharpens the interface between the regions of high- and low-density of stalled motors. In (d), increasing the turning rate constant, k, also biases the net movement to the left end of the cell. Note that high values of k are required to shift the behaviour from right-biased to left-biased due to the high baseline Q-value ($Q = 0.9$).

2.4.3 QSS Reduction: Myosin Model

Next, I study the QSS reduction of the myosin model given in (A.24). The analysis of this model will differ from that of the previous two models in that there are two possible quasi-steady-state solutions. In addition, the boundary-layer behaviour will play a nontrivial role in the dynamics.

As shown in Appendix A.4.3, the myosin model (2.11) of §2.2.3 can be scaled to a system

of the form (2.15) by

$$\mathbf{p} = \begin{pmatrix} p^{\mathrm{W}} \\ p^{\mathrm{B}} \\ p^{\mathrm{U}} \end{pmatrix}, \qquad \mathbf{f}(\mathbf{p}) = \begin{pmatrix} -k_{\mathrm{bw}} \left(p^{\mathrm{B}}\right)^2 p^{\mathrm{W}} + k_{\mathrm{b}} p^{\mathrm{U}} - p^{\mathrm{W}} \\ k_{\mathrm{bw}} \left(p^{\mathrm{B}}\right)^2 p^{\mathrm{W}} - p^{\mathrm{B}} \\ p^{\mathrm{B}} + p^{\mathrm{W}} - k_{\mathrm{b}} p^{\mathrm{U}} \end{pmatrix}, \qquad \mathbf{M} = \begin{pmatrix} -\frac{\partial}{\partial x} & 0 & 0 \\ 0 & v\frac{\partial}{\partial x} & 0 \\ 0 & 0 & D\frac{\partial^2}{\partial x^2} \end{pmatrix}, \tag{2.54}$$

where the dimensionless parameters v, D, ε, k_{bw}, and k_{b} are defined by

$$v \equiv \frac{v_{\mathrm{b}}}{v_{\mathrm{w}}}, \qquad D \equiv \frac{D_{\mathrm{f}}}{v_{\mathrm{w}} L_0}, \qquad \varepsilon \equiv \frac{v_{\mathrm{w}}}{k_{\mathrm{u}} L_0}, \qquad k_{\mathrm{bw}} \equiv \frac{\hat{k}_{\mathrm{bw}} \rho^2}{k_{\mathrm{u}}}, \qquad k_{\mathrm{b}} \equiv \frac{\hat{k}_{\mathrm{b}}}{k_{\mathrm{u}}}. \tag{2.55}$$

Upon setting the nonlinear kinetics in the scaled myosin model (A.24a) and (A.24c) to zero, one obtains the two equations:

$$k_{\mathrm{bw}} \left(p^{\mathrm{B}}\right)^2 p^{\mathrm{W}} - p^{\mathrm{B}} = 0, \qquad -k_{\mathrm{b}} p^{\mathrm{U}} + p^{\mathrm{B}} + p^{\mathrm{W}} = 0. \tag{2.56}$$

The two possible solutions to the first equation in (2.56) are $p^{\mathrm{B}} = 1/\left[k_{\mathrm{bw}} p^{\mathrm{W}}\right]$ and $p^{\mathrm{B}} = 0$. In the latter case, the motors equilibrate between freely diffusing and walking on MT, with no motors in the bound, stalled state. In the former case, there is some proportion of motors that are stalled. I analyze each of these cases in turn.

Type I quasi-steady-states: $p^{\mathrm{B}} \equiv 0$

In the case, with $p^{\mathrm{B}} \equiv 0$, let p^{U} be the free parameter and set $p^{\mathrm{U}} = \beta(x,t)$. This yields the quasi-steady-state

$$\mathbf{p}^0(\beta) = \begin{pmatrix} p^{\mathrm{W}} \\ p^{\mathrm{B}} \\ p^{\mathrm{U}} \end{pmatrix} = \begin{pmatrix} k_{\mathrm{b}}\beta \\ 0 \\ \beta \end{pmatrix}. \tag{2.57}$$

For $\mathbf{p}^0$, I readily calculate that the eigenvalues λ of the Jacobian of the kinetics $\mathbf{f}(\mathbf{p})$ at $\mathbf{p} = \mathbf{p}^0$ are $\lambda = 0$, $\lambda = -1$, and $\lambda = -1 - k_{\mathrm{b}}$. Therefore, (2.57) is a slow manifold in the sense of Definition 2.3.1. The QSS PDE for $\beta(x,t)$ is calculated by expanding the solvability condition (2.24a). This yields the linear PDE

$$(k_{\mathrm{b}} + 1)\frac{\partial \beta}{\partial t} = \frac{\partial}{\partial x}\left[D\frac{\partial \beta}{\partial x} - k_{\mathrm{b}}\beta\right], \quad 0 < x < 1; \qquad D\frac{\partial \beta}{\partial x} = k_{\mathrm{b}}\beta, \quad \text{on} \quad x = 0, 1. \tag{2.58}$$

The steady-state solution $\beta_s(x)$ of (2.58) having a unit mass, so that $\int_0^1 (k_{\mathrm{b}} + 1)\beta \, dx = 1$, is simply

$$\beta_s(x) = \left(\frac{k_{\mathrm{b}}}{(k_{\mathrm{b}} + 1)D}\right) \frac{e^{k_{\mathrm{b}}(x-1)/D}}{1 - e^{-k_{\mathrm{b}}/D}}, \tag{2.59}$$

which determines the steady-state $\mathbf{p}^0[\beta_s(x)]$ from (2.57).

Moreover, since the time-dependent QSS PDE (2.58) is linear, it is readily solved by separation of variables as

$$\beta(x,t) = \beta_s(x) + e^{k_\mathrm{b}x/D}\sum_{n=1}^{\infty} c_n e^{-\lambda_n D t/(k_\mathrm{b}+1)}\Phi_n(x), \tag{2.60}$$

where c_n for $n \geq 1$ are coefficients defined in terms of the initial data $\beta(x,0)$. Here $\lambda = \lambda_n > 0$ and $\Phi = \Phi_n(x)$ are the positive eigenvalues and eigenfunctions of the Sturm-Liouville problem

$$\big(w(x)\Phi'\big)' + \lambda w(x)\Phi = 0, \quad 0 < x < 1; \qquad \Phi'(0) = \Phi'(1) = 0, \quad w(x) \equiv e^{k_\mathrm{b}x/D}. \tag{2.61}$$

Since the myosin model (A.24) is linear when $p^\mathrm{B} \equiv 0$, the boundary-layer analysis near $x = 0$ and $x = 1$ is routine for this quasi-steady-state. At steady-state, and with $p^\mathrm{B} = 0$ in (A.24), it follows from (2.82) that there is no boundary-layer near $x = 1$. By solving the boundary layer equations (2.83) near $x = 1$, the leading-order uniform steady-state approximation is

$$p^\mathrm{W} = k_\mathrm{b}A\left(e^{k_\mathrm{b}x/D} - e^{-x/\varepsilon}\right), \qquad p^\mathrm{U} = Ae^{k_\mathrm{b}x/D}, \qquad \text{where} \qquad A \equiv \frac{k_\mathrm{b}}{D(k_\mathrm{b}+1)}\frac{e^{-k_\mathrm{b}/D}}{1-e^{-k_\mathrm{b}/D}}. \tag{2.62}$$

By (2.62), p^U is an exponentially increasing function. By comparison, p^W has a rapidly decaying correction factor (since $1/\varepsilon$ is large in the second exponential), which produces a small "knee" in its graph, Figure 2.10 (a), close to the origin.

Numerical results reveal that the steady-state (2.62) with $p^\mathrm{B} = 0$ is realizable from the long-time dynamics of the full transport model (A.24) with different initial states for p^W, p^B, and p^U at $t = 0$. Figure 2.10 depicts the numerical solution p^W and p^U to (A.24) at $t = 130$ for the parameter values $\varepsilon = 0.02$, $k_\mathrm{b} = 0.3$, $k_\mathrm{bw} = 0.5$, and $D = 0.1$, when the initial densities are spatially uniform and equally-partitioned as $p^\mathrm{W} = p^\mathrm{B} = p^\mathrm{U} = 1/3$ at $t = 0$. The full dynamics quickly drives p^B to zero as t increases. From Figure 2.10, note that at $t = 130$ the computed motor densities p^W and p^U from the full model agree well with the steady-state asymptotic result (2.62).

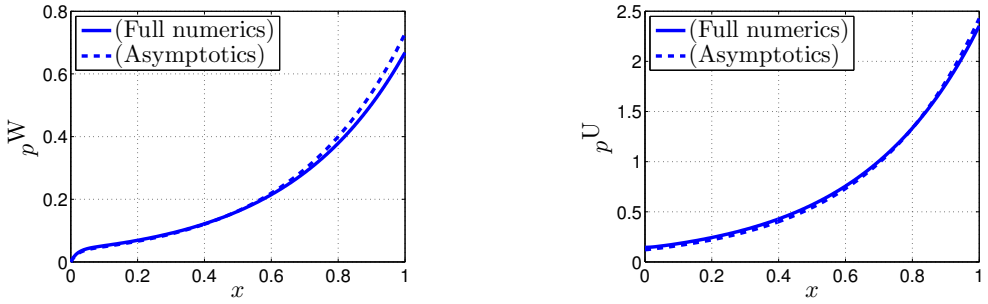

(a) p^{W} versus x (b) p^{U} versus x

Figure 2.10: Full numerical vs. asymptotic solutions to the myosin model. Shown are steady-state motor densities (solid curves) p^{W} (a) and p^{U} (b) (shown at $t = 130$) computed from the full time-dependent myosin transport model (A.24) for $\varepsilon = 0.02$ and with the spatially uniform initial condition $p^{\mathrm{W}} = p^{\mathrm{B}} = p^{\mathrm{U}} = 1/3$ at $t = 0$, so that the total mass is unity. The parameters are $k_{\mathrm{b}} = 0.3$, $k_{\mathrm{bw}} = 0.5$, and $D = 0.1$. Although $p^{\mathrm{B}} > 0$ at $t = 0$, the dynamics quickly drives p^{B} to zero as t increases. The dashed curves in (a) and (b) are the asymptotic results (2.62) for the steady-state, which compare favorably with the numerical results.

Type II quasi-steady-states: $p^{\mathrm{B}} > 0$

It is also possible to let $p^{\mathrm{B}} \neq 0$ be the free parameter, and define $p^{\mathrm{B}} = \alpha(x,t)$. Upon solving (2.56) for p^{W} and p^{U}, the quasi-steady-state solution for (A.24) is given by

$$\mathbf{p}^0(\alpha) = \begin{pmatrix} p^{\mathrm{W}} \\ p^{\mathrm{B}} \\ p^{\mathrm{U}} \end{pmatrix} = \begin{pmatrix} \frac{1}{k_{\mathrm{bw}}\alpha} \\ \alpha \\ \frac{1}{k_{\mathrm{b}}}\left(\alpha + \frac{1}{k_{\mathrm{bw}}\alpha}\right) \end{pmatrix}. \tag{2.63}$$

The eigenvalues λ of the Jacobian of the kinetics $\mathbf{f}(\mathbf{p})$ at $\mathbf{p} = \mathbf{p}^0$ reveal whether $\mathbf{p}^0$ is a slow manifold in the sense of Definition 2.3.1. One eigenvalue is $\lambda = 0$, while the remaining two eigenvalues $\lambda_\pm$ satisfy the quadratic equation $\lambda^2 - \sigma_1\lambda + \sigma_2 = 0$, where σ_1 and σ_2 are given by

$$\sigma_1 = -2 - k_{\mathrm{b}} + 2k_{\mathrm{bw}}p^{\mathrm{B}}p^{\mathrm{W}} - k_{\mathrm{bw}}\left(p^{\mathrm{B}}\right)^2, \tag{2.64a}$$

$$\sigma_2 = \left(1 - 2k_{\mathrm{bw}}p^{\mathrm{B}}p^{\mathrm{W}}\right)\left(1 + k_{\mathrm{b}} + k_{\mathrm{bw}}(p^{\mathrm{B}})^2\right) + 2k_{\mathrm{bw}}^2(p^{\mathrm{B}})^3p^{\mathrm{W}} - k_{\mathrm{b}} + k_{\mathrm{b}}\left(1 + k_{\mathrm{bw}}(p^{\mathrm{B}})^2\right), \tag{2.64b}$$

with p^{B} and p^{W} as given by the entries in (2.63). Upon using (2.63) for $\mathbf{p}^0$, σ_1 and σ_2 are

$$\sigma_1 \equiv -k_{\mathrm{b}} - \alpha^2 k_{\mathrm{bw}}, \qquad \sigma_2 \equiv (k_{\mathrm{b}} + 1)\left(\alpha^2 k_{\mathrm{bw}} - 1\right). \tag{2.65}$$

Since $\sigma_1 < 0$, a necessary and sufficient condition for $\mathrm{Re}(\lambda_\pm) < 0$ is that $\sigma_2 > 0$ in (2.65). From the expression for σ_2 in (2.65), it follows that $\mathbf{p}^0$ is a slow manifold whenever $k_{\mathrm{bw}} > 1/\alpha^2$.

For $k_{\mathrm{bw}} > 1/\alpha^2$, the QSS PDE results from the solvability condition (2.24a). This yields that

$$(1,1,1)\frac{\partial}{\partial t}\begin{pmatrix} \frac{1}{k_{\mathrm{bw}}\alpha} \\ \alpha \\ \frac{\alpha}{k_{\mathrm{b}}} + \frac{1}{k_{\mathrm{b}}k_{\mathrm{bw}}\alpha} \end{pmatrix} = (1,1,1)\mathbf{M}\begin{pmatrix} \frac{1}{k_{\mathrm{bw}}\alpha} \\ \alpha \\ \frac{\alpha}{k_{\mathrm{b}}} + \frac{1}{k_{\mathrm{b}}k_{\mathrm{bw}}\alpha} \end{pmatrix}. \tag{2.66}$$

By calculating the various terms in this expression, the following nonlinear QSS PDE is obtained for $\alpha(x,t)$:

$$\frac{\partial}{\partial t}\left(\frac{(k_{\mathrm{b}}+1)(k_{\mathrm{bw}}\alpha^2+1)}{k_{\mathrm{b}}k_{\mathrm{bw}}\alpha}\right) = \frac{\partial}{\partial x}\left(\mathcal{V}(\alpha)\alpha + \mathcal{D}(\alpha)\frac{\partial \alpha}{\partial x}\right), \tag{2.67a}$$

where the "effective transport rate" and the "effective rate of diffusion" are given by

$$\mathcal{V}(\alpha) = v\alpha - \frac{1}{k_{\mathrm{bw}}\alpha}, \qquad \mathcal{D}(\alpha) = D\frac{(k_{\mathrm{bw}}\alpha^2-1)}{k_{\mathrm{b}}k_{\mathrm{bw}}\alpha^2}. \tag{2.67b}$$

From (2.80) of §2.5, the zero-flux boundary conditions for this conservation law are

$$\mathcal{V}\alpha + \mathcal{D}\frac{\partial \alpha}{\partial x} = 0, \qquad \text{at} \quad x = 0, 1, \tag{2.67c}$$

which are exactly zero-flux boundary conditions for the QSS PDE (2.67). From (2.67b) we observe that the advection direction depends on the sign of $\mathcal{V}$. In particular, if $\alpha < 1/(\sqrt{vk_{\mathrm{bw}}})$, the net movement is to the right. By integrating the QSS PDE over the domain, and by using (2.67c), we obtain a conservation law for $y(x,t) = \mathbf{e}^T\mathbf{p}^0[\alpha(x,t)]$, where $\mathbf{p}^0(\alpha)$ is defined in (2.63). For all $t > 0$, we obtain in terms of $\alpha(x,t)$ that

$$\int_0^1 y(x,t)dx = \int_0^1 y(x,0)\,dx\,, \qquad y(x,t) \equiv \frac{(k_{\mathrm{b}}+1)}{k_{\mathrm{b}}k_{\mathrm{bw}}}\frac{(k_{\mathrm{bw}}\alpha^2+1)}{\alpha}\,. \tag{2.68}$$

We remark that on the range $k_{\mathrm{bw}}\alpha^2 - 1 > 0$ for which $\mathbf{p}^0$ is a slow manifold for the dynamics, the QSS PDE (2.67a) is well-posed in that the diffusion coefficient in (2.67a) is positive. In fact by expanding (2.67a), we obtain that (2.67a) is equivalent to the following PDE with a constant diffusivity $D/(k_{\mathrm{b}}+1)$,

$$\frac{\partial \alpha}{\partial t} = \frac{D}{k_{\mathrm{b}}+1}\frac{\partial^2 \alpha}{\partial x^2} + \frac{k_{\mathrm{bw}}k_{\mathrm{b}}}{(k_{\mathrm{b}}+1)(k_{\mathrm{bw}}\alpha^2-1)}\left(\left(v\alpha^2 + \frac{1}{k_{\mathrm{bw}}}\right)\frac{\partial \alpha}{\partial x} + \frac{2D}{\alpha k_{\mathrm{b}}k_{\mathrm{bw}}}\left(\frac{\partial \alpha}{\partial x}\right)^2\right). \tag{2.69}$$

Alongside the transport term involving $\frac{\partial \alpha}{\partial x}$, the source term $\frac{2D}{\alpha k_{\mathrm{b}}k_{\mathrm{bw}}}\left(\frac{\partial \alpha}{\partial x}\right)^2$ describes how

gradients in α can lead to an increase in motor density, especially for low densities (so that $1/\alpha$ is large).

Steady-state solutions to the QSS PDE (2.67) are solutions to the nonlocal problem

$$\frac{d\alpha}{dx} = -\frac{k_{\rm b}}{D}\frac{\left(v k_{\rm bw}\alpha^2 - 1\right)}{k_{\rm bw}\alpha^2 - 1}\alpha\,, \qquad \frac{(k_{\rm b}+1)}{k_{\rm b}k_{\rm bw}}\int_0^1 \frac{(k_{\rm bw}\alpha^2+1)}{\alpha}\,dx = 1\,, \tag{2.70}$$

provided that $k_{\rm bw}\alpha^2 - 1 > 0$ on $0 \le x \le 1$. Here, the total mass has been fixed as $\int_0^1 y(x,0)\,dx = 1$. It is possible to use the numerical shooting method described in Appendix A.2 to solve (2.70) and, further, to numerically identify the region in the $k_{\rm bw}$ versus $k_{\rm b}$ parameter space where $k_{\rm bw}\alpha^2 - 1 > 0$ on $0 < x < 1$. For $D = 0.1$, this region is shown in Figure 2.11(a) and in Figure 2.11(b) for $v = 0.1$ and $v = 0.5$, respectively.

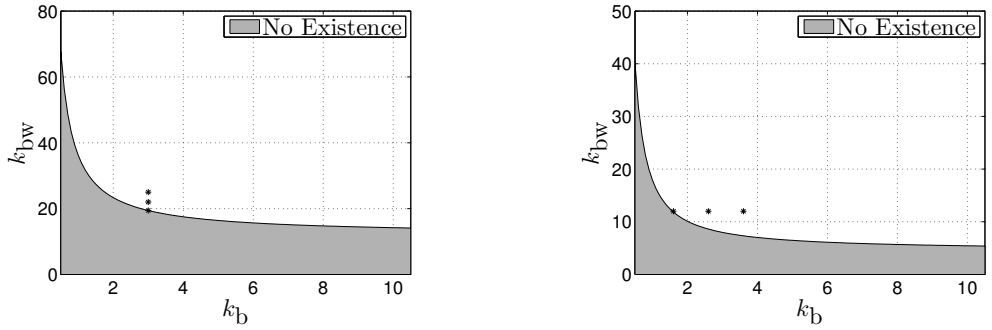

(a) $v = 0.1$ (b) $v = 0.5$

Figure 2.11: Region of solution existence (unshaded). Shown are the regions in the $k_{\rm bw}$ versus $k_{\rm b}$ parameter space where a steady-state to the myosin model Type II QSS PDE (2.67) for $D = 0.1$ exists when (a) $v = 0.1$ and (b) $v = 0.5$. In the shaded regions, there is no steady-state to the Type II QSS PDE. On the boundary of these regions $\alpha = 1/\sqrt{k_{\rm bw}}$ at $x = 0$. The total mass was fixed at $\int_0^1 y(x,0)\,dx = 1$. The points marked in the left and right panel are parameter values corresponding to solutions shown in Figure 2.13 and Figure 2.12, respectively.

Figure 2.12(a)-(c) depicts the QSS motor-densities $p^{\rm B}(x)$, $p^{\rm W}(x)$, and $p^{\rm U}(x)$, for three values of $k_{\rm b}$ corresponding to taking a horizontal slice at fixed $k_{\rm bw} = 12$ through the parameter plane of Figure 2.11(b) with $v = 0.5$. In terms of $\alpha(x)$, these densities are given by (2.63). From Figure 2.12(a)-(b), observe that as $k_{\rm b}$ increases there is an accumulation of bound myosin motors, with a corresponding decrease in walking myosin motors near the left end of the cell. From Figure 2.12(c), observe that as $k_{\rm b}$ increases, there is a decrease in unbound freely diffusing motors in the cytosolic compartment in the middle of the cell.

Figure 2.13(a-c) depicts the QSS motor-densities $p^{\rm B}(x)$, $p^{\rm W}(x)$, and $p^{\rm U}(x)$, for three values of $k_{\rm bw}$ corresponding to taking a vertical slice at fixed $k_{\rm b} = 3.0$ through the phase-

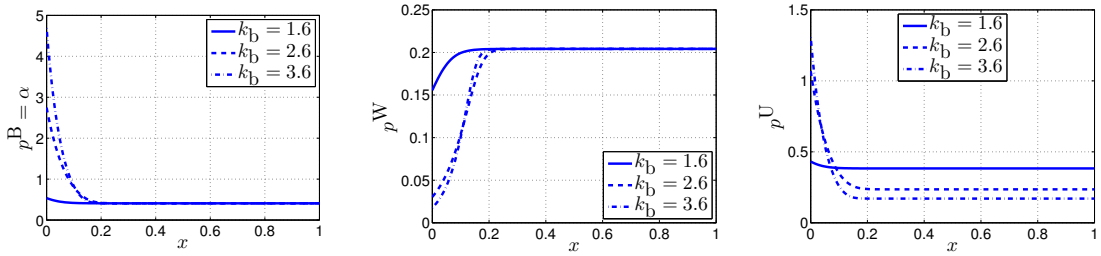

(a) p^{B} versus x (b) p^{W} versus x (c) p^{U} versus x

Figure 2.12: Effect of the (scaled) binding rate, k_{b}. The QSS densities p^{B} (a), p^{W} (b), and p^{U} (c), computed from (2.70) and (2.63), are plotted for three values of k_{b} corresponding to taking a horizontal slice through the parameter space of Figure 2.11(b) with fixed $k_{\mathrm{bw}} = 12$. Other parameters are $D = 0.1$, and $v = 0.5$. The total mass was fixed at $\int_0^1 y(x)\,dx = 1$.

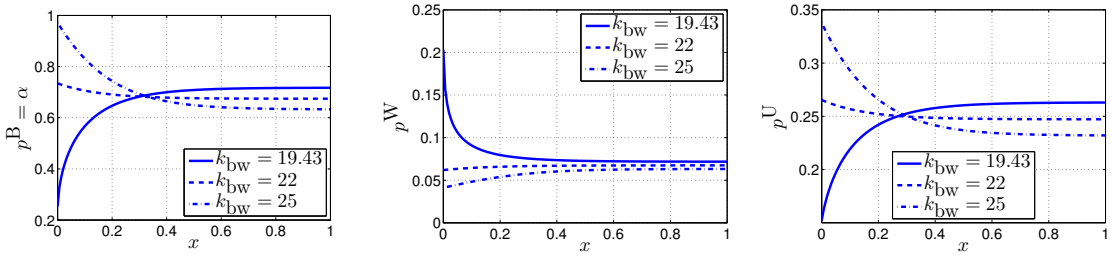

(a) p^{B} versus x (b) p^{W} versus x (c) p^{U} versus x

Figure 2.13: Effect of the (scaled) stalling rate, k_{bw}. As in Figure 2.12 but for three values of k_{bw} corresponding to taking a vertical slice through the parameter space of Figure 2.11(a) with fixed $k_{\mathrm{b}} = 3.0$.

diagram of Figure 2.11(a) with $v = 0.1$. Observe from Figure 2.13(a-b) that as the transition rate k_{bw} between walking to bound motors increases, there is a decrease in walking motors, with a corresponding increase in bound motors near the left end of the cell.

Finally, Figure 2.14(a,b) depicts the QSS motor densities for $v = 0.1$ and $v = 0.5$, respectively, for the parameters $k_{\mathrm{b}} = 3$, $k_{\mathrm{bw}} = 20$, and $D = 0.1$. As the treadmilling speed, v, increases from $v = 0.1$ to $v = 0.5$, note that the system switches from right-biased advection to left-biased advection. This matches the observation that net movement is to the right if $p^{\mathrm{B}} \equiv \alpha < 1/\sqrt{v k_{\mathrm{bw}}}$. For small treadmilling velocity v, this condition is more easily satisfied since the quantity $1/\sqrt{v k_{\mathrm{bw}}}$ is large.

Two notable features distinguish the myosin model from previous models discussed herein. The first is existence of two possible QSS approximations, as shown. A second feature pertains to the boundary-layer behavior near $x = 0$ and $x = 1$. This is analyzed in

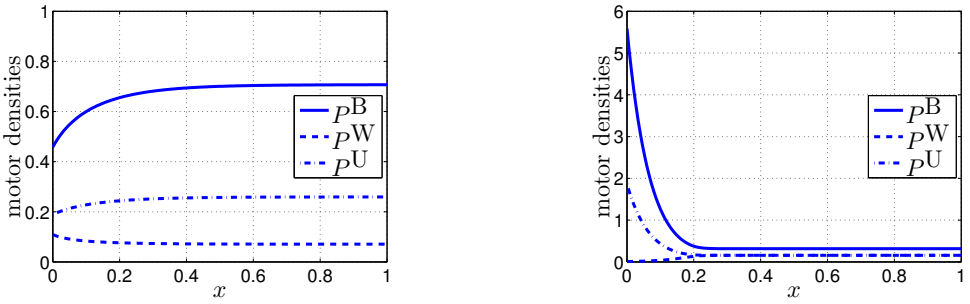

(a) $v = 0.1$ (b) $v = 0.5$

Figure 2.14: Effect of treadmilling speed, v. QSS densities p^B, p^W, and p^U, computed from (2.70) and (2.63), for (a) $v = 0.1$ and (b) $v = 0.5$. As v increases, the system switches from right-biased advection to left-biased advection. Other parameters are $k_{bw} = 20$, $k_b = 3$ and $D = 0.1$. The total mass is $\int_0^1 y(x,0)\,dx = 1$.

detail in §2.5.3 based on the full myosin transport model (A.24) near $x = 0$. There, using phase-plane analysis, I explain that it is always possible to insert a boundary layer near $x = 0$ to satisfy $p^W = 0$ at $x = 0$. However, §2.5.3 also shows that there is no steady-state boundary-layer solution near $x = 1$ that allows the extra boundary condition $p^B = 0$ at $x = 1$ to be satisfied. This difficulty results from the fact that $p^B = 0$ is the slow manifold for the Type I solutions of §2.4.3. Since no steady-state boundary layer solution exists in the full model, any non-zero density of stalled motors p^B will tend to 0 via a backwards propagating wave that leaves $p^B = 0$ in its wake. The full myosin model converges to a Type I QSS (2.57) regardless of the initial condition. An example of this behaviour is shown in Figure 2.15, where $k_{bw} = 25$, $k_b = 3$, $D = 0.1$, $v = 0.5$, and $\varepsilon = 0.02$. As a result, drawing conclusions about the behavior of the full system from the QSS PDE becomes difficult. This leads to the question of which QSS PDE, Type I or Type II, better describes the bulk system dynamics.

One possible regularization to overcome this problem with the boundary-layer near $x = 1$ is to add an asymptotically small diffusion term $\varepsilon_1 p^B_{xx}$ to (A.24), where $\varepsilon_1 = \mathcal{O}(\varepsilon)$. This regularization term does not affect the quasi-steady-states at leading order. The addition of such a small "regularizing" diffusion term also appears in the traveling-wave analysis of [102]. The fully scaled model is as in (A.24c), but with the additional small diffusion term

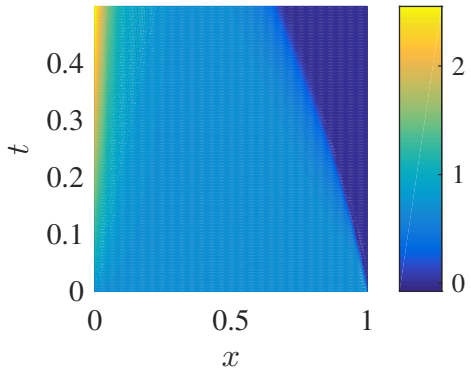

Figure 2.15: $p^{\mathrm{B}}(x,t)$ converges to Type I QSS. The density of bound motors, $p^{\mathrm{B}}(x,t)$, tends to zero behind a wave propagating backwards from $x=1$. The full myosin model converges to a Type I QSS as no non-trivial steady-state solution satisfies the boundary condition $p^{\mathrm{B}}(1)=0$. Parameters are $k_{\mathrm{bw}}=25$, $k_{\mathrm{b}}=3$, $D=0.1$, $v=0.5$, and $\varepsilon=0.02$.

in the p^{B} equation:

$$\frac{\partial p^{\mathrm{W}}}{\partial t} = -\frac{\partial p^{\mathrm{W}}}{\partial x} + \frac{1}{\varepsilon}\left(-k_{\mathrm{bw}}\left(p^{\mathrm{B}}\right)^2 p^{\mathrm{W}} + k_{\mathrm{b}} p^{\mathrm{U}} - p^{\mathrm{W}}\right), \tag{2.71a}$$

$$\frac{\partial p^{\mathrm{B}}}{\partial t} = \varepsilon_1 \frac{\partial^2 p^{\mathrm{B}}}{\partial x^2} + v\frac{\partial p^{\mathrm{B}}}{\partial x} + \frac{1}{\varepsilon}\left(k_{\mathrm{bw}}\left(p^{\mathrm{B}}\right)^2 p^{\mathrm{W}} - p^{\mathrm{B}}\right), \tag{2.71b}$$

$$\frac{\partial p^{\mathrm{U}}}{\partial t} = D\frac{\partial^2 p^{\mathrm{U}}}{\partial x^2} + \frac{1}{\varepsilon}\left(p^{\mathrm{B}} + p^{\mathrm{W}} - k_{\mathrm{b}} p^{\mathrm{U}}\right). \tag{2.71c}$$

The boundary conditions are as before, (2.12) and (2.13), but instead of $p^{\mathrm{B}}(1,t)=0$, it is necessary to impose that

$$\frac{\partial p^{\mathrm{B}}}{\partial x}(0,t) = 0 \quad \text{and} \quad \frac{\partial p^{\mathrm{B}}}{\partial x}(1,t) = 0, \tag{2.72}$$

for conservation of mass.

In this case, both Type I and Type II QSS PDE are valid approximations of the full system, and it is possible to add steady-state boundary layers near $x=0$ and $x=1$ for the regularized model (2.71). However, it is intractable anaytically to analyze the global behavior of time-dependent solutions for (2.71), so as to predict which of the two types of QSS PDEs will result from an an arbitrary initial state. Figure 2.16(a) depicts that the full model (2.71) with asymptotically small diffusion term $\varepsilon_1 p^{\mathrm{B}}_{xx}$ has a steady-state with non-zero p^{B}, and that solutions can converge to the Type II QSS (as compared with Figure 2.15). In this case, as shown in Figure 2.16(b), solutions to the full myosin model and the Type II QSS PDE agree as expected.

Due to the existence of two QSS solutions, it is expected that the initial condition for

(2.71) determines whether the full myosin model converges to the Type I or Type II QSS. To elucidate this hypothesis, I fix the model parameters $k_{\mathrm{bw}} = 25$, $k_{\mathrm{b}} = 3$, $D = 0.1$, $v = 0.5$, $\varepsilon = 0.02$, and $\varepsilon_1 = 0.005$ and numerically determine to which QSS the regularized full system of PDE's (2.71) converges for a range of spatially homogenous initial conditions: $p^{\mathrm{W}}(x,0) = c_1$, $p^{\mathrm{B}}(x,0) = c_2$, with $0 \leq c_2, c_2 \leq 1$, $c_1 + c_2 \leq 1$ and $p^{\mathrm{U}}(x,0) = 1 - c_1 - c_2$ (to ensure conservation of total mass). In Figure 2.17, the results of this exploration are shown in a phase-diagram. For a given pair of spatially homogenous initial conditions, $(p^{\mathrm{B}}(x,0), p^{\mathrm{W}}(x,0))$, a circle indicates that the model (2.71) converges to a Type I QSS, while a cross indicates that the model (2.71) converges to a Type II QSS. The line on the phase-diagram indicates the unstable manifold which emanates from a saddle-point steady-state in the myosin-model reaction kinetics (the non-spatial myosin-model). For a phase-plane analysis of the non-spatial model, see §A.4.4. Below this unstable manifold, the solutions converge to a steady-state with $p^{\mathrm{B}} = 0$, similar to a Type I QSS. Above this unstable manifold, solutions converge to a steady-state with $p^{\mathrm{B}} > 0$, similar to a Type II QSS. The discrepancy between the unstable manifold computed from the non-spatial model and the phase-diagram from the fully-spatial model indicates that the spatial processes enlarge the region of attraction for Type II QSS with non-zero p^{B}.

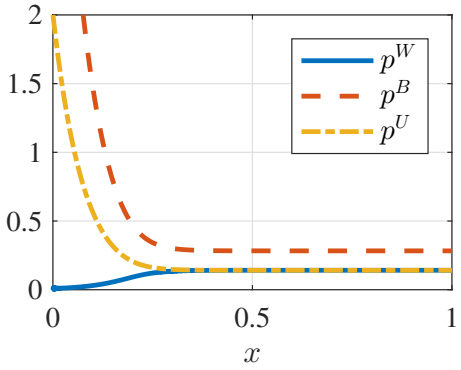

(a) Steady-state myosin densities

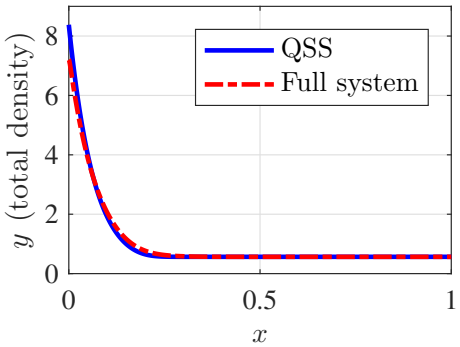

(b) QSS and myosin model comparison

Figure 2.16: Steady-state behaviour of the regularized myosin model. (a) The steady-state behaviour of the full myosin model with small p^{B} diffusion term. Note that $p^{\mathrm{B}} > 0$ for all x. (b) A comparison of the total density of myosin in the Type II QSS approximation and in the full model. Note that this Type II QSS behaviour approximates the full system dynamics well. Parameters are $k_{\mathrm{bw}} = 25$, $k_{\mathrm{b}} = 3$, $D = 0.1$, $v = 0.5$, $\varepsilon = 0.02$, and $\varepsilon_1 = 0.005$. The total mass was fixed at $\int_0^1 y(x)\,dx = 1$.

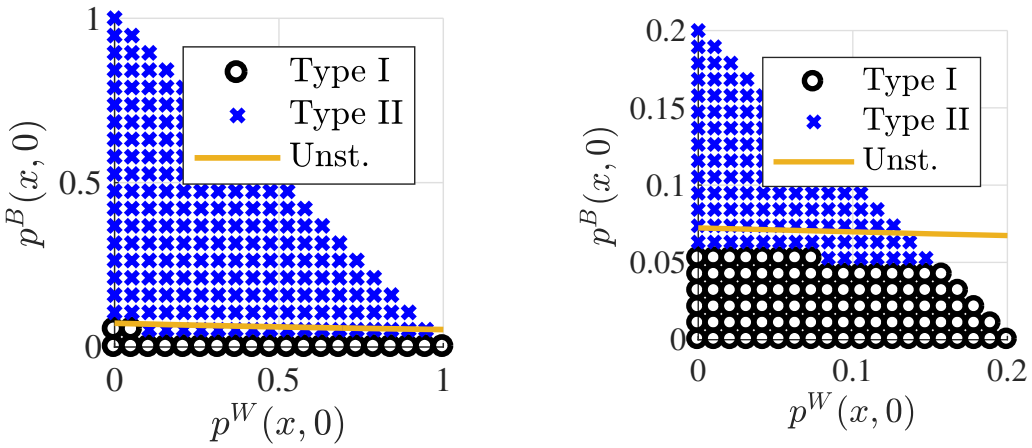

(a) Phase-diagram

(b) Enlarged version of (a)

Figure 2.17: Myosin model initial condition dependence. The steady-state behaviour of the full myosin model with p^{B} diffusion depends on the initial conditions. For a given pair of spatially homogenous initial conditions, $\left(p^{\mathrm{W}}(x,0), p^{\mathrm{B}}(x,0)\right) = (c_1, c_2)$, with $p^{\mathrm{U}}(x,0) = 1 - c_1 - c_2$, the solution will converge to a Type I steady-state, with $\int_0^1 p^{\mathrm{B}}(x)\,dx = 0$ (indicated by a circle), or to a Type II steady-state (cross), with $\int_0^1 p^{\mathrm{B}}(x)\,dx > 0$. The line in the phase-diagram represents the unstable manifold computed from the non-spatial myosin model (§A.4.4). In the non-spatial model, the solution converges to a Type I steady-state ($p^{\mathrm{B}} = 0$) with initial conditions below this unstable manifold, while the solution converges to a Type II steady-state ($p^{\mathrm{B}} > 0$) with initial conditions above this unstable manifold. Parameters are $k_{\mathrm{bw}} = 25$, $k_{\mathrm{b}} = 3$, $D = 0.1$, $v = 0.5$, $\varepsilon = 0.02$, and $\varepsilon_1 = 0.005$. The total mass was fixed at $\int_0^1 y(x)\,dx = 1$.

2.5 Boundary Layer Analysis

In this section, the appropriate boundary conditions for the QSS PDEs are determined, and the boundary layers in the full models near $x = 0, 1$ are analyzed. In particular, I explain how the QSS PDE inherits the boundary condition from the full reaction-advection-diffusion PDE system. Using the method of matched asymptotics, I also analyze the boundary layer behaviour of solutions to the full PDE system to explain estimate the error in the QSS approximation.

The discussion begins with general three-component systems on $0 \le x \le 1$ of the form

$$p_{1t} = -v_1 p_{1x} + \frac{f_1}{\varepsilon}, \qquad p_{2t} = v_2 p_{2x} + \frac{f_2}{\varepsilon}, \qquad p_{3t} = D p_{3xx} + \frac{f_3}{\varepsilon}, \tag{2.73a}$$

where v_1, v_2, D are positive $\mathcal{O}(1)$ constants, $\varepsilon \ll 1$, and the kinetics $f_j = f_j(p_1, p_2, p_3)$ for

$j = 1, 2, 3$, satisfy the conservation condition

$$f_1 + f_2 + f_3 = 0. \tag{2.73b}$$

The three models, kinesin, kinesin-dynein, and myosin are systems of PDE of the form (2.73a). Imposing the mass constraint $\partial_t \int_0^1 (p_1 + p_2 + p_3)\, dx = 0$, and setting $p_1(0,t) = p_2(1,t) = 0$, reveals the following boundary conditions for (2.73a):

$$Dp_{3x} + v_2 p_2 - v_1 p_1 = 0, \quad \text{at} \quad x = 0, 1; \qquad p_1(0,t) = 0, \quad p_2(1,t) = 0. \tag{2.73c}$$

Matched asymptotic analysis

As in the QSS reduction in the previous sections, assume that there is a unique one-parameter family $\mathbf{p}^0(\alpha) \equiv (p_1^0(\alpha), p_2^0(\alpha), p_3^0(\alpha))^T$ of solutions to the leading-order problem $\mathbf{f} = (f_1, f_2, f_3)^T = \mathbf{0}$, and that $\mathbf{p}^0$ is a slow manifold for (2.73) in the sense of Definition 2.3.1. Then, as was shown in §2.3, $\alpha = \alpha(x,t)$ satisfies the QSS PDE (2.24a), which can be written as

$$\partial_t \left(p_1^0 + p_2^0 + p_3^0\right) = \partial_x \left(-v_1 p_1^0 + v_2 p_2^0 + D\partial_x p_3^0\right). \tag{2.74}$$

The QSS solution is known as the *outer solution*, which is valid away from the boundaries $x = 0, 1$.

To determine an appropriate boundary condition for (2.74) as $x \to 0^+$, I analyze the boundary layer structure for (2.73) near the left endpoint $x = 0$. As $x \to 0^+$, then it is expected that the solution to the full system will agree with the outer solution (from the QSS PDE) with errors that depend on x:

$$p_1 = p_{10}^0 + \mathcal{O}(x), \qquad p_2 = p_{20}^0 + \mathcal{O}(x), \qquad p_3 \to p_{30}^0 + x \frac{dp_3^0}{dx}\Big|_{x=0} + \cdots, \tag{2.75}$$

where $p_{j0}^0 \equiv p_j^0(\alpha(0,t))$ denotes the QSS solution evaluated at $x = 0$. for $j = 1, 2, 3$. Since the cell-ends are interchangeable, only an analysis of the boundary layer near $x = 0$ is presented—a similar analysis can be done near $x = 1$.

To determine the width of the boundary layer, consider the dominant balances in the full system. For $t = \mathcal{O}(1)$ the two possible balances for the spatial derivatives in (2.73a) near $x = 0$ are $x = \mathcal{O}(\sqrt{\varepsilon})$ and $x = \mathcal{O}(\varepsilon)$ (considering the presence of a first-order and a second-order spatial dertivatives and the $\frac{1}{\varepsilon}$ multiplying the nonlinear function f). On the

wider scale, use the change of variables $\xi = x/\sqrt{\varepsilon}$ to obtain from (2.73a) that

$$p_{1t} = -\frac{v_1}{\sqrt{\varepsilon}} p_{1\xi} + \frac{f_1}{\varepsilon}, \qquad p_{2t} = \frac{v_2}{\sqrt{\varepsilon}} p_{2\xi} + \frac{f_2}{\varepsilon}, \qquad p_{3t} = \frac{D}{\varepsilon} p_{3\xi\xi} + \frac{f_3}{\varepsilon}. \tag{2.76}$$

In this case, for $\varepsilon \ll 1$, the leading-order contributions are from those terms with factor $\frac{1}{\varepsilon}$. At leading order, $f_1 = f_2 = 0$ (from the first two equations in (2.76)). This implies that $f_3 = 0$ thanks to conservation (2.73b). Since the QSS solution satisfies $f_1 = f_2 = f_3 = 0$, it follows that on this wide-scale that $p_1 \sim p_{10}^0$, $p_2 \sim p_{20}^0$, and $p_3 \sim p_{30}^0$ for $x = \mathcal{O}(\sqrt{\varepsilon})$. In other words, the QSS approximation is still valid on this wide-scale when $x = \mathcal{O}(\sqrt{\varepsilon})$.

The other dominant balance for spatial derivatives in (2.73a) is $x = \mathcal{O}(\varepsilon)$. To study this region, introduce $\eta \equiv x/\varepsilon$, and obtain from (2.73a) that

$$\varepsilon p_{1t} = -v_1 p_{1\eta} + f_1, \qquad \varepsilon p_{2t} = v_2 p_{2\eta} + f_2, \qquad \varepsilon p_{3t} = \frac{D}{\varepsilon} p_{3\eta\eta} + f_3. \tag{2.77a}$$

From (2.73c), the boundary conditions for this system are

$$\frac{D}{\varepsilon} p_{3\eta} + v_2 p_2 - v_1 p_1 = 0, \quad \text{at} \quad \eta = 0; \qquad p_1(0,t) = 0, \tag{2.77b}$$

while the asymptotic matching conditions, as obtained from (2.75), are that

$$p_1 \sim p_{10}^0, \qquad p_2 \sim p_{20}^0, \qquad p_3 \sim p_{30}^0 + \varepsilon\eta \frac{dp_3^0}{dx}\Big|_{x=0}, \qquad \text{as} \quad \eta \to \infty. \tag{2.77c}$$

For $t = \mathcal{O}(1)$, neglect the asymptotically negligible left-hand sides of (2.77a) to obtain

$$-v_1 p_{1\eta} = -f_1, \qquad v_2 p_{2\eta} = -f_2, \qquad \frac{D}{\varepsilon} p_{3\eta\eta} = -f_3. \tag{2.78}$$

By adding the equations in (2.78), using the conservation condition (2.73b), and after integrating in η, for all $\eta > 0$,

$$\frac{D}{\varepsilon} p_{3\eta} - v_1 p_1 + v_2 p_2 = A, \tag{2.79}$$

where A is independent of η. Evaluating this expression at $\eta = 0$, (2.77b) yields that $A = 0$. With $A = 0$, evaluating (2.79) as $\eta \to \infty$ by using the matching condition (2.77c) yields

$$D\frac{dp_3^0}{dx} - v_1 p_1^0 + v_2 p_2^0 = 0, \quad \text{at} \quad x = 0. \tag{2.80a}$$

This key result shows that to obtain the boundary condition at $x = 0$ for the QSS PDE for $\alpha(x,t)$, it is possible to substitute the outer approximation $p_1 = p_1^0(\alpha)$, $p_2 = p_2^0(\alpha)$, and

$p_3 = p_3^0(\alpha)$, into the first condition of (2.73c). In this sense, the QSS PDE inherits the no-flux boundary condition (2.73c) at $x = 0$. Note that a similar analysis can be done near $x = 1$, with the analogous result that

$$D\frac{dp_3^0}{dx} - v_1 p_1^0 + v_2 p_2^0 = 0, \quad \text{at} \quad x = 1. \tag{2.80b}$$

Next, to fully characterize the beahviour of the boundary layer and to estimate the error made with the QSS approximation, I complete the boundary layer analysis near $x = 0$ by asymptotically expanding:

$$p_3 = p_{30}^0 + \frac{\varepsilon}{D}\mathcal{P}_3 + \cdots, \tag{2.81}$$

and obtain from the first two equations in (2.78), together with (2.79) with $A = 0$, the following boundary-layer problem on $0 < \eta < \infty$:

$$v_1 p_{1\eta} = f_1\left(p_1, p_2, p_{30}^0\right); \qquad p_1(0) = 0, \quad p_1 \to p_{10}^0 \quad \text{as} \quad \eta \to \infty, \tag{2.82a}$$

$$v_2 p_{1\eta} = -f_2\left(p_1, p_2, p_{30}^0\right); \qquad p_2 \to p_{20}^0 \quad \text{as} \quad \eta \to \infty, \tag{2.82b}$$

$$\mathcal{P}_{3\eta} = v_1 p_1 - v_2 p_2; \qquad \mathcal{P}_{3\eta} \sim D\frac{dp_3^0}{dx}\Big|_{x=0} \quad \text{as} \quad \eta \to \infty. \tag{2.82c}$$

Here, the first two equations result from the dynamics of the full model in the region where $x = \mathcal{O}(\varepsilon)$, i.e., with spatial coordinate η. Boundary conditions for these equations result from the fact that $p_1(0) = 0$, and that both p_1 and p_2 should match with the outer solution (from the QSS) as $\eta \to \infty$. Finally, the boundary conditions at $x = 0$ (2.79) imply that the correction term $\mathcal{P}_3$ must satisfy the $\mathcal{P}_{3\eta} = v_1 p_1 - v_2 p_2$, with the derivative matching the derivative of the outer solution as $\eta \to \infty$.

Although the first two equations for p_1 and p_2 are uncoupled from $\mathcal{P}_3$, in general it is not possible to calculate p_1 and p_2 analytically when f_1 and f_2 are nonlinear in p_1 and p_2. However, the system for p_1 and p_2 can be readily studied qualitatively in the phase-plane.

A similar boundary layer analysis can be done near $x = 1$. To study this boundary layer, define $\eta = (1 - x)/\varepsilon$ to find, in place of (2.82a) and (2.82b), that

$$v_1 p_{1\eta} = -f_1\left(p_1, p_2, p_{31}^0\right); \qquad p_1 \to p_{11}^0 \quad \text{as} \quad \eta \to \infty, \tag{2.83a}$$

$$v_2 p_{1\eta} = f_2\left(p_1, p_2, p_{31}^0\right); \qquad p_2(0) = 0, \qquad p_2 \to p_{21}^0 \quad \text{as} \quad \eta \to \infty. \tag{2.83b}$$

Here $p_{j1}^0 \equiv p_j^0(\alpha(1,t))$, for $j = 1, 2, 3$.

Next, I will study the phase-plane behaviour of the boundary layer solution for the kinesin, kinesin-dynein, and the myosin models.

2.5.1 The Kinesin Model

For the kinesin model (2.25) of §2.4.1, the boundary layer system (2.82) can be solved explicitly. With the QSS approximation $\mathbf{p}^0$, as given in (2.27), note that $v_1 = v_2 = 1$, $p_1 = p^{\mathrm{R}}$, $p_2 = p^{\mathrm{L}}$, and $p_3 = p^{\mathrm{U}}$. From the QSS for the kinesin model, (2.27), the outer solution gives $p_{10}^0 = k_{\mathrm{a}} P(0) g(\alpha_0)$, $p_{20}^0 = k_{\mathrm{a}} [1 - P(0)] g(\alpha_0)$, and $p_{30}^0 = \alpha_0$, where $\alpha_0 \equiv \alpha(0,t)$. Therefore, using the reaction kinetics in (2.25), the boundary layer problem (2.82) becomes

$$p_{1\eta} = p_{10}^0 - p_1, \qquad p_{2\eta} = -p_{20}^0 + p_2, \qquad \mathcal{P}_{3\eta} = p_1 - p_2. \tag{2.84}$$

The solution with $p_1(0) = 0$, $p_1 \to p_{10}^0$ and $p_2 \to p_{20}^0$ as $\eta \to \infty$, is simply $p_1 = p_{10}^0(1 - e^{-\eta})$, and $p_2 = p_{20}^0$. Then, $\mathcal{P}_3$ is obtained up to a constant by integrating the last equation in (2.84). In this way, the boundary layer solution for $x = \mathcal{O}(\varepsilon)$ is that

$$p^{\mathrm{R}} \sim p_{10}^0 \left(1 - e^{-x/\varepsilon}\right), \qquad p^{\mathrm{L}} \sim p_{20}^0, \qquad p^{\mathrm{U}} = p_{30}^0 + \frac{\varepsilon}{D}\left(\eta D \frac{d\alpha}{dx}|_{x=0} + p_{10}^0 e^{-\eta} + B\right), \tag{2.85}$$

where the constant B can only be determined from a two-term outer QSS solution, that is intractable analytically. This analysis shows two key features. First, the right-moving motors have a classic boundary-layer behaviour when $x = \mathcal{O}(\varepsilon)$. Second, for $x = \mathcal{O}(\varepsilon)$ the unbound kinesin motor density p^{U} differs from its outer approximation only by an error $\mathcal{O}(\varepsilon/D)$. A similar calculation can be done for the boundary layer near $x = 1$ using (2.83).

2.5.2 The Kinesin-Dynein Model

For the kinesin-dynein model (2.48), I study the boundary-layers equations (2.82) for the layer near $x = 0$ qualitatively in the phase-plane. Using $\mathbf{f}$ in (2.48), and setting $v_1 = 1$ and $v_2 = v$, (2.82a) and (2.82b) on $0 < \eta < \infty$ become

$$p_{1\eta} = -p_1 - k p_1 p_2 + k_{\mathrm{a}} Q p_{30}^0, \qquad p_1(0) = 0, \qquad p_1 \to p_{10}^0 \equiv \frac{Q\alpha_0}{k\alpha_0 + 1 - Q} \quad \text{as} \quad \eta \to \infty, \tag{2.86a}$$

$$p_{2\eta} = -\frac{1}{v}\left[k_{\mathrm{a}}(1 - Q) p_{30}^0 - p_2 + k p_1 p_2\right], \qquad p_2 \to \alpha_0 \qquad \text{as} \quad \eta \to \infty, \tag{2.86b}$$

where $p_{30}^0 = (k\alpha_0 + 1)\alpha_0/[k_a(k\alpha_0 + 1 - Q)]$. To analyze (2.86) in the phase-plane, it is convenient to introduce new variables $q_1(\eta)$ and $q_2(\eta)$ defined by

$$p_1 = \frac{r_2}{k} q_1, \qquad p_2 = \frac{r_1}{k} q_2, \qquad \text{where} \qquad r_1 = k\alpha_0, \qquad r_2 \equiv \frac{Q r_1}{r_1 + 1 - Q}. \tag{2.87}$$

In terms of q_1 and q_2, (2.86) transforms to the two-component dynamical system

$$q_{1\eta} = g_1(q_1, q_2) \equiv (1 - q_1) + r_1(1 - q_1 q_2), \qquad q_1(0) = 0, \qquad q_1 \to 1 \quad \text{as} \quad \eta \to \infty, \tag{2.88a}$$

$$q_{2\eta} = g_2(q_1, q_2) \equiv -\frac{1}{v}\left[1 - q_2 + r_2(q_1 q_2 - 1)\right], \qquad q_2 \to 1 \qquad \text{as} \quad \eta \to \infty. \tag{2.88b}$$

This system for q_1 and q_2 is more easily studied qualitatively, as it has a equilibrium solution at $q_1 = q_2 = 1$, and the asymptotic matching conditions require that q_1 and q_2 tend 1 as $\eta \to \infty$, to match with the outer solution. Moreover, the initial condition requires that $q_1(0) = 0$. As such, in the phase-plane, I seek to show the existence of a trajectory from the q_2 axis for $\eta = 0$ that converges to $q_1 = q_2 = 1$. Below, I will argue that the equilbrium $(1, 1)$ is a saddle point for the dynamics and demonstrate that such a trajectory does exist. This trajectory will correspond to the boundary layer solution after changing coordinates back to p_1 and p_2.

Note that r_2 depends on r_1. With r_2 considered as a function of r_1: $r_2 = 0$ when $r_1 = 0$; $r_2 \to Q < 1$ as $r_1 \to \infty$; and r_2 is monotone increasing in r_1 since $dr_2/dr_1 = [Q(1 - Q)]/(r_1 + 1 - Q)^2 > 0$ holds for $0 < Q < 1$. It follows that $0 < r_2 < 1$ for any $r_1 > 0$.

The determininant of the Jacobian J_g of g_1 and g_2 at the equilibrium state $q_1 = q_2 = 1$ is

$$\det(J_g) = -\frac{1}{v\,(k\alpha_0 + 1 - Q)}\left[(1 - Q)(1 + 2k\alpha_0) + k\alpha_0^2\right] < 0,$$

revealing that $q_1 = q_2 = 1$ is a saddle point for the dynamics. In Figure 2.18(a), I plot the phase portrait q_2 versus q_1 and nullclines for (2.88) for representative values $r_1 = 2$, $r_2 = 0.5$, and $v = 0.5$. The q_2 nullcline intersects the q_2 axis at $q_2 = 1 - r_2 \in (0, 1)$ since $0 < r_2 < 1$. This plot indicates the existence of a unique value $q_2(0) = q_2^0 > 1 - r_2$ for which (2.88) has a solution with $(q_1, q_2) \to (1, 1)$ as $\eta \to \infty$. This solution corresponds to the stable manifold of the saddle point, which intesects the q_2-axis so that $q_1(0) = 0$. The solution is the boundary-layer solution after returning to the original variables p_1 and p_2. This qualitative analysis confirms the existence of a boundary-layer solution near $x = 0$ for the kinesin-dynein model for a range of parameters.

A similar phase-plane analysis can be done to analyze the boundary-layer system (2.83)

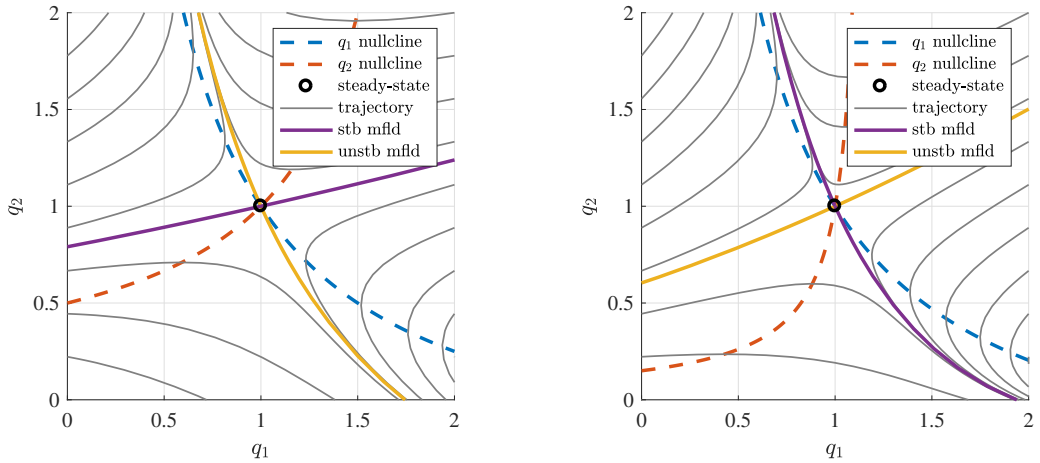

(a) $r_1 = 2.0$, $r_2 = 0.5$, $v = 0.5$ (b) $r_1 = 1.69$, $r_2 = 0.85$, $v = 0.5$

Figure 2.18: Qualitative analysis of boundary layer behaviour of the kinesin-dynein model. Phase portraits of q_2 versus q_1 for boundary layer solutions of the kinesin-dynein model near $x = 0$ (a) and near $x = 1$ (b) from (2.88) and (2.89), respectively. In (a) there is a unique value $q_2 = q_2^0$ at $q_1 = 0$ for which (2.88) has a solution with $(q_1, q_2) \to (1, 1)$ as $\eta \to +\infty$. In (b) there is a unique value $q_1 = q_1^0$ at $q_2 = 0$ for which (2.89) has a solution with $(q_1, q_2) \to (1, 1)$ as $\eta \to \infty$. The parameter values r_1, r_2, and v for (b) are those consistent with Figure 2.8.

near $x = 1$. In place of (2.88), the boundary-layer system is now

$$q_{1\eta} = -g_1(q_1, q_2) \equiv -\left[(1 - q_1) + r_1(1 - q_1 q_2)\right], \qquad q_1 \to 1 \quad \text{as} \quad \eta \to \infty, \tag{2.89a}$$

$$q_{2\eta} = -g_2(q_1, q_2) \equiv \frac{1}{v}\left[1 - q_2 + r_2(q_1 q_2 - 1)\right], \qquad q_2(0) = 0 \qquad q_2 \to 1 \qquad \text{as} \quad \eta \to \infty, \tag{2.89b}$$

where, in place of (2.87), r_1 and r_2 are now defined by $r_1 = k\alpha_1$ and $r_2 \equiv Qr_1/(r_1 + 1 - Q)$, and $\alpha_1 = \alpha$ at $x = 1$. Also note that the asymptotic matching conditions for $\eta \to \infty$ are different. Here, the solution must satisfy $q_2(0) = 0$. As such, I seek a solution that intersects the q_1 axis and converges to $(1, 1)$. Figure 2.18(b) depicts the phase portrait and nullclines for (2.89) for $r_1 = 1.69$, $r_2 = 0.85$, and $v = 0.5$. This corresponds to the parameter values used in Figure 2.8. The phase portrait shows the existence of a unique value $q_1(0) = q_1^0$ for which (2.89) has a solution with $(q_1, q_2) \to (1, 1)$ as $\eta \to \infty$. As before, the solution corresponds to the stable manifold of the saddle point, and yields $q_1^0 \approx 1.95$. In terms of the original variables this yields $p_1 \approx 0.83$ at $x = 1$ (from (2.87)), which agrees with the numerical approximations in Figure 2.8.

2.5.3 The Myosin Model

For the full myosin transport model (A.24), the boundary-layer equations (2.82a)–(2.82b) can be studied qualitatively. In this section, I will explain that a boundary layer solution exists near $x = 0$, however, there is no boundary-layer solution for the myosin model near $x = 1$. This result will explain why the Type II QSS is not realized by numerical solutions to the full myosin model as in §2.4.

The boundary-layer near $x = 0$ can also be studied qualitatively in the phase-plane. Upon setting $v_1 = 1$ and $v_2 = v$, (2.82a) and (2.82b) on $0 < \eta < \infty$ become

$$p_{1\eta} = -k_{\rm bw} p_1 p_2^2 - p_1 + k_{\rm b} p_{30}^0, \qquad p_1(0) = 0, \qquad p_1 \to p_{10}^0 \equiv \frac{1}{k_{\rm bw}\alpha_0}, \quad \text{as} \quad \eta \to \infty, \tag{2.90a}$$

$$p_{2\eta} = -\frac{1}{v}\left(k_{\rm bw} p_1 p_2^2 - p_2\right), \qquad p_2 \to \alpha_0 \qquad \text{as} \quad \eta \to \infty, \tag{2.90b}$$

where $p_{30}^0 = \left(\alpha_0 + 1/[k_{\rm bw}\alpha_0]\right)/k_{\rm b}$ and $\alpha_0 = \alpha(0,t)$. As before, introduce new variables q_1 and q_2 defined by

$$p_1 = \frac{1}{k_{\rm bw}\alpha_0} q_1, \qquad p_2 = \alpha_0 q_2, \tag{2.91}$$

so that in terms of $r \equiv k_{\rm bw}\alpha_0^2$, (2.90) becomes

$$q_{1\eta} = g_1(q_1, q_2) \equiv -r\left(q_1 q_2^2 - 1\right) + 1 - q_1, \qquad q_1(0) = 0, \qquad q_1 \to 1 \quad \text{as} \quad \eta \to \infty, \tag{2.92a}$$

$$q_{2\eta} = g_2(q_1, q_2) \equiv -\frac{1}{v}\left(q_1 q_2^2 - q_2\right), \qquad q_2 \to 1 \qquad \text{as} \quad \eta \to \infty. \tag{2.92b}$$

As in the last section, the equilibrium is a saddle point and the boundary layer solution corresponds to the stable manifold of the saddle point. At the equilibrium state $q_1 = q_2 = 1$, the determinant of the Jacobian J_g of g_1 and g_2 is $\det(J_g) = (1 - r)/v$. Therefore, $\det(J_g) < 0$ and $q_1 = q_2 = 1$ is a saddle-point if $r \equiv k_{\rm bw}\alpha_0^2 > 1$. Figure 2.19(a) depicts phase portrait of q_2 versus q_1 and nullclines for (2.92) for the representative values $r = 5$ and $v = 0.5$. Observe that there is a unique value $q_2(0) = q_2^0$ for which (2.92) has a solution with $(q_1, q_2) \to (1, 1)$ as $\eta \to \infty$. As such, there is always a boundary-layer solution near $x = 0$ for the myosin model.

A similar boundary-layer system near $x = 1$ can be obtained from (2.83) for the myosin

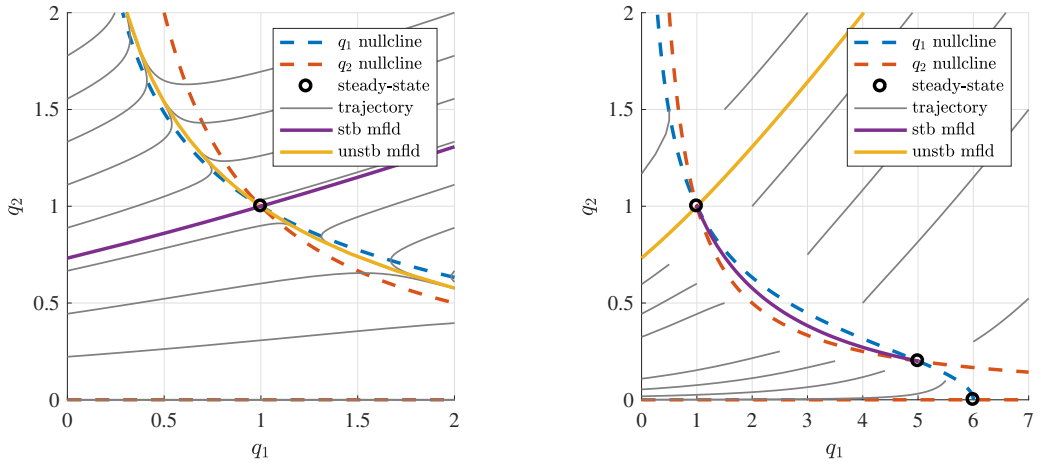

(a) $r = 5$, $v = 0.5$ (b) $r = 5$, $v = 0.5$

Figure 2.19: Qualitative analysis of boundary layer behaviour of the myosin model. Phase portraits of q_2 versus q_1 for boundary layer solutions of the myosin model near $x = 0$ (a) and near $x = 1$ (b) from (2.92) and (2.93), respectively. In (a) there is a unique value $q_2 = q_2^0$ at $q_1 = 0$ for which (2.92) has a solution with $(q_1, q_2) \to (1, 1)$ as $\eta \to +\infty$. However, for the right boundary-layer, the phase-plane in (b) there is no value $q_1 = q_1^0 > 0$ at $q_2 = 0$ for which $(q_1, q_2) \to (1, 1)$ as $\eta \to \infty$.

model. In place of (2.92), the system is

$$q_{1\eta} = -g_1(q_1, q_2) \equiv r\left(q_1 q_2^2 - 1\right) - 1 + q_1, \qquad q_1 \to 1 \quad \text{as} \quad \eta \to \infty, \tag{2.93a}$$

$$q_{2\eta} = -g_2(q_1, q_2) \equiv \frac{1}{v}\left(q_1 q_2^2 - q_2\right), \qquad q_2(0) = 0 \qquad q_2 \to 1 \qquad \text{as} \quad \eta \to \infty, \tag{2.93b}$$

where r is now defined by $r = k_{\text{bw}}\alpha_1^2$ with $\alpha_1 = \alpha(1, t)$. Although the equilibrium point $q_1 = q_2 = 1$ is a saddle point of (2.93) whenever $r > 1$, the phase portrait in the q_2 versus q_1 plane in Figure 2.19(b) shows that there is no value $q_1(0) = q_1^0 > 0$ on $q_2 = 0$ for which $(q_1, q_2) \to (1, 1)$ as $\eta \to \infty$.

As such, for the Type II QSS approximation (2.63) in the myosin model there is no steady-state boundary-layer solution near $x = 1$ that allows the extra boundary condition $p^{\text{B}} = 0$ at $x = 1$ to be satisfied.

2.6 Discussion

The quasi-steady-state reduction method for molecular motor transport was introduced in [57] for reaction–advection–diffusion systems with linear reaction kinetics. Here, I have generalized this method to a class of problems where the kinetics are nonlinear, but where a conservation condition is satisfied. The QSS method relies on the assumption that the

nonlinear kinetics occur on a faster time-scale than the diffusion and advection processes. In this limit of fast reaction kinetics, and under a condition on the eigenvalues of the Jacobian of the kinetics, the full system dynamics were shown to be well-approximated by the dynamics on a slow solution manifold, which consists of a single scalar quasi-steady-state PDE. This asymptotic formalism was used to analyze three specific nonlinear models for the binding and unbinding of molecular motors.

Three models I used as case-studies contained two distinct types of nonlinear reaction. (1) The kinesin model has a nonlinearity in the binding rate of motors to MT (due to saturation, with and without binding cooperativity). This model reduces (with parameter $c = 0$) to the linear binding case considered in a previous study [16], and is used here as a basic "control" to validate our method. Typical nonlinear responses such as Michaelis-Menten or Hill function kinetics were used to describe the dependence of binding rate on the free motor density (represented by the increasing and saturating function g). Here the nonlinearity was a function of a single state-variable. (2) In the second class of models, nonlinearity stemmed from interaction between motors in different states, such as collisions that lead to direction changes or stalling while bound to a MT. Both the kinesin-dynein complex model and the myosin motor model shared such aspects.

Each model satisfied a conservation law, namely the total density of motors was fixed in the cell (the total density was fixed at 1 for numerics throughout, as discussed in Appendix A.4). This constraint served an important purpose, as it was used to reduce the system from n to $n - 1$ states (where $n = 3$ for all our models). In each case, the population of motors in various states was defined in terms of one reference state (denoted by $\alpha(x)$). The choice for that reference state was merely a matter of convenience of calculations, and specific to each case.

Many elements of the linear QSS theory carry over to the nonlinear analysis here. However, the geometry of projections in the linear case (as developed in [7, 57]) no longer holds, suggesting that obtaining higher order terms in asymptotic solutions is no longer tractable. Obtaining expressions for such correction terms remains an open problem. Moreover, in many cases, the diffusion coefficient in the unbound state is taken to be $\mathcal{O}(\varepsilon)$. If this is the case, in those particular cases where the drift term vanishes, our QSS PDE would simply reduce to a conservation law for the total density of motors, and fail to describe the dynamics of the system. To avoid this, it is necessary to assume that the diffusion coefficient in the unbound state is $\mathcal{O}(1)$.

For all such models, the QSS reduction of (2.15) leads to new scalar nonlinear PDEs, are not easily amenable to analytical solution techniques. Although it was still necessary to solve these QSS PDEs numerically, the QSS reduction does effectively eliminate the small parameter ε from the full model and avoids the more challenging numerical task of having

to compute solutions to the full nonlinear vector system (2.15) of PDEs at each small ε.

The QSS analysis permits the formulation of conclusions about the overall rate of transport (advection velocity) of the system that results from the combination of motors walking on MT, diffusing while unbound, and kinetics of binding, unbinding, switching directions, and/or stalling. Additionally, the QSS PDE was shown to provide insight into the behaviour of the steady-state solutions as parameters are varied. This insight was used to interpret cell-level behaviours resulting from various specific molecular-motor-level assumptions. I now summarize some of the major conclusions and their implications for each of the case-studies.

Kinesin model

Here the cytosolic motor state was used as the reference state α, and a Fokker-Planck (FP) equation (2.29) was derived for the total motor density. In the special case of spatially constant microtubule bias, this reduced further to the FP equation (2.33a) for the cytosolic state from which we can draw several conclusions. (a) The overall transport direction depends on the sign of $(1-2P)$. (b) When $(1-2P) \neq 0$ (which means that more MTs point to one end of the cell than to the other), I predict an exponential spatial motor distribution corresponding to MTs bias. (c) Both the effective diffusion and the effective transport rates are (essentially) averages of the diffusion and transport rates in the underlying states, weighted by the fraction of time spent in each of those states. These conclusions are consistent with results of the linear models in [16]. (d) When MT polarity bias $P(x)$ is spatially nonuniform, there arises the possibility for motors to pile up either at cell ends or in the middle of the cell, as shown in Figure 2.6. This reflects the earlier results for the QSS reduction of a model with spatially varying parameters. In this case, the resulting QSS PDE had spatially dependent effective diffusion and velocity [58]. (e) The overall effect of nonlinear binding in this case is that more kinesin motors are sequestered in the freely diffusing class, which results in a shallower motor density across the cell. The shallower solution profile results from the fact that the binding rate is limited in both the saturated binding and Hill function binding cases. (f) Hill function binding (which could represent cooperative motor binding interactions) creates 'kinks' and inflection points in the spatial motor distribution, since the Hill function turns binding on or off more sharply than does Michaelis-Menten kinetics.

Kinesin-Dynein model

Here the nonlinearity involves a product of two state variables (left and right moving complexes), a composite left-right bias function $Q(x)$, and possibly distinct velocities when moving right or left (see Appendix A.3.2 for the relationship of the function Q to the un-

derlying biological details). Here the left-moving motor variable was used as reference state α. Both the effective transport rate and effective diffusion rate are "density dependent" functions of α. The effective transport rate depends intuitively on the model parameters. Increasing the velocity of left-moving complexes, decreasing the probability of binding to the right-moving state, or increasing the right-to-left turning rate all result in biasing transport towards the left-end of the cell. The effective diffusion rate is scaled by $1/k_{\mathrm{a}}$ (k_{a} is the association constant), which intuitively modulates how many molecular motor complexes remain in the cytosolic vs. bound states. The effective diffusion rate is further increased from baseline through the "tug-of-war" that the motor complex exerts on its cargo. This increase results from the product $(1-Q)Q$, which gives the probability of binding into the left-moving and right-moving state. Although a motor cannot simultaneously bind into the left-moving and right-moving state, I find that the competition between right-moving and left-moving states increases the effective diffusion of the system—this makes sense, as any rapid switching between right- and left-moving states is similar to a diffusive mechanism.

Myosin model

The motor interference was assumed to cause stalling with a higher-degree nonlinearity ($(p^{\mathrm{B}})^2 p^{\mathrm{W}}$) than in the kinesin-dynein motor complex model, which was inspired by the nonlinear interactions in a model for myosin aggregations [101, 102]. Moreover, the stalled and walking myosin motors have different velocities, with the stalled motors being transported due to actin treadmilling. Interestingly, this higher-degree nonlinearity gave rise to two distinct QSS solutions, one of which was characterized by the absence of stalled motors ($p^B = 0$, "Type I QSS"). In this case, the QSS PDE is linear and the steady-state solution was found explicitly. For the second QSS solution with $p^B \neq 0$, I identified a nonlinear FP equation with diffusivity $D/(1+k_{\mathrm{b}})$, a density-dependent effective transport term, and an additional term proportional to $(\partial\alpha/\partial x)^2$. The latter ("Type II QSS") exists only for a subset of parameters (Figure 2.11). Moreover, solutions to the full system converge to the Type I solution, unless the full model is corrected by an asymptotically small diffusion term for the stalled motors. Interestingly, such a term had been included in the model in [101, 102]. There, the inclusion of this small diffusion term was justified physically as a small random motion of stalled motors, yet the analysis here reveals a mathematical justification. This peculiar effect stems from an issue with the boundary layer at the cell end $x = 1$. The small diffusive correction term changes the p^{B} equation from hyperbolic to parabolic, allowing the model to be consistent with boundary conditions that the uncorrected model cannot satisfy. In this case, the existence of two QSS solutions suggested further investigation of the behaviour of the full myosin model. Through extensive numerical simulations, it was possible to determine which QSS PDE would better describe the dynamics of the full

system (Figure 2.17). In the end, a phase-plane analysis of the non-spatial kinetic model largely suggested which QSS PDE would be valid for a given set of spatially homogenous initial conditions.

All in all, the QSS analysis is generalizable to nonlinear models for molecular motors. That said, the examples discussed herein are simplified prototypes and caricatures of actual molecular motor behaviour. For example, a caveat of the kinesin model (2.3) is that the nonlinear binding function, $g(p^{\mathrm{U}})$, may not accurately describe biological effects such as competition for binding sites on a single MT. As formulated with a saturating function for $g(p^{\mathrm{U}})$, the model implies that crowding in a region of the cell is responsible for limiting the binding rate of motors to MTs, rather than explicit competition for binding sites. In the kinesin model, it is necessary to interpret the saturated binding rate as a result of competition or crowding for binding sites on a single MT.

In reality, many more states and interactions between states could occur, making the biological system more realistic and interesting, but also much more complicated to analyze mathematically. In this analysis, I have not considered the cases of heterogenous multi-motor complexes composed of a distribution of motor types, nor the additional interactions with cargo such as vesicles or early endosomes. It remains unclear at present whether similar methods would lead to insights in more realistic and complex models. The QSS methodology has also been extended to 2-dimensional models in the context of a searcher alternating between ballistic and diffusive movement phases [6] with linear kinetics. The method presented here for 1D nonlinear models, should extend to two dimensional nonlinear models, provided the conditions on the kinetic terms are met, although it remains an open problem for which classes of nonlinear kinetics and in which spatial dimensions it is possible to analytically find an approximating QSS PDE.

Chapter 3

Coupling Mechanical Tension and GTPase Signalling to Generate Cell and Tissue Dynamics

3.1 Introduction

The Rho-family GTPase proteins are central regulators within signalling networks of eukaryotic cells. While their effects extend to nearly all cell functions, a primary well established role is to control the actin cytoskeleton, actomyosin assembly and myosin contraction [73]. This fact makes Rho GTPases important in regulating cell shape in single cells and in epithelia. Rac1 promotes cell spreading by activating downstream signalling that leads to actin polymerization and cellular protrusions such as lamellipodia. RhoA activates different downstream signalling that in turn activates myosin-induced cell contraction. Hence, while Rac1 promotes cell spreading, RhoA counteracts this by stimulating cell contraction. While previous studies have addressed how GTPases spontaneously segregate to front or back in a cell [54, 64, 95, 99], and how this leads to cell polarization and motility [25, 59], here I focus primarily on the effect of GTPase activity on cell contraction or spreading, and on their interplay with tension and mechanical forces experienced by cells.

Rho GTPases cycle between active and inactive forms: they are activated by guanine nucleotide-exchange factors (GEFs), and inactivated by GTPase-activating proteins (GAPs) [73]. GTPases signalling proteins are interconnected, with crosstalk via a host of proteins. The proteins Rac1, RhoA and Cdc42 are central regulators, downstream of cell-surface receptors that sense a host of stimuli, including small ligand gradients [74], adhesion molecules, extracellular matrix (ECM), substrate stiffness [18], as well as forces and mechanical tension [97].

It has been known for many years that mechanical tension can stimulate cells and lead to signal transduction, but details of the connections were poorly understood. More recently, techniques for measuring forces felt by cells [20, 77] have been used in coordination with methods for observing activity of GTPases [68]. This kind of experimental work has revealed a direct connection between mechanical tension and GTPase activity in cells. For example, Weiner and coworkers [35] showed that the aspiration (which increases tension) of a neutrophil membrane by a micropipette directly inhibits Rac1 activity. When tension is released, Rac1 activity resumes in the cell. Compressing cells was shown to activate RhoA [30] in a rapid and reversible way. Isotropic stretching of vascular smooth muscle cells on an elastic substrate was shown to inhibit Rac (timescale of 5 minutes, recovery over 45 minutes) in [37]. The authors also quantified Rac activity versus % stetch, showing a decrease by about 50% in response to a 15% stretch (Figure 2B in [37]) How cells sense mechanical forces is reviewed in [20, 97], and the identity of multiple Rho GEFs and two GAPs involved in mechanotransduction is summarized in [62].

Cells have diverse mechanosensory mechanisms, and the molecular details of the link between mechanical tension and GTPase activities are still emerging. Specific examples of mechanosensory mechanisms include Rap1 as a tension-sensor and its effect on Rac1 [24] or tension-sensitive calcium ion channels that produce signals to the Rho GTPases [30]. Cellular adhesions and related structures (integrins, vinculin, and talin) act as mechanosensors that funnel signals to central regulators [41, 69]. Membrane tension is known to affect actin assembly directly by limiting polymerization and through a signalling pathway that inhibits actin nucleation via a protein called WAVE2 [21]. Cell-substrate and cell-cell adhesion, cytoskeleton, and their effects on Rho proteins is reviewed in [62]. Other proteins, such as merlin, can act as a mechanochemical transducer by localizing to cortical cell-cell junctions when pulling forces are transmitted from cell to cell in epithelial tissue [15]. Focal adhesion kinase (FAK), for example, inhibits RhoA and activates it in response to tension-dependent integrin reorganization, facilitating cyclic activation of RhoA and Rac1 [91]. Finally, specific proteins for sensing cell membrane curvature can also regulate the cycles of cell protrusion and retraction by controlling Rac1 through GAPs [92].

The connection between mechanical forces and intracellular signalling is a two-way street. On one hand, mechanical tension can influence GTPase activity. On the other hand, GTPases lead to cell deformation (spreading or contraction) that exerts pulling, stretching, or contractile forces on the cell, the local extracellular matrix, and/or neighboring cells. This two-way feedback between chemical and mechanical signalling merits investigation, which is the main focus of this chapter. While mechanochemical interactions have been considered in previous mathematical models for cell behaviours [34, 60, 61, 63, 65], to my knowledge, this is the first instance that mechanochemical interactions are applied to a

GTPase signalling cell and tissue dynamical system.

Rho GTPase are embedded in complex signalling networks, with many effectors, interconnections, and inputs, but proteins such as Rac1, RhoA and Cdc42 play a central regulatory role. Moreover, the details of such networks vary from one cell type to another, and adapt to cell state and environment. Several recent experimental and modelling studies have provided evidence for the hypothesis that certain cell behaviours can be explained as emergent properties of relatively small subsets of these networks, consisting of GTPase modules. Examples of these simple modules include the bistability and hysteresis of cell shape [3, 14, 78] and cell motility behaviour [9], as well as diverse motility phenotypes in melanoma cells on patterned adhesion surfaces [34, 65]. Using simple underlying models for GTPase "circuits" guides the approach here. Instead of attempting to describe the complexity of a large signalling network, which may vary from cell to cell, I restrict attention to a minimal GTPase signalling model and a simplified physical model for cell tension. From this simple, conceptual model, a range of emergent behaviour can be explained. Further fine-tuning and adaptations to specific cells and experimental systems is left to the next modelling step, when mechanistic mathematical models can be studied in conjunction with experiments.

The first step is to consider a single GTPase, such as RhoA, associated with actomyosin contraction. I present a minimal model for RhoA activity, capable of bistable dynamics and link it to feedback from mechanical tension. High RhoA activity leads the cell to contract, which generically results in the reduction of tension from any applied stretch (I do not assume a specific biophysical tension-sensing mechanism). I study this conceptual mechanochemical model in a single cell, without spatial effects. I characterize high or low GTPase activities and transitions between these, and the coupled dynamics of cell tension. Owing to the simplicity of this two ordinary differential equation model, it is possible fully characterize parameter-dependence and delineate regimes of behaviour through numerical bifurcation analysis. In a the "single-cell GTPase-tension model", there exist regimes of (1) high and (2) low RhoA (corresponding to contracted or relaxed cells) separated by (3) regimes of spontaneous, persistent cycling between these states which correspond to cycles of contraction and relaxation in the cell.

I then consider the dynamics of the minimal model when many cells are coupled together mechanically in a 1D role or in a 2D epithelial sheet. In a collective, when one cell changes shape, forces are transmitted to neighbouring cells which are then transduced into GTPase signalling. Despite the simplicity of the conceptual model, multicellular systems exhibit a variety of interesting behaviour. Tissues can contract or oscillate as a whole, or waves and spatially correlated dynamical patterns of activity and size can emerge in large 1D or 2D tissues.

In the final step, I also consider a related GTPase circuit consisting of both Rac1 and RhoA (henceforth Rac and Rho) and mechanical tension. Mutual inhibition between these has been found in a number of cell types [46, 75] and highlighted in recent biological literature for both normal and malignant cells [9, 28, 65, 67, 78]. The effect of such GTPase interactions on cell shape has been explored theoretically [34, 49], but the two-way feedback between cell mechanics and cell signalling is the main theme that motivates the work herein.

3.2 Minimal Model for a Single Mechanochemical Cell

First consider the simplest case, where the mechanosensitivity of a single cell affects its GTPase activity (Figure 3.1(A)), which, in turn, affects a contractile actomyosin meshwork in the cell. The minimal model tracks the activity of a GTPase such as RhoA over time in a single cell. (While RhoA is known to redistribute intracellularly, I ignore spatial variations within a cell, so as to build a first working multicellular model.) RhoA acts through Rho-associated protein kinase (ROCK) to phosphorylate myosin light chain, leading to actomyosin contraction. Consequently, to capture the mechanical contraction, associate a mechanical Kelvin-Voigt element (spring-dashpot system) with the cell size. In one dimension, cell size is represented by a length, L (Figure 3.1(C)). A cell at mechanical equilibrium has some constant "rest-length", $L = L_0$ (Figure 3.1(B)). To couple the signalling with the mechanical tension, assume that cell tension, T, proportional to $(L - L_0)$, enhances RhoA activation. Thus, if a resting cell is temporarily stretched, RhoA activity increases. In turn, active RhoA results in contraction of the cell (I assume that active RhoA decreases the rest-length of the cell). As the cell contracts towards its rest-length, the effect of the temporary increase in length is removed (resolving the tension). This reduces the GTPase activity to a lower level. The overall paradigm of the model is shown as a cycle through states following the purple arrows in Figure 3.1(B).

3.2.1 Model Equations and Definitions

For the activity of the GTPase, I adopt the generic equation

$$\frac{dG}{dt} = (\text{Tension-dependent rate of activation})\, G_i - (\text{Rate of inactivation})\, G, \qquad (3.1)$$

where G_i is the level of inactive GTPase. Ignoring spatial variation, and assuming that the total GTPase G_T is roughly constant over the timescale of interest ($G_T = G + G_i =$ constant), leads to a single equation, (3.1), with $G_i = G_T - G$. This equation is a direct adaptation of the 1-GTPase spatially-uniform version of the model in [33], with the addition of the mechanical coupling.

In the case of a linear equation (3.1), that is, if terms in braces are constant, no interest-

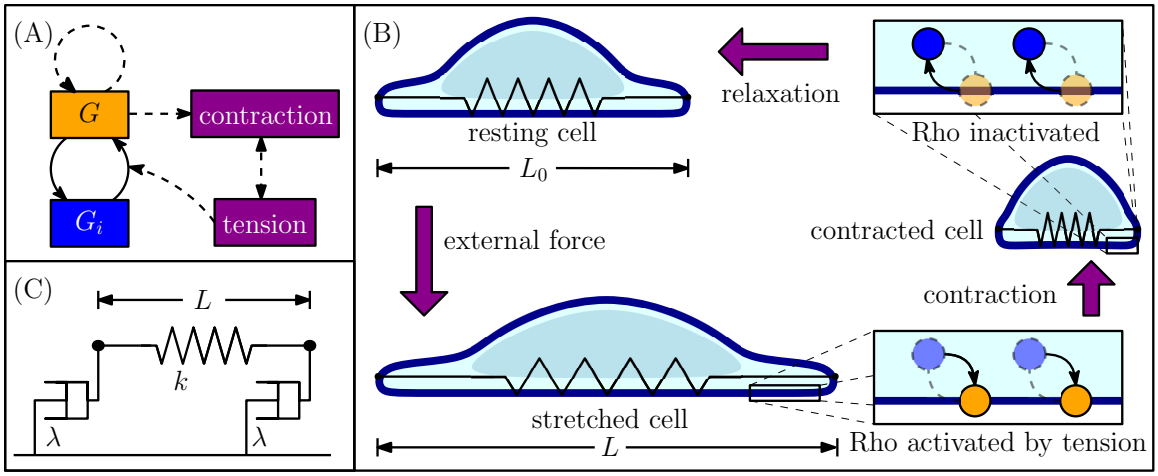

Figure 3.1: The minimal model for coupled GTPase activity and cellular-tension. (A) Schematic of our minimal model for a GTPase "mechanochemical cell". Typical GTPase cycling between active (G, orange) and inactive (G_i, blue) forms. Black arrows denote interconversion (solid), and positive feedback (dashed) from the active GTPase and from tension to GTPase activation. Purple elements (in (A) and (B)) represent mechanical effects. We assume that $G_i = G_T - G$ by conservation. Active RhoA results in cell contraction, which reduces tension. Tension is assumed to increase the activation rate of RhoA. (B) A resting cell (rest length L_0, top left) is stretched by an external force to length L (bottom left); the "spring" schematic represents contractile actomyosin). Tension $T \propto (L - L_0)$ in the stretched cell activates RhoA (inset, lower right, color scheme as in (A)), leading to a coupled mechanochemical system. RhoA activity results in actomyosin-powered cell contraction, which eventually reduces cell tension as the cell approaches its new contracted rest-length. As RhoA is inactivated by the loss of tension (upper right), the cell relaxes. (C) Mechanical representation of the actomyosin cell cortex as a Kelvin-Voigt element.

ing behaviour is found. Some feedback is needed to obtain the nonlinearities that generate bistability and allow for non-trivial dynamics. It is typical to assume positive feedback from active GTPase to its own activation [33, 54] (see [36] for the equivalence of other assumptions). Furthermore, based on the prevalence of GEF-associated mechanotransduction [62], I include the tension-dependent feedback $f(T)$ in the activation rate. This leads to a model equation of the form

$$\frac{dG}{dt} = \left(b + f(T) + \gamma \frac{G^n}{1 + G^n} \right) (G_T - G) - G. \tag{3.2a}$$

where b is basal activation rate (in the absence of feedback from mechanics) scaled by the constant inactivation rate, and γ is a similarly scaled rate of feedback activation. (Details of the scaling are provided in the Appendix.) In this model, cell tension depends on the "size" L of the cell relative to its concurrent rest-length L_0. I considered several forms of

$f(T)$, as described in the Appendix; however, I concentrate on the case that

$$f(T) = \beta \frac{1}{1 + \exp[-\alpha T]}, \quad \text{where} \quad T = L - L_0. \tag{3.2b}$$

The parameter β governs the strength of feedback from tension to GTPase activation. The so-called squashing function in (3.2b) means that the mechanical input has no effect if $L \ll L_0$, but builds up to a maximal level of β for $L \gg L_0$. Consequently, the model GTPase, G, is sensitive to a pulling force, but not to a squeezing or contractile force. It is straightforward to generalize this minimal assumption to other mechanosensory mechanisms, but I only consider the effect of tension here. The parameter α governs the sharpness of the GTPase activation response to cell stretching. It is worth remarking that this form of mechanical model (3.2a) with (3.2b) bears a close resemblance to the equation proposed in [30] for the dynamics of active RhoA in human fibrosarcoma cells that are exposed to mechanical tension. The squashing function has the same basic property of switch-like activation as the Hill-function dependence on T in [30].

For the mechanical coupling, assume that GTPase activity (e.g. RhoA activating ROCK, which activates myosin light chain) effectively shortens the rest length of the "cortical actomyosin spring" promoting contraction. This is described through the following equation for the cell size L:

$$\frac{dL}{dt} = -\varepsilon(L - L_0), \qquad \text{where} \qquad L_0 = \ell_0 - \phi \frac{G^p}{G_h^p + G^p}, \tag{3.2c}$$

and $\varepsilon = 2k/\lambda$ is the rate of contraction. This model assumes that the cell acts as an over-damped elastic spring with Hookian spring constant k, and viscous coupling to a fixed substrate (viscosity λ). The rest length, L_0, is assumed to decrease from a fixed rest length, ℓ_0, depending on the amount of active GTPase within the cell, G. The dependence on G is represented by a Hill function with amplitude ϕ, half-maximum GTPase activity G_h, and power p. For large GTPase activity G, the rest length approaches $L_0 \approx \ell_0 - \phi$, while for low GTPase activity, the rest length remains near ℓ_0. A switch occurs close to the activity level $G = G_h$. The larger p, the sharper the transition between small and large L_0 values. Equation (3.2c) presumes the over-damped regime, where inertial forces are negligible, as appropriate for modelling cell-scale behaviour. Equation (3.2c) follows from a force balance at the two cell ends:

$$\lambda \frac{dx_1}{dt} = k(L - L_0) \qquad \text{and} \qquad \lambda \frac{dx_2}{dt} = -k(L - L_0), \quad \text{where } L = x_2 - x_1, \tag{3.3}$$

for x_1, x_2 positions of the left and right cell boundaries (in 1D), and from $\frac{dL}{dt} = \frac{dx_2}{dt} - \frac{dx_1}{dt}$.

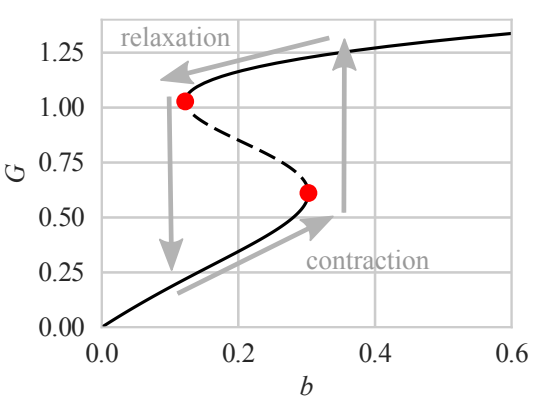

(a) Bistability in GTPase module.

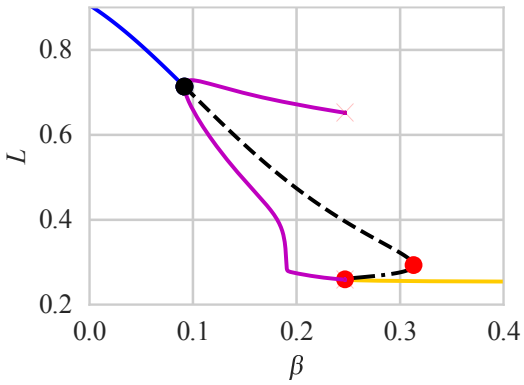

(b) GTPase-tension coupling results in new bifurcations.

Figure 3.2: Bifurcation diagrams for the minimal model (3.2). (a) On its own the GTPase model (3.2a) (with $f(T) = 0$) exhibits bistability with respect to the activation rate b. (Other parameters: $\gamma = 1.75$, $n = 4$, $G_T = 2$). Mechanical tension affects the GTPase activation rate, leading to the possibility of a relaxation oscillator (hysteresis loop) shown in this diagram. (b) Bifurcation diagram for the coupled GTPase-tension minimal model Equation (3.2), showing how cell length L varies with the strength of coupling (β) of tension to GTPase activation. L can be long (small β, solid blue line), oscillatory (middle values of β, magenta line), or short (large β, solid yellow line). In both, red points are saddle node bifurcations, and the black point corresponds to a Hopf bifurcation (after which stable oscillations emerge). Other parameters are $b = 0.1$, $\gamma = 1.5$, $G_T = 2$, $\phi = 0.75$, $G_h = 0.3$, $\varepsilon = 0.1$, $\alpha = 10$, $\ell_0 = 1$, and $n = p = 4$.

3.2.2 Results

The single GTPase model on its own (with $\beta = 0$), is bistable for a range of parameters. As the basal activation rate b increases, the system transitions from a monostable state with low GTPase activity, through a bistable regime, and finally to a monostable state with high GTPase activity (Figure 3.2(a) and [33, 34]). With mechanical feedback ($\beta \neq 0$) as described in Section 3.2.1, there are three regimes of behaviour: (1) for small β, the cell remains relaxed with low GTPase activity, (2) for large β, the cell becomes contracted with high GTPase activity, and (3) for intermediate β, the cell dynamics tends to a stable limit cycle with GTPase activity cycling between low and high levels. The bifurcation diagram of Figure 3.2(b) shows these three regimes of behavior, displaying steady state cell length, L, as a function of the coupling feedback strength, β. For this choice of parameters, the three regimes of behavior occur for different intervals of β; however, for different parameter values, it is possible that the limit cycle and contracted steady-state can both be stable for the same value of β.

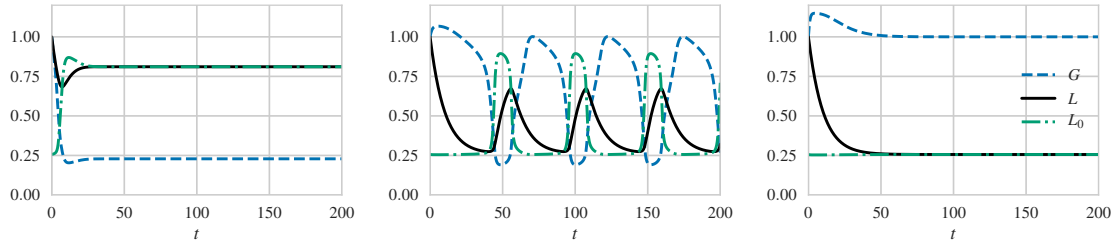

(a) $\beta = 0.05$ (b) $\beta = 0.2$ (c) $\beta = 0.3$

Figure 3.3: Dynamics of the minimal model for a single cell with one GTPase ("RhoA") and feedback from tension to GTPase activation, Equation (3.2). In (a), the feedback strength from tension ($\beta = 0.05$) is weak, and the cell remains relaxed. In (b), the feedback ($\beta = 0.1$) is of intermediate strength, and limit cycle oscillations arise. In (c), the coupling is so strong that GTPase activity is always high, and the cell stays in a contracted state. Parameters are $b = 0.1$, $\alpha = 10$, $\gamma = 1.5$, $n = p = 4$, $G_T = 2$, $\phi = 0.75$, $G_h = 0.3$, $\varepsilon = 0.1$ and $\ell_0 = 1$. When the GTPase activity level is close to $G = G_h$, the cell rest length changes sharply from $L_0 \approx \ell_0$ to $L_0 \approx \ell_0 - \phi$ (green dash-dotted), resulting in the dramatic changes in cell length seen in (B). Some lag stem from the slower dynamics of L, due to the slow mechanical response (small parameter ε).

The dynamics of the cell size (L, solid), rest-length (L_0, dash-dotted curve) and GTPase activity (G, dashed curve) is shown in Figure 3.3 for each of these regimes. When the feedback from tension upon GTPase activation is small, (a) $\beta = 0.05$, the cell remains relaxed. As the feedback parameter increases, (b) $\beta = 0.2$, the cell oscillates, or (c) for $\beta = 0.3$, the cell contracts and maintains a small length.

The results can be understood based on known dynamical systems behaviour of a bistable system (the GTPase activity) with slow negative feedback (the mechanical contraction). The coupling can constrain the bistable system to either its low or its high steady state levels, or, for intermediate coupling, lead to a trajectory around a hysteresis loop. In the latter case, the system behaves as a relaxation oscillator due the separation of time scales between fast G and slow L (note the small parameter ε in the L ODE). As shown by the hysteresis loop in Figure 3.2(a), the activation rate is increased when the cell is stretched, eventually leading to a transition from low to high GTPase activity. At this point, the GTPase activity leads to cell contraction, effectively decreasing the rest length L_0. As the cell contracts, L approaches L_0, and tension decreases, reducing GTPase activation rate and transiting to the low GTPase state. This resets the rest-length to a larger value. With the appropriate relative timescales of mechanics and chemical signalling, this cycle repeats, setting up the limit cycle oscillations.

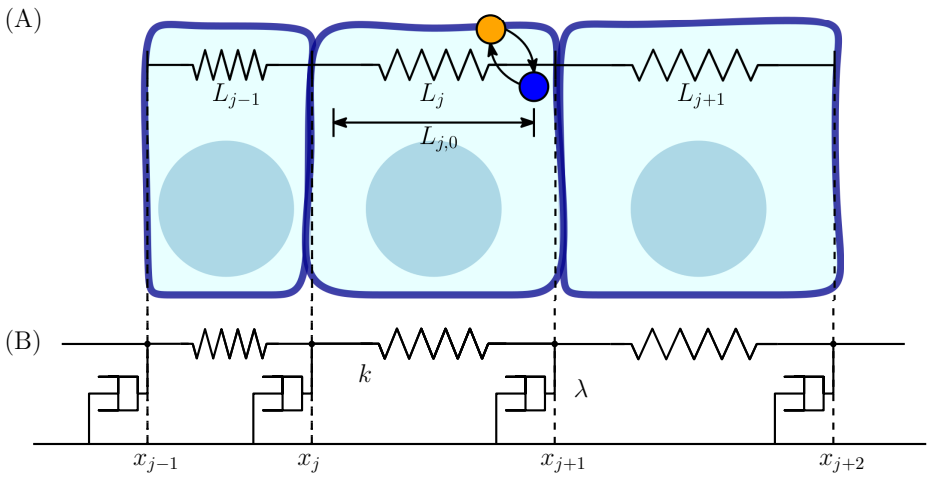

Figure 3.4: Cell interactions in a 1D array of "model cells". (A) The contraction-relaxation of each cell affects the force of pulling on its neighbours. Each cell has its own internal GTPase signalling. (B) The array behaves much like a system of over-damped springs in series. The GTPase signalling affects the rest-lengths of the springs L_j, and the dynamics then moves the nodes x_j that represent cell borders.

3.3 Mechanical Coupling in a 1D Array of Cells

Having characterized the minimal "model cell", next consider the behaviour of a coupled array of such cells. As a first step, consider coupled cells mechanically in one spatial dimension (1D), as shown in Figure 3.4. Here the lengths of the cortical actomyosin Kelvin elements are simply the distances $L_j = x_{j+1} - x_j$, $j = 1, \ldots, N-1$ between "nodes" (edges of cells along a 1D axis). Each cell has its own internal GTPase signalling, following Equation (3.2a), and only responds to neighbouring cells through mechanical force. Hence, the motion of the cell ends, x_j, is prescribed by the following system of ODE:

$$\lambda \frac{dx_1}{dt} = k(L_1 - L_{1,0}), \tag{3.4a}$$

$$\lambda \frac{dx_j}{dt} = -k(L_{j-1} - L_{j-1,0}) + k(L_j - L_{j,0}), \tag{3.4b}$$

$$\lambda \frac{dx_N}{dt} = -k(L_{N-1} - L_{N-1,0}), \tag{3.4c}$$

with $j = 2, \ldots, N-1$ giving the index j of the $N-1$ cells. The rest-length in each cell, $L_{j,0}$, is coupled to GTPase signalling according to Equation (3.2c).

3.3.1 Tissue Dynamics in 1D Depend on Mechanical Feedback Strength

When many cells are coupled together, new tissue-level behaviours emerge. For example, as one cell is displaced or contracts, its neighbours are stretched or squeezed. This change in

length then affects tension, T, and ultimately the GTPase activity, G of the neighbour(s), that can similarly affect their neighbours, and so on. The emergent behaviour depends on the signalling parameters of the individual cells. For example, if the strength of feedback from mechanics to GTPase activity, β, is sufficiently small or sufficiently large everywhere, the entire tissue will be relaxed (and long) or highly contracted (and short), respectively. Examples of these behaviours are shown in Figure 3.5(a) and (c).

For β in the single-cell oscillatory regime ($\beta = 0.2$, as in Figure 3.3(b)) a small array of cells ($N = 10$) can exhibit synchronous oscillations, as shown in Figure 3.5(b). In this case, as each cell expands or contracts, the force exerted on its nearest neighbours induces a change in the chemical signalling, which results in the coordination of the entire group (possibly excluding the cells at either end). This shows up as coherent bands of colour in Figure 3.5(b) while the total length of the array (vertical dimension in Figure 3.5) oscillates.

I next asked whether a propagating wave of contraction, similar to that obtained in the work of Odell et al. [61] (as discussed in Chapter 1), could be obtained with this model. To explore this, I set up a simulation in which each cell would sit in the relaxed-length steady-state, but provide an initial GTPase perturbation to one or more cells at the end of a tissue. I was unable to reproduce a wave of contraction in this way. However, using a modification of the model with linear feedback (instead of the squashing and hill functions) between GTPase signalling and tension, I was able to produce wave-like behaviour. The specific parameters and feedback functions for this linear-feedback model are collected in Section B.3. The wave of contraction behaviour is shown in Figure 3.5(d) where two cells at the right end of the row are initially "stimulated" with high GTPase activity, while the rest of the cells are at their relaxed steady-state. Contraction of the stimulated cells stretches their immediate neighbours to the left, which activates new GTPase signalling in those neighbours and subsequent contraction. In this way, a unidirectional wave of GTPase activity and contraction sweeps across the entire row of cells. As discussed later, this wave of contraction resembles a wave associated with zippering in the neural tube closure of an ascidian embryo [29].

As the number of cells increases, the spatial extent of the mechanical force transduction can no longer span the entire "tissue", and appears to become localized to some neighbourhoods. Then, patches of contraction and relaxation emerge; these can propagate throughout the tissue as waves of contraction-relaxation. Typical examples for 50 and 100 cells in such 1D arrays are shown in Figure 3.5(e) and (f). In such large arrays, GTPase activity is also seen to form wave patterns that sweep back and forth across the 1D domain. This leads to the slanted bands of colour in Figure 3.5(e) and (f). Even though the GTPase activity is not directly coupled between cells, the mechanical coupling effectively leads to GTPase coordination on some spatial and temporal scale.

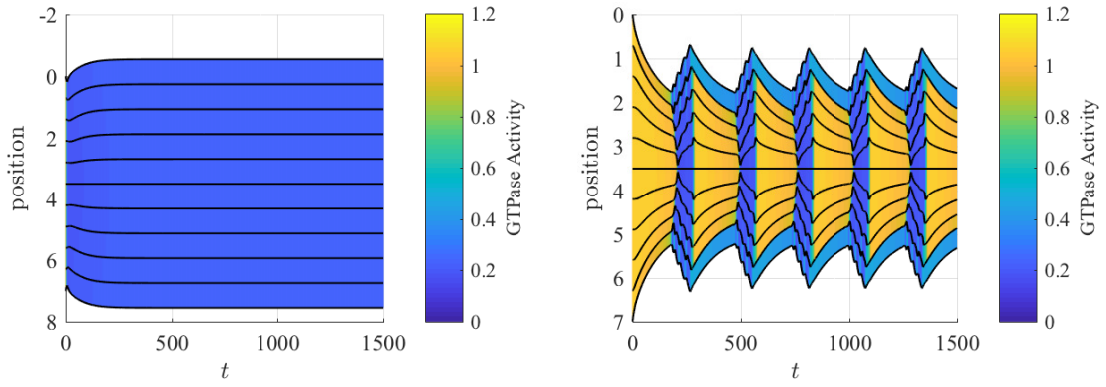

(a) $\beta = 0.05$, 10 cells

(b) $\beta = 0.2$, 10 cells

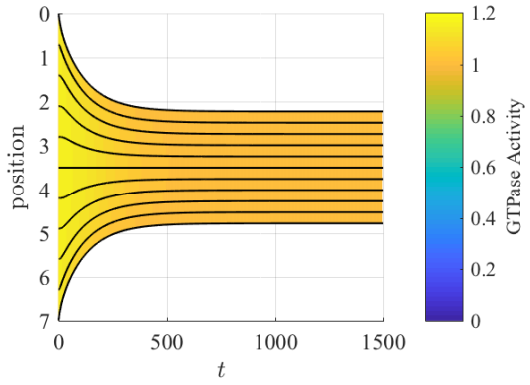

(c) $\beta = 0.3$, 10 cells

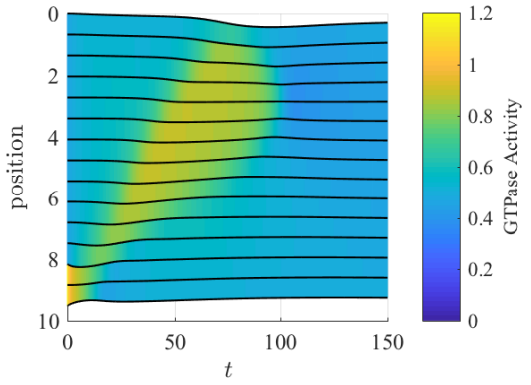

(d) Wave of contraction, 14 cells

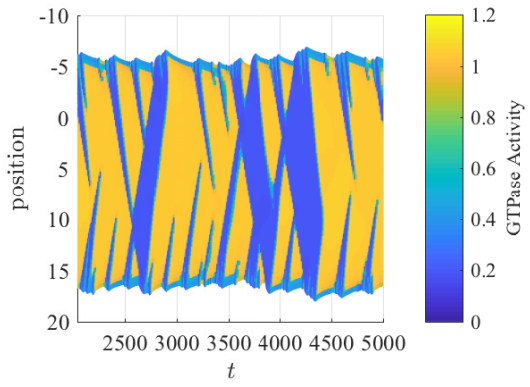

(e) $\beta = 0.2$, 50 cells

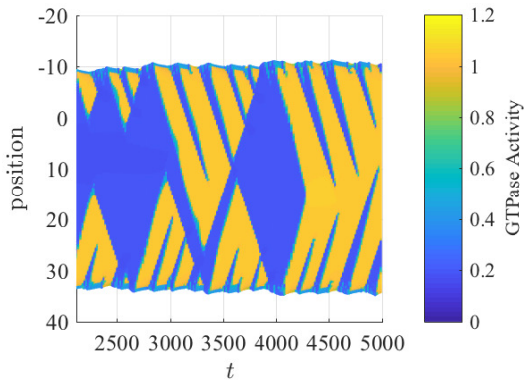

(f) $\beta = 0.2$, 100 cells

Figure 3.5: 1D tissue dynamics result from mechanochemical interactions. Kymographs show the 1D position of cell edges (vertical axis, black curves; suppressed for clarity in (e), (f)) with colour indicating the GTPase activity within each cell. Parameters as in Figure 3.3(b), except in (d). For a small number of cells ($N = 10$), the tissue can be (a) relaxed, (b) oscillatory, or (c) contracted. (d) An initial perturbation of GTPase activity at one end of the row can propagate a wave of GTPase activity and contraction throughout the whole row of cells. Larger number of cells: (e) $N = 50$, (f) $N = 100$: waves of contraction and relaxation propagate across the tissue and model details in Section B.3.

I did not explore all possible behaviours of this 1D cell collective, and an analytical or numerical analysis of the behaviour of the cell collective is warranted to delineate possible regimes of behaviour. Nonetheless, the examples provided in this section illustrate an interesting range of behaviour. A limitation of the 1D approach is that each cell only interacts with 2 neighbours and cell shape does not play a role. As such, in the next section, I study a realization of the GTPase-tension model in a 2D setting.

3.4 Cell shape and cell-cell interactions in 2D epithelial sheets

3.4.1 Adapting the Model

In order to describe cell expansion and/or contraction in 2D, I modified the model to represent changes in projected cell area, A, rather than cell length. Generalizing from the 1D model, assign a "resting cell area" A_0 to the cell, and assume that positive $(A - A_0)$ corresponds to an average cell-stretching tension that has an effect in 2D similar to $(L - L_0)$ in the 1D model cell. This assumption could be modified, scaled according to $A \approx cL^2$, or adapted to experimental data. In the context of the simple conceptual model, the main effect, preserved by these assumptions, is that GTPase activity and mechanical tension switch one another on or off.

To simulate cell shape and intracellular chemistry, I worked with Dhananjay Bhaskar to use a publicly available software package, CompuCell3D, that represents cell shapes using the Cellular Potts model (CPM) formalism [90] as introduced in Chapter 1. Briefly, the pixel-based motion of a cell edge outwards (expansion) or inwards (contraction) is governed by a Hamiltonian, $\mathcal{H}$, describing the total energy in the system. The Hamiltonian includes adhesion energies, and volume constraints (area constraint in 2D). At each time step (called a Monte-Carlo step (MCS)) in the simulation, several small changes are introduced, called pixel-copy or spin-copy attempts. The CPM algorithm accepts such changes if this decreases the Hamiltonian (overall energy of the system), or accepts it randomly otherwise as a small noise-induced fluctuation. While CPM does not explicitly track forces, it has recently been shown to be consistent with other simulations where forces are made explicit [47], for example, vertex-based cell models.

Several aspects of the simulations were adapted to the technical requirements of the Cellular Potts model (CPM). The timescale τ and notion of a "target area", A_T, was introduced. The actual cell area A and the GTPase-governed target cell area A_T are tracked in each CPM cell. The target area for a cell is determined by a system of ODEs that couple sub-cellular biochemistry (assuming that the cell is well-mixed) to cell mechanics. This

leads the following model equations for the GTPase activity G and target area A_T:

$$\frac{1}{\tau}\frac{dG}{dt} = \left(b + f(T) + \gamma\frac{G^n}{1+G^n}\right)(G_T - G) - G, \tag{3.5a}$$

$$\frac{1}{\tau}\frac{dA_T}{dt} = -\varepsilon(A_T - A_0(G)), \quad \text{where} \quad A_0(G) = a_0\left(1 - \phi\frac{G^p}{G_h^p + G^p}\right). \tag{3.5b}$$

Here, a_0 is the constant baseline cell area. The target area A_T approaches A_0 on the timescale τ that can be controlled to increase or decrease the speed of the feedback. Note that cell area A does not approach target area A_T instantaneously, but through the addition or removal of lattice sites over several MCS. That is, A, is updated stochastically to approach the target area A_T by the CPM. Here, I also assumed

$$f(T) = \beta\frac{A^m}{A_T^m + A^m}, \qquad \text{where} \qquad T = A - A_T. \tag{3.5c}$$

Tension is defined as $T = A - A_T$, which is a "delayed" form of $A - A_0$. In turn, the function $f(T)$, describes the feedback on GTPase activation from tension. This Hill function has the property that as m increases, its shape is fundamentally similar to that of the squashing function used in the 1D GTPase model (Equation (3.2b)). For this exploration, I again assume that GTPase activity is uniform inside a given cell through variable across the entire collection of cells. Stochasticity in the CPM leads to interesting behaviour (e.g., stochastic switching) which is not observed in deterministic numerical solutions.

As before, assume that increasing tension (represented as the difference between target area and actual cell area), can increase GTPase activity via Equation (3.5c). To appropriately calibrate the CPM to observe the same oscillatory dynamics as in the one-cell single GTPase model, it is necessary to choose the timescale and the time step for numerically integrating the ODEs, τ and Δt, respectively, so that each MCS is $\tau\Delta t = 2000 \cdot 0.001 = 2$ units of time t. In the next section, I consider the GTPase-tension model in a single 2-dimensional cell, and later consider the coupling between interconnected cells.

3.4.2 Single Cell Dynamics

With appropriate calibration, the 2D Cellular Potts model (CPM) implementation recapitulates the behaviour found in the single cell model. As shown in Figure 3.6(a) and Appendix Figure B.10, a parameter set corresponding to 1D cell oscillations also led to single-cell oscillations in the 2D CPM cell. The CPM also produces relaxed cells and contracted cells for corresponding parameter sets in the 1D model, see Appendix Figure B.8 and B.9 for relaxed cells.

Cellular Potts model simulations have inherently stochastic behaviour due to the al-

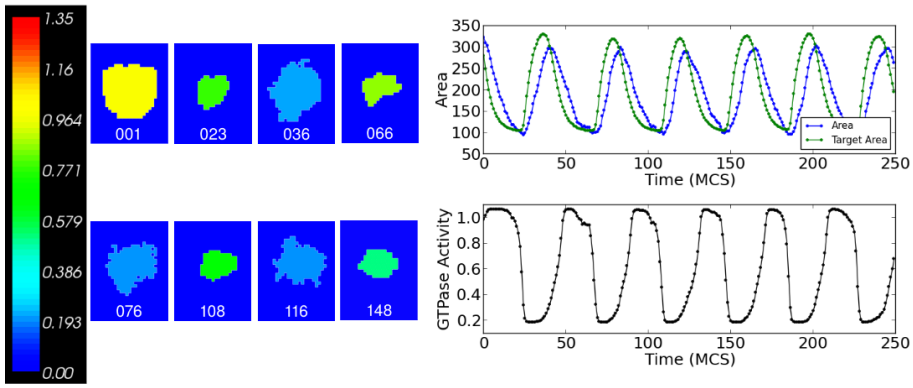

(a) Single cell oscillations, $\beta = 0.2$.

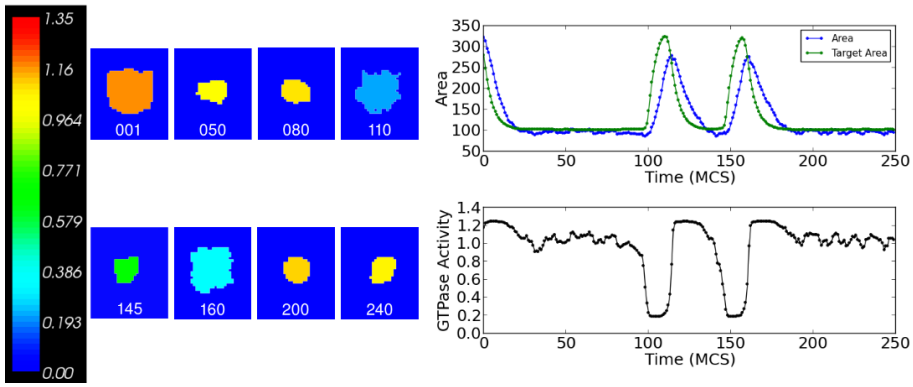

(b) Single cell, stochastic oscillations, $\beta = 0.5$

Figure 3.6: Single cell oscillations in 2D cells simulated with the Cellular Potts model (CPM) CompuCell 3D software [90]. In (a) and (b), cell color represents a (spatially uniform) GTPase activity level from low (blue) to high (yellow and orange), as shown in the color bar. Cell shape changes over time as indicated by the progression of snapshots numbered by the Monte-Carlo step (MCS) of the CPM (MCS increase left to right and top to bottom). Cell target area (green) and actual area (blue) as well as GTPase activity is plotted over 250 MCS of the CPM. In (a), $\beta = 0.2$ results in a single oscillatory cell. In (b), the cell stochastically switches between high GTPase steady state (corresponding to $\beta = 0.5$) and a large amplitude limit cycle. Other parameters were: $\tau = 2000$, $b = 0.1$, $m = 10$, $\gamma = 1.5$, $n = p = 4$, $G_T = 2$, $\varepsilon = 0.1$, $a_0 = 400$, $\phi = 0.75$, and $G_h = 0.3$.

lowable random fluctuations mentioned above. As a result, I found new behaviour that was not found in the deterministic 1D cell simulations, namely that spontaneous cycles of high to low GTPase level (and low to high cell areas) could occur, even in parameter sets consistent with monostable states. An example of this type is shown in Figure 3.6(b). Here, parameter values were set to the stable small-size single-cell regime in the 1D model ($\beta = 0.5$). The cell was in a contracted state for some time, but displayed two cycles of contraction-relaxation, at MCS 100 and 150, before returning to its quasi-quiescent state. In Appendix Figure B.11, there is an example of cells switching between small and large limit cycle oscillations for $\beta = 0.175$.

3.4.3 Coupling CPM Cells in 2D

What happens when there are multiple cells in the 2D simulation? To answer this question, consider two types of situations in which N cells are present, where each cell is governed by its own set of 2D equations (see Apppendix) with the same set of parameters but with random initial conditions. As shown in Appendix Figure B.2 for $N = 9$ cells, the first implementation was of cells that have no direct mechanical coupling. As expected, in this case, cells behave independently with distinct and uncorrelated copies of the dynamics. The Rho GTPase levels inside such cells (top, Appendix Figure B.3) remain unsynchronized, as detected by the Kuramoto order parameter and the variance in the phase (details in Appendix Section B.5).

Next, consider cells that were contiguous and can interact via adhesion terms in the CPM Hamiltonian (details in Appendix Section B.4). Essentially, cells that have larger interfaces with their neighbours have stronger adhesion (and lower adhesion energy). An example of such simulations are shown in Appendix Figure B.4. As a cell changes size, neighbouring cells are affected through cell-cell adhesion. As one cell area contracts, its neighbours are stretched, causing their tension, proportional to $(A - A_T)$, to increase. This promotes a neighbour's GTPase activity, and leads it to contract. In this way, mechanical forces are propagated throughout the tissue and affect GTPase signaling in each cell. As seen in Appendix Figure B.5, GTPase activities rapidly synchronize in the entire group of 9 cells, with a few small fluctuations in phase seen occasionally. In collaboration with Dhananjay Bhaskar, we used the Kuramoto order parameter to quantify the degree of synchronization between the 9 cells. The Kuramoto order parameter is a complex number whose magnitude measures the phase-coherence of oscillators and can vary between 0 and 1. When oscillators are close in phase, the Kuramoto order parameter is closer to 1 ([42], [89] for a review). The larger Kuramoto order parameter and lower variance in the phase (note scaling on the vertical axis) as compared with simulation for independent cells (Appendix Figure B.3) also confirms this synchronization.

The strength of cell-cell adhesion can affect the results. As shown in the sequence of Appendix Figure B.5-B.7, as cells become more adhesive to one another ("low cell-cell adhesion energy") than to the surrounding "medium", the mechanical coupling is stronger, and the synchronization of cell oscillations is more regular.

3.4.4 Waves of Contraction and GTPase Activities in 2D Model Tissue

Next, again with Dhananjay Bhaskar, we asked how larger numbers of cells, also in 2D CPM, would behave when coupled mechanically through their adhesion. To probe this question, consider a simulation with a circular tissue composed of 373 contiguous cells with initial areas randomly chosen. As before, parameters of each cell are in the oscillatory single-cell regime. Results are shown in Figure 3.7 for the case of intermediate adhesion, in Figure 3.8 for the case of strong adhesion, and in Appendix Figure B.12 for the case of weak adhesion. Here the 2D tissue is much larger than a few cell diameters. Figures 3.7 and 3.8 show two views of the same "tissue", one (a) indicating cell area on a colour scheme of blue (small) to yellow (large), and a second (b) representing the concurrent GTPase activity level from low (blue) to high (orange).

In contrast to the case of few cells, where synchronized oscillations were observed over the entire population, synchronization is limited to patches in larger tissues. Moreover, waves of contraction/relaxation and GTPase activity propagate throughout the tissue. This behaviour can be seen in the successive snapshots in Figure 3.7(a) and (b) for the case of intermediate cell-cell adhesion. Bands of highly contracted cells (dark blue) are noteworthy in several panels in Figure 3.7 (a), and coincide with interfaces between zones of high and low GTPase activity in Figure 3.7 (b).

The strength of cell-cell adhesion affects the strength of coupling and extent of synchronization. In the case of weak cell-cell adhesion (Appendix Figure B.12(a) and (b)) relatively small patches are seen, and cells tend to detach from the periphery of the tissue. Waves of contraction and expansion are observed. As cell-cell adhesion is increased from the baseline simulation in Figure 3.7, cells are more likely to favour adhering to each other. They then experience larger changes in area as one of their neighbours shrinks or grows. This results in nearly the entire tissue of cells expanding and contracting, though we still tend to see a wave of synchronization spreading from the centre to the edge of the tissue, as in Figure 3.8. This leads to the conjecture that the patch size (number of cells in a group with coordinated behaviour) increases with the strength of cell-cell adhesion.

In the final CPM experiment, consider the case that cells are heterogeneous, with a range of values of the feedback parameter β coupling mechanics to the GTPase activation. Consider a large simulated tissue with values of β assigned randomly to each cell. Results are shown in Figure 3.9. With the range of values of β, individual cells could be either

contracted, oscillatory, or relaxed. Due to the presence of some oscillatory cells in the tissue, those cells which would normally be quiescent at either relaxed or contracted steady-states, undergo oscillations due to pulling by oscillatory neighbours. Patches of activity in the tissue persist, though with a heterogenous GTPase activity. These forced oscillations are suggestive of a mechanism by which tissue dynamics can be driven by a few pace-maker cells, whose phenotype is oscillatory. I discuss how these model predictions relate to epithelial dynamics in biological systems in §3.6.

3.5 Rac and Rho GTPase Model

In this section, I determine whether some of the lessons learned from the single-GTPase model would carry over to similar conclusions in a slightly expanded Rac-Rho GTPase circuit. It is well-known that Rac1 and RhoA are mutually inhibitory under many situations [9, 67, 78]. Here, the analysis starts from the well-mixed variants of the Rac-Rho model described in [33], and in the melanoma-based modelling of [34]. In the latter case, coupling of front and rear compartments of a cell (through extracellular matrix signalling) was found to lead to the possibility of distinct behavioural regimes, including stable high Rho or Rac, or cycling between those levels. Here the mechanical coupling has an effect similar to the ECM coupling in that paper.

In the mutually inhibitory Rac-Rho model, the total level of Rac (Rho) GTPase, R_T (ρ_T) is assumed to be roughly constant over the timescale of interest. Hence only the active forms of the GTPases need to be tracked. Assuming that each of Rho and Rac inhibits the activation of the other, consider the set of equations

$$\frac{dR}{dt} = \frac{b_R}{1+\rho^n}\left(R_T - R\right) - \delta R, \tag{3.6a}$$

$$\frac{d\rho}{dt} = \left(b_\rho + f(T)\right)\frac{1}{1+R^n}\left(\rho_T - \rho\right) - \rho, \tag{3.6b}$$

where $f(T)$ represents the activation of Rho GTPase by tension T as in (3.2b). As before, Rho GTPase activity decreases the rest-length of the cell:

$$\frac{dL}{dt} = -\varepsilon\left(L - L_0\right), \qquad \text{where} \qquad L_0 = \ell_0 - \phi\frac{\rho^p}{\rho_h^p + \rho^p}. \tag{3.6c}$$

Note that while Rac is a candidate for mechanosensory inputs and also has an affect on cell size, I initially assume that only Rho is affected by tension and has an affect on cell length.

On its own, without feedback from mechanics, the minimal Rac-Rho mutual inhibition model has a region of bistability, as shown in Figure 3.10(a). As either the basal activation rates, b_ρ or b_R, increase, the system transitions from a monostable state with either species

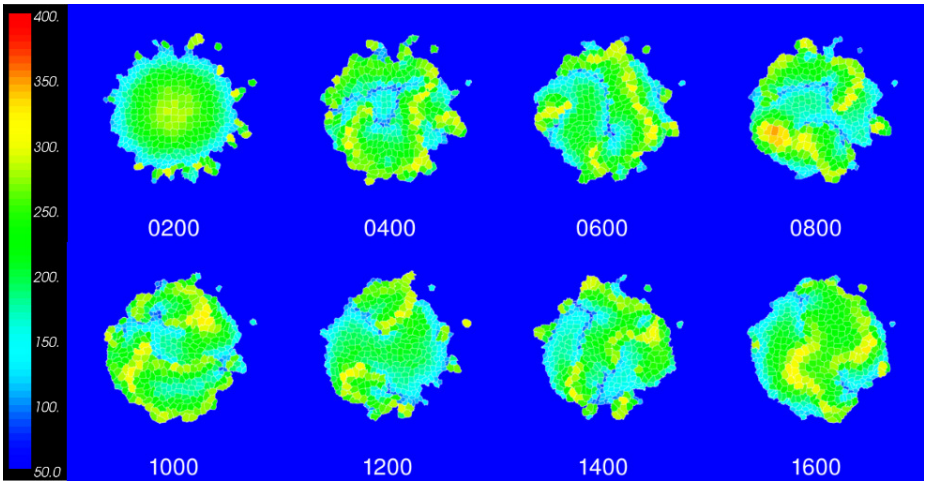

(a) Cell area in a 2D tissue over time.

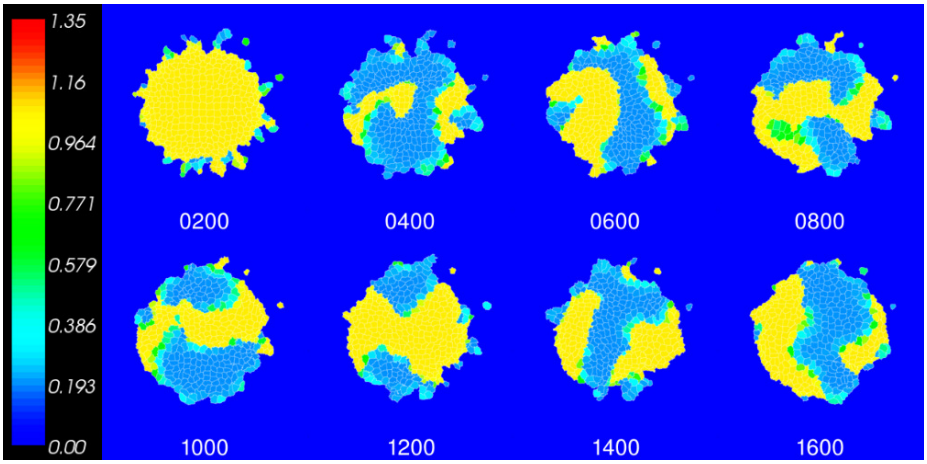

(b) GTPase activity in the same 2D tissue over time.

Figure 3.7: Simulation of a 2D "tissue" ($N = 373$ cells) in the intermediate adhesion scenario using CompuCell3D [90]. Individual cells satisfy the minimal GTPase-tension model, with $T \propto (A - A_T)$, where A is cell area, and A_T is the target area. Cell-medium adhesion energy (80) is equal to cell-cell adhesion energy (80) in the Hamiltonian, $\mathcal{H}$. In (a), cells are coloured based on their current cell area, while in (b), cells are coloured based on the uniform level of GTPase activity within each cell. Cells with smallest area (dark blue in (a)) are correlated with an interface between high (orange) and low (blue) GTPase activity in (b). Waves of contracting cells and relaxing cells are observed throughout patches in the tissue. Parameters listed in Appendix Section B.4 and B.6.

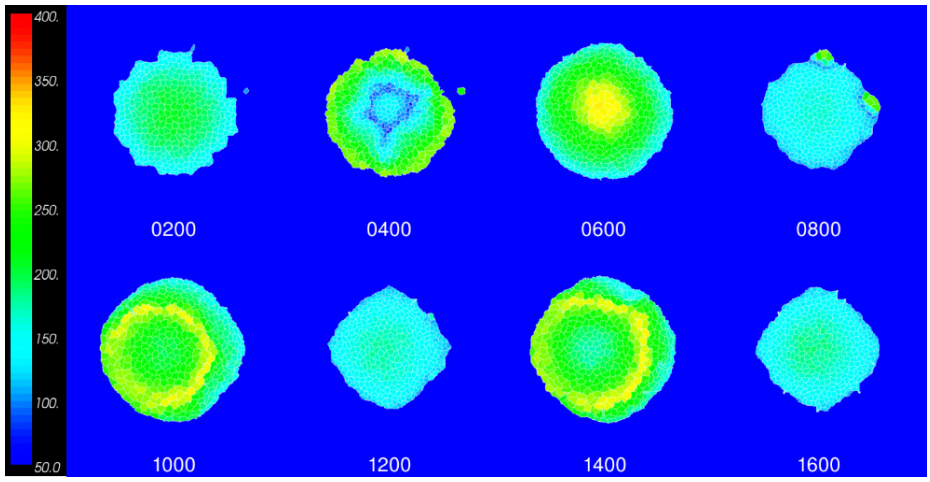

(a) Cell area in a 2D tissue over time.

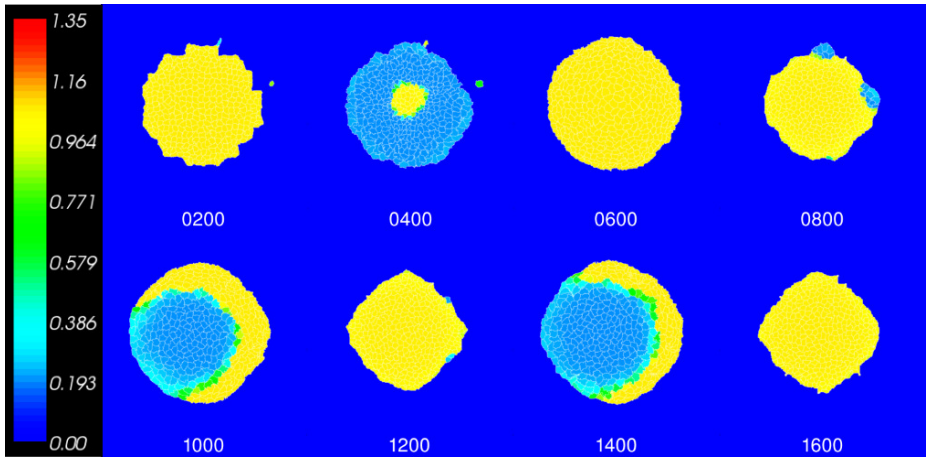

(b) GTPase activity in the same 2D tissue over time.

Figure 3.8: As in Figure 3.7 but for the strong adhesion scenario. Cell-medium adhesion energy (80) is greater than cell-cell adhesion energy (30) in the Hamiltonian, $\mathcal{H}$. The entire tissue is synchronized. In (b), cells are coloured by area, while in (b), cells are coloured by GTPase activity. Notice that cells at the outer edge are first to expand/contract as they are less constrained by neighbours, so that expansion/contraction is 'outside-in'. Parameters are the same as in Figure 3.7, and are listed in Appendix Section B.4 and B.6.

at a high steady-state (and the other at a low steady-state) or from a coexistence state, into the bistable regime. Assume, as before, that stretching a cell would increase the activation rate of RhoA. With that assumption, the same regimes of behaviour as in the single GTPase model (Section 3.2.1) occur in the Rac-Rho model. These three regimes of behaviour depend on the strength of feedback from tension to Rho activation (a parameter denoted γ_ρ). The dependence is shown in the bifurcation diagram in Figure 3.10(b). For small γ_ρ, the cell remains long and relaxed, with high levels of Rac activity and low levels of Rho activity

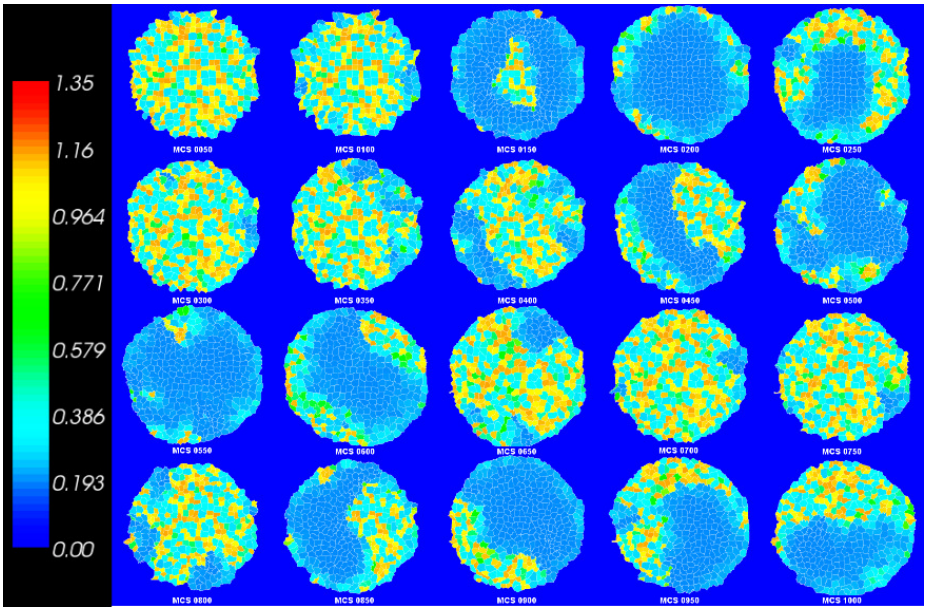

Figure 3.9: As in Figure 3.7 (b), but with the parameter β (feedback strength from tension to GTPase activation) initially randomly chosen for each cell. Cells are coloured by GTPase activity. Cells in steady state are forced to oscillate due to mechanical coupling with cells that are in the limit cycle regime. In this case, the baseline area parameter is increased $a_0 = 600$ (resulting in larger variation in cell area), and temperature parameter of Potts model $T = 15$ is decreased from baseline. In the Hamiltonian, $\mathcal{H}$, cell-cell adhesion energy is 60, and cell-medium adhesion energy is 80. Other parameters are as in Appendix B.4 and B.6.

(Figure 3.11(a)). For large γ_ρ, the cell is contracted, (small L) with low levels of Rac activity and high levels of Rho activity (Figure 3.11(c). For intermediate γ_ρ, limit cycle oscillations arise (Figure 3.11(b)). There is a regime of parameter space where a stable limit cycle and stable steady-state coexist (approximately $12.29 \leq \gamma_\rho \leq 15.61$). In this parameter regime, depending on initial conditions, the cell may either end up in the oscillatory regime, or at the contracted cell state.

In the above Rac-Rho model, I considered only coupling between mechanical tension and Rho activity, ignoring possible direct effects of mechanosensing on Rac activity. Rac is known to cause cell spreading via actin assembly, an effect that I had similarly omitted. To check the possible outcomes of such additional factors, I briefly explored several variants of the above default Rac-Rho-tension model. Specifically, I experimented with inclusion of (1) the effects of compression (as opposed to tension) sensing with feedback to Rac activation and (2) the effect of Rac activity on cell size, modelled as an increase in the rest-length L_0. Feedback from mechanics to Rac activation can be interpreted as a change in b_R in Figure 3.10(a). This can push the underlying Rac-Rho signalling model into a

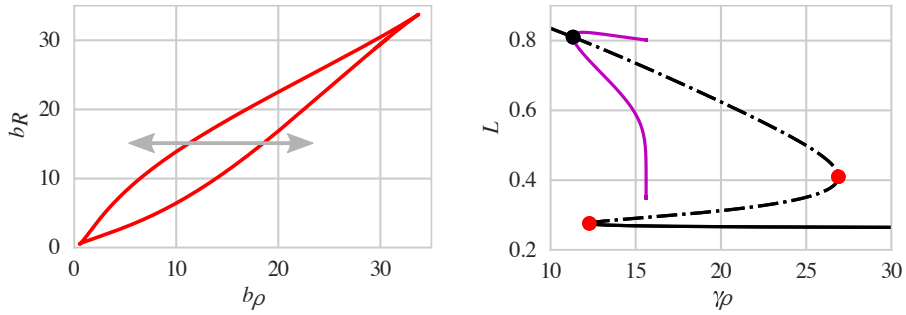

(a) Bistability (inside curve) in the Rac-Rho model without tension.

(b) GTPase-mechanics coupling results in a range of possible dynamics.

Figure 3.10: Bifurcation diagrams for the minimal Rac-Rho model of Equations (3.6). (a) On its own, the Rac-Rho model (with $\beta = 0$) exhibits bistability (inside red-bordered region) with respect to the activation rates b_R and b_ρ. Mechanical tension affects the Rho GTPase activation rate, leading to the possibility of a relaxation oscillator by traversing the bistable region (grey arrows). (b) Bifurcation diagram for the coupled Rac-Rho-tension minimal model (3.6), showing how cell length L varies with the strength of coupling (γ_ρ) of tension to Rho activation. L can be long (small γ_ρ, solid black line), oscillatory (middle values of γ_ρ, magenta curve), or short (large γ_ρ, solid black line). As opposed to the single GTPase-tension model, it is possible for a stable limit cycle to coexist alongside a stable steady-state (for $12.29 \leq \gamma_\rho \leq 15.61$). Here, the red points correspond to saddle node (fold) bifurcations, and the black point to a Hopf bifurcation. Other parameters are $b_R = 15$, $b_\rho = 5$, $R_T = \rho_T = 4$, $\delta = 1$, $n = p = 3$, $\gamma_L = 0.75$, $\varepsilon = 0.1$, $\alpha = 10$, $\rho_h = 1$ and $\ell_0 = 1$.

regime of different behaviour—high Rac, bistability, coexistence, or low Rac—and alter the resulting cell behaviour accordingly (in a mechanical feedback-dependent manner). In these additional numerical experiments, behaviour similar to Figure 3.11 arises; albeit with Rac activity increasing the cell length and the relaxation oscillation arising from compression instead of tension.

Aside from the above complementary Rac-feedback-only model, I guided an undergraduate advisee, Jim Shaw, to experiment with mixed Rac and Rho feedbacks and antagonistic effects on cell size. With Jim Shaw, I also considered feedback from tension and/or compression to GAPs as well as GEFs (inactivation versus activation terms in the GTPase equations). Overall, similar regimes of behaviour can be found in many such examples, within smaller or larger regions of parameter space. Cases of specific interest should henceforth be linked to specific biological examples where the mechanical coupling to known GEFs or GAPs is of interest.

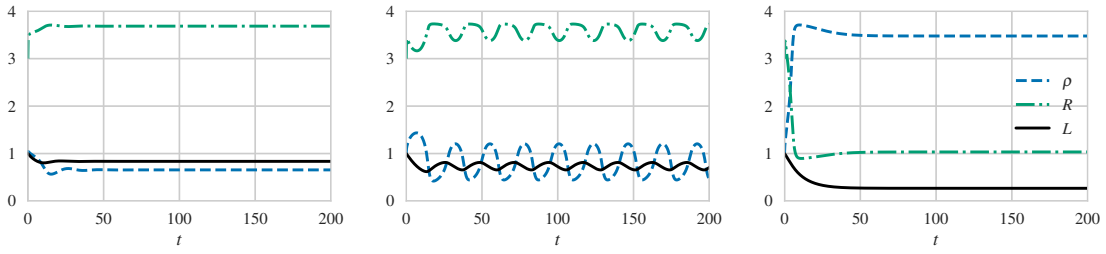

(a) $\gamma_\rho = 10$ (b) $\gamma_\rho = 14$ (c) $\gamma_\rho = 18$

Figure 3.11: Dynamics of the model (3.6) for a single cell with two GTPases ("Rac1" and "RhoA") and feedback from tension to Rho activation. In (a), the feedback from tension ($\gamma_\rho = 10$) is weak, and the cell remains large and relaxed ($L \approx 1$) with high Rac and low Rho activities. In (b), the feedback ($\gamma_\rho = 14$) is of intermediate strength, and limit cycle oscillations arise, provided that the initial conditions send the system to the stable limit cycle, instead of the contracted-cell steady-state (see Figure 3.10). In (c), the coupling is so strong ($\gamma_\rho = 18$) that RhoA activity is always high, Rac is low, and the cell stays in a contracted state ($L \ll 1$). Parameters are as in Figure 3.10.

3.6 Discussion

Feedback between biochemical signalling and mechanical forces plays a vital role in developmental biology and morphogenesis. Given the increasing biological evidence for the role that mechanical forces play in signalling networks, such as GTPases, mathematical and computational approaches are relevant and important to elucidate behaviours and suggest hypotheses. For example, a recent review [27] highlights how diffusion-driven patterns, differential adhesion, buckling instabilities in growing layers, and flows in active materials (cytoskeleton and motor proteins) lead to patterning. Following the experimental work of [35], a single-cell model was also developed to describe the inhibition of cell polarization by membrane tension [98]. The authors used a more sophisticated spatio-temporal model of the GTPases in a 2D cell (based on the idea of wave-pining [54]), its downstream effect on actin, and a cell boundary represented using the phase-field method. The model was able to account for observations on how build-up of tension in a neutrophil (by aspiration into a micropipette) and sudden release of tension (by severing a long cellular protrusion) affect the level and distribution of GTPase activity.

While the effect of tension on GTPase activity was studied previously [30, 35], this is the first model that links GTPase-induced cell contraction to tension-induced GTPase activity in single cells and in a 1D and 2D tissue. Interestingly, a model based on mechanochemical coupling of some (indeterminate) signalling chemical and cell length that was studied mathematically and computationally decades ago [60] bears resemblance to the model presented here. That previous model was aimed at understanding folding and invagination

of epithelia, for example in the process of gastrulation [61, 63]. It was shown then that a localized stimulus in one cell could result in active localized contraction in some neighbourhood, creating the first fold in an early embryo. As GTPases and their effects were yet to be characterized, this early modelling work was theoretical and speculative. Now, such work has additional relevance within the context of mechanical tension and GTPase signalling and illustrated herein. More recently, single and collective cellular oscillations were accounted for by a generic oscillator model for turnover of force-producing material (such as myosin motors) contracting against an elastic element [17]. Similar to the results here, varying the mechanical and kinetic properties of the system can transition the cell behaviour from relaxed cell, to oscillatory, or to contracted cell length and collective cell behaviour from unsynchronized to synchronized oscillations [17].

Through coupling a simple GTPase bistable model without spatially distributed activity within a cell to a simple elastic (Kelvin-Voigt element) cell, I found three distinct regimes of behaviour, including high and low GTPase activity, with coordinated cell tension, and persistent periodic cycling between those states. Here the dynamic pattern of contractile activity stems exclusively from cell size fluctuations, amplified by tension-dependent GTPase activity. I did not include chemical diffusion (each cell is assumed to hold a uniform GTPase level), nor explicit cytoskeletal flows.

Since actual signalling networks are incredibly complex and intricate, it is a significant challenge to understand how cell behaviour can emerge from underlying components and properties. Nonetheless, large networks have been studied theoretically, e.g., by [32, 39, 50]. For example, Boolean models of cell signalling including tens of interacting species have been used to show oscillatory activity of Rac and Rho GTPases [32]. Given this level of detail, it is easy to understand specific biological mechanisms yet difficult to explain the connections between network features and parameters on one hand, and emergent cell behaviour on the other. For this reason, stripped-down conceptual models that concentrate on key topologies and regulators have a role to play in the theoretical understanding of cell behaviour [93]. This principle motivates the analysis of small models for the GTPases.

Assumptions made for the purpose of simplification can be modified substantially without changing the overall conclusions. For example, while our equation for Rho activation resembles that of [30], the authors' assumption about the Hill function-dependence on tension can be modified to another switch-like function that turns on at some critical force magnitude. Furthermore, while there is so far evidence for the multiplicity of GEFs involved in mechanotransduction (relative to GAPs; see [62] Table 1), the model works equally well with GAP-sensitive responses as with the GEF-based GTPase response assumed here.

One of the key findings is that simple coupling between GTPase activity and tension is consistent with a range of biologically-relevant cell behaviour. The simplest model already

produces contracted or relaxed cells as well as cyclic fluctuations between these states. In the Rac-Rho circuit, such dynamic oscillatory regimes can coexist with static steady states in the same parameter range, highlighting the dependence on stimuli and/or initial conditions. Oscillations in cell size are observed under laboratory conditions in epithelial monolayers [103, 104]. While the link between tension and GTPases may be just one factor operating in such systems, the model suggests experiments that could be used to test the connection. In particular, inhibitors of ROCK that would abrogate the connection between RhoA and actomyosin contraction, or of Rac that would inhibit the antagonism of Rac to Rho could be used to test the effect on the presence, frequency, and synchrony of cell volume oscillations.

Hashimoto el al. investigated the "zippering" in the neural/epidermal boundary of the sea squirt (*Ciona intestinalis*) embryo, part of the process that sets up neurulation over a time frame of about 2 hours [29]. Zippering involves successive shortening of cellular junctions, one after the other, in a unidirectional wave of contractions up the zippering axis. The contraction was shown to be powered by the localization of active myosin, along the boundary, and to be dependent on Rho GTPase activity [29]. Furthermore, their paper was accompanied by kinematic simulations that reproduced the sequence of contractions, based on assigned tensions (for pre- and post-contraction cells) and assigned time intervals. Here, I propose a simple model that aims at closing the gap between kinematics and dynamics. Briefly, instead of the manual assignment of forces and time intervals, a closed-loop chemical-mechanical system can give rise to the wave-like pattern of sequential cell contractions. As shown in Figure 3.5(d), under suitable conditions, a unidirectional wave of Rho activation contraction is supported by the minimal model. That said, while the conceptual model here can account for the formation of wave, it is clear that other factors such as communication between cells reaching across the "zipper" sides play vital roles not considered here (Edwin Munro, personal communication).

In other organisms, such as *Drosophila*, Rac GTPase is known to have multiple roles in early morphogenesis [100]. During *Drosophila* dorsal closure, over- and under-expressing Rac results in the excess assembly of lamellipodia or disrupts the assembly of an actin cable (and subsequent zippering) and cell protrusions. While GTPases such as Rac regulate cell behaviour during these morphogenetic processes, it is likely that cell and tissue mechanics also play an important role. Upstream mechanical signalling to Rho GTPases may occur as cells move and forces are transmitted, or as cell-cell junctions are rearranged. In the case of zippering in sea squirt embryos, or in *Drosophila* dorsal closure, further validation of the mechanisms and/or completion of other essential elements remains as a future step. Nonetheless, with these mechanosensing assumptions, it is possible that feedback between signalling and mechanics can account for diverse single and collective cell behaviour in

these morphogenetic processes. Extending the conceptual model here to specific organisms by connecting to GTPase signalling and cell mechanics to data from experiments remains a direction for future work.

I focused on cell size (expanded or contracted), but it is also of interest to consider how cell polarization is affected by mechanical cues in isolated cells and in cell collectives. See [43] for some theoretical background and review. Importantly, the results point to parameter regimes in which cells oscillate between compression and relaxation (in the case of a single Rho-like GTPase), or compression and stretching (for Rac-Rho). But it is known that such cyclic stretching can itself change the properties of cells, reorganizing stress-fibers, for example in a Rho-dependent manner in endothelial cells [38]. It would be of interest to explore such polarity and directionality in future 2D models of this type, as well as to consider how the feedback between GTPases and tension operate in collective cell migration [71]. There is evidence that GTPases also affect the cell-cell adhesion [52, 96] and tight-junctions [105], which would affect the coupling of mechanical transduction between cells in a tissue. This could be of interest in future models.

Chapter 4

Conclusions

Broadly, this thesis has addressed how biological mechanisms combine to organize cell behaviours using models and techniques from applied mathematics. It is possible to gain an understanding of mechanisms, facts and theories about how a host of biological players interact with each other from biological experiments and observations. Building on these observations, multi-scale modelling and analysis can serve as a platform for understanding how cell-scale and tissue-scale organization emerges from the interactions of the many biological players. Along these lines, I have discussed two examples in this thesis. As the first example, I extended asymptotic quasi-steady-state (QSS) reduction methods to a class of nonlinear reaction-advection-diffusion PDE systems satisfying a conservation condition which describe molecular motor transport within cells. As the second example, I developed a model to explore the interplay between GTPase signalling and cell mechanics, which could generate a wide range of single and collective cell behaviour.

In this section, instead of summarizing the results from each part (results are summarized and discussed in sections 2.6 and 3.6, respectively), I will comment on the significance, broader contributions, and future applications of each part.

Intracellular Transport by Molecular Motors

The contribution of the work in Chapter 2 was the extension of existing QSS methods for molecular motor transport to include nonlinear reaction kinetics. These methods were previously limited to models with linear reaction kinetics, but were successfully applied to understand molecular motor based transport in neurons [57] and in fungal hyphae [16]. Here, I have illustrated that even with the incorporation of nonlinear reactions, which may better represent biological interactions, the QSS approximation methodology can serve as a bridge between molecular events, interactions, and motor speeds and the overall transport at the cell scale. Biological insight into the effective transport and effective diffusion rates

is obtained through the QSS methodology. For example, in the kinesin-dynein model, the QSS PDE revealed that changes in any number of parameters could switch the distribution of motors within the cell from one cell end to the other (see Figure 2.9). The biological significance of this finding is that a mutation or other change in one of the biophysical properties of the molecular motors can drastically alter the overall, cell-scale, distribution of motors. Such a mutation would have a detrimental impact on the normal function of the transport process.

The three-case studies illustrated the generality of the QSS approximation method to a variety of nonlinear interactions; however, it remains an open question whether the QSS approximation is possible for more realistic models with a greater number of motor states; or in models with higher degree nonlinearities. Moreover, the QSS approximation relies on the assumption that there is a separation of time-scales between binding/unbinding and motion across the cell.

Recent work by Ciocanel et al. [12] has estimated biophysical motor parameters from active transport data and a PDE approximation method for a system of transport equations with linear reactions. Future work should use data from specific experimental systems to validate the QSS approximation. Although the biological systems considered here are truly three-dimensional (in space), the 1D models considered here are a sufficiently good approximation for fungal hyphae (or neurons) which are long thin cells. Nonetheless, it would be interesting to extend the QSS approximation to higher spatial dimensions with nonlinear reactions (the QSS approximation method has been studied in the context of models in two spatial dimensions with linear reactions [6]). A final interesting direction is the open question of what happens in systems with multiple quasi-steady-states, as in the myosin model in Chapter 2. Of particular interest is a system with three quasi-steady-states in a bistable arrangement (two stable, with an unstable state in between). In such a model, the first questions are to determine which QSS better approximates solutions to the full PDE system, especially if the system is attracted to different QSS in different spatial regions within the cell.

The Interplay Between Cell Signalling and Cell Mechanics

The contribution of the work in Chapter 3 was the first exploration of the interplay between GTPase-induced cell contraction and tension-induced GTPase activity in single cells and in a 1D and 2D tissue. The main biological result is that a wide variety of cell behaviour emerges from this signalling feedback: contracted cells, relaxed cells, oscillatory cells, synchronized contractile tissue, and waves of contraction in a large tissue. This behaviour is consistent with a range of biologically relevant cell behaviours. Although many models have looked at the implications of GTPase signalling for cell behaviour [33, 49] and many others have

sought to understand the implications of mechanochemical interactions for cell behaviours [17, 34, 60], the work here stands as one of the first steps to understanding the interplay between GTPase signalling and cell mechanics within a mathematical model.

The successes of the GTPase-tension modelling work are (1) the emergence of a variety of cell behaviour from the interplay of signalling and mechanics (2) the theoretical understanding possible from the use of a stripped-down, conceptual model and (3) the possible, immediate, extensions to a variety of specific experimental systems such as *Dropsophila* dorsal closure or "zippering" in the neural/epidermal boundary in the *Ciona intestinalis* embryo. The simplicity of the two ODE model allowed for numerical bifurcation analysis to characterize the solutions to the single cell model, but this was limited to the single cell system and could be extended to the multi-cell system. Using the Cellular Potts model (CPM) revealed the implications of 2D neighbour interactions in the GTPase-tension model, but leaves the question of how to translate between a Monte-Carlo step and a unit of time t.

As future work, I can suggest the following projects.

- Extending the specific GTPase-tension system to specific, data-driven, systems (as mentioned above) to explore the interplay between signalling and mechanics in regulating morphogenetic processes.

- Obtaining a continuum limit partial differential equation of the 1D multi-cellular system to understand the transition between synchronization and waves of contraction as a bifurcation in mechanical or signalling parameters (as in [17]).

- Utilizing coarse-graining methods to derive partial differential equation models that approximate the behaviour of the 2D CPM. This could provide a link to the subcellular signalling and the population-level outcomes. For example, Alber et al. [1], Lushnikov et al. [45], Turner et al. [94] have used coarse-graining methods to derive PDE descriptions of cell behaviour from cellular Potts models of cell migration, cell adhesion and chemotaxis. In these examples, numerical simulations of the PDE model match the CPM simulations, and the coefficients of the PDE are derived from the CPM parameters.

- Determining how cell polarity and directionality in 2D cell migration models are affected by mechanical signalling and GTPase signalling.

Multi-scale Modelling in Cell Biology

Upon reflecting on the conclusions, significance, and contribution of the results in thesis, it is evident that multi-scale mathematical modelling is useful for explaining qualitative behaviour and suggesting plausible hypotheses for experimentally observed phenomena. To

illustrate, consider the following examples. First, from the QSS methods in Chapter 2, the effective transport and effective diffusion rates were found to depend on the biophysical properties of the molecular motors. In an experiment where the overall, cell-scale, distribution of motors or cargo is observed the quantitative measures would describe the effective transport and diffusion rates instead of specific molecular motor behaviours. From such data (and further experiments to alter or inhibit different players in the transport process) it would be possible to obtain a realistic biophysical understanding of the motors and interactions that control transport. Second, a result from Chapter 3 is the emergence of oscillations of cell size in a large epithelial tissue. Such oscillations are also observed in epithelial monolayers [103, 104]. Experimental manipulations to increase or decrease the adhesions of cells (through drugs that target integrins, focal adhesions, or other cell-cell junctions, for example) and quantitative analysis of the resulting behaviour could test the hypothesis that increasing adhesion leads to increased synchronization within the monolayer.

Nonetheless, conceptual multi-scale models such as those in this thesis can have limitations. A few limitations of the work here are the (1) lack of connections to specific experimental data, (2) the usage of deterministic models, (3) over-simplification of cell signalling, (4) assuming that cells are homogenous internally, and (5) the myriad of other biological factors that I have ignored. When coupled to data, model parameters can be estimated, models can test hypotheses and suggest new experiments (as suggested above). Noise, which is inherent to may biophysical systems, has largely been ignored in this thesis. Although the reaction-advection-diffusion PDE systems studied in Chapter 2 can be understood as averages or approximations of the noisy agent-based behaviour of many molecular motors, and the Cellular Potts model (CPM) revealed additional single cell behaviour (stochastic switching between steady-states) in Chapter 3, a more careful treatment of the noisy biological processes may be helpful in a more mechanistic modelling approach.

Even with the simplifications, assumptions, and limitations of the specific models, it is apparent that a wide variety of organization can be understood from interactions at different levels. In Chapter 2, I illustrated how, from sub-cellular interactions, quasi-steady-state methods can serve as a tool understand cell-scale distribution of molecular motors and the effects that particular biophysical parameters have on the resulting motor distributions. In Chapter 3, I connected signalling and mechanics at the cell scale to generate and understand cellular and multi-cellular behaviours.

Bibliography

[1] M. Alber, N. Chen, P. M. Lushnikov, and S. A. Newman. Continuous macroscopic limit of a discrete stochastic model for interaction of living cells. *Physical Review Letters*, 99(16), Oct 2007. doi:10.1103/physrevlett.99.168102. → page 95

[2] P. W. Baas, J. S. Deitch, M. M. Black, and G. A. Banker. Polarity orientation of microtubules in hippocampal neurons: uniformity in the axon and nonuniformity in the dendrite. *Proceedings of the National Academy of Sciences*, 85(21):8335–8339, Nov 1988. doi:10.1073/pnas.85.21.8335. → page 18

[3] C. Bakal, J. Aach, G. Church, and N. Perrimon. Quantitative morphological signatures define local signaling networks regulating cell morphology. *Science*, 316 (5832):1753–1756, Jun 2007. doi:10.1126/science.1140324. → pages 8, 9, 70

[4] D. Bhat and M. Gopalakrishnan. Effectiveness of a dynein team in a tug of war helped by reduced load sensitivity of detachment: evidence from the study of bidirectional endosome transport ind. discoideum. *Physical Biology*, 9(4):046003, Jun 2012. doi:10.1088/1478-3975/9/4/046003. → pages 2, 18

[5] T. L. Blasius, N. Reed, B. M. Slepchenko, and K. J. Verhey. Recycling of kinesin-1 motors by diffusion after transport. *PLoS ONE*, 8(9):e76081, Sep 2013. doi:10.1371/journal.pone.0076081. → pages 2, 17

[6] P. C. Bressloff and J. M. Newby. Quasi-steady-state analysis of two-dimensional random intermittent search processes. *Physical Review E*, 83(6), Jun 2011. doi:10.1103/physreve.83.061139. → pages 67, 94

[7] P. C. Bressloff and J. M. Newby. Stochastic models of intracellular transport. *Reviews of Modern Physics*, 85(1):135–196, Jan 2013. doi:10.1103/revmodphys.85.135. → pages 2, 18, 22, 27, 64

[8] P. R. Burton. Dendrites of mitral cell neurons contain microtubules of opposite polarity. *Brain Research*, 473(1):107–115, Nov 1988. doi:10.1016/0006-8993(88)90321-6. → page 18

[9] K. M. Byrne, N. Monsefi, J. C. Dawson, A. Degasperi, J.-C. Bukowski-Wills, N. Volinsky, M. Dobrzyński, M. R. Birtwistle, M. A. Tsyganov, A. Kiyatkin, and et al. Bistability in the Rac1, PAK, and RhoA signaling network drives actin cytoskeleton dynamics and cell motility switches. *Cell Systems*, 2(1):38–48, Jan 2016. doi:10.1016/j.cels.2016.01.003. → pages 9, 70, 71, 84

[10] D. Chowdhury, A. Schadschneider, and K. Nishinari. Traffic Phenomena in Biology: From Molecular Motors to Organisms. *Traffic Granul. Flow*, 2(4):223–238, 2005. → pages 2, 17

[11] L. Ciandrini, M. C. Romano, and A. Parmeggiani. Stepping and crowding of molecular motors: Statistical kinetics from an exclusion process perspective. *Biophysical Journal*, 107(5):1176–1184, Sep 2014. doi:10.1016/j.bpj.2014.07.012. → pages 2, 18

[12] M.-V. Ciocanel, J. A. Kreiling, J. A. Gagnon, K. L. Mowry, and B. Sandstede. Analysis of active transport by fluorescence recovery after photobleaching. *Biophysical Journal*, 112(8):1714–1725, Apr 2017. doi:10.1016/j.bpj.2017.02.042. → page 94

[13] R. Clewley, W. Sherwood, M. LaMar, and J. Guckenheimer. PyDSTool, a software environment for dynamical systems modeling, 2007. → page 118

[14] S. Cooper, A. Sadok, V. Bousgouni, and C. Bakal. Apolar and polar transitions drive the conversion between amoeboid and mesenchymal shapes in melanoma cells. *Molecular Biology of the Cell*, 26(22):4163–4170, Aug 2015. doi:10.1091/mbc.e15-06-0382. → pages 8, 9, 70

[15] T. Das, K. Safferling, S. Rausch, N. Grabe, H. Boehm, and J. P. Spatz. A molecular mechanotransduction pathway regulates collective migration of epithelial cells. *Nature Cell Biology*, 17(3):276–287, Feb 2015. doi:10.1038/ncb3115. → pages 8, 69

[16] D. Dauvergne and L. Edelstein-Keshet. Application of quasi-steady state methods to molecular motor transport on microtubules in fungal hyphae. *Journal of Theoretical Biology*, 379:47–58, Aug 2015. doi:10.1016/j.jtbi.2015.04.033. → pages 2, 3, 18, 19, 22, 30, 35, 36, 37, 39, 64, 65, 93

[17] K. Dierkes, A. Sumi, J. Solon, and G. Salbreux. Spontaneous oscillations of elastic contractile materials with turnover. *Physical Review Letters*, 113(14):10, Oct 2014. doi:10.1103/physrevlett.113.148102. → pages 90, 95

[18] D. E. Discher. Tissue cells feel and respond to the stiffness of their substrate. *Science*, 310(5751):1139–1143, Nov 2005. doi:10.1126/science.1116995. → pages 8, 68

[19] R. Dixit, J. L. Ross, Y. E. Goldman, and E. L. F. Holzbaur. Differential regulation of dynein and kinesin motor proteins by tau. *Science*, 319(5866):1086–1089, Feb 2008. doi:10.1126/science.1152993. → page 19

[20] A. Diz-Muñoz, D. A. Fletcher, and O. D. Weiner. Use the force: membrane tension as an organizer of cell shape and motility. *Trends in Cell Biology*, 23(2):47–53, Feb 2013. doi:10.1016/j.tcb.2012.09.006. → page 69

[21] A. Diz-Muñoz, K. Thurley, S. Chintamen, S. J. Altschuler, L. F. Wu, D. A. Fletcher, and O. D. Weiner. Membrane tension acts through PLD2 and mTORC2 to limit actin network assembly during neutrophil migration. *PLOS Biology*, 14(6):e1002474, Jun 2016. doi:10.1371/journal.pbio.1002474. → page 69

[22] L. Edelstein-Keshet. *Mathematical Models in Biology*. Society for Industrial and Applied Mathematics, Jan 2005. doi:10.1137/1.9780898719147. → page 5

[23] G. Fink. Dynein-dependent motility of microtubules and nucleation sites supports polarization of the tubulin array in the fungus Ustilago maydis. *Molecular Biology of the Cell*, 17(7):3242–3253, Apr 2006. doi:10.1091/mbc.e05-12-1118. → page 18

[24] S. A. Freeman, S. Christian, P. Austin, I. Iu, M. L. Graves, L. Huang, S. Tang, D. Coombs, M. R. Gold, and C. D. Roskelley. Applied stretch initiates directional invasion through the action of Rap1 GTPase as a tension sensor. *Journal of Cell Science*, 130(1):152–163, May 2017. doi:10.1242/jcs.180612. → page 69

[25] M. Fukata, M. Nakagawa, and K. Kaibuchi. Roles of Rho-family GTPases in cell polarisation and directional migration. *Current Opinion in Cell Biology*, 15(5): 590–597, 2003. doi:10.1016/S0955-0674(03)00097-8. → pages 8, 68

[26] J. Gou, L. Edelstein-Keshet, and J. Allard. Mathematical model with spatially uniform regulation explains long-range bidirectional transport of early endosomes in fungal hyphae. *Molecular Biology of the Cell*, 25(16):2408–2415, Jun 2014. doi:10.1091/mbc.e14-03-0826. → pages 2, 18, 22, 39

[27] P. Gross, K. V. Kumar, and S. W. Grill. How active mechanics and regulatory biochemistry combine to form patterns in development. *Annual Review of Biophysics*, 46(1):337–356, May 2017. doi:10.1146/annurev-biophys-070816-033602. → page 89

[28] C. Guilluy, R. Garcia-Mata, and K. Burridge. Rho protein crosstalk: another social network? *Trends in Cell Biology*, 21(12):718–726, Dec 2011. doi:10.1016/j.tcb.2011.08.002. → page 71

[29] H. Hashimoto, F. B. Robin, K. M. Sherrard, and E. M. Munro. Sequential contraction and exchange of apical junctions drives zippering and neural tube closure in a simple chordate. *Developmental Cell*, 32(2):241–255, Jan 2015. doi:10.1016/j.devcel.2014.12.017. → pages 77, 91

[30] L. He, J. Tao, D. Maity, F. Si, Y. Wu, T. Wu, V. Prasath, D. Wirtz, and S. X. Sun. Role of membrane-tension gated Ca2+ flux in cell mechanosensation. *Journal of Cell Science*, 131(4):jcs208470, Jan 2018. doi:10.1242/jcs.208470. → pages 69, 73, 89, 90

[31] A. G. Hendricks, E. Perlson, J. L. Ross, H. W. Schroeder, M. Tokito, and E. L. Holzbaur. Motor coordination via a tug-of-war mechanism drives bidirectional vesicle transport. *Current Biology*, 20(8):697–702, Apr 2010. doi:10.1016/j.cub.2010.02.058. → pages 2, 18

[32] J. H. R. Hetmanski, E. Zindy, J.-M. Schwartz, and P. T. Caswell. A MAPK-driven feedback loop suppresses Rac activity to promote RhoA-driven cancer cell invasion. *PLOS Computational Biology*, 12(5):e1004909, May 2016. doi:10.1371/journal.pcbi.1004909. → page 90

[33] W. R. Holmes and L. Edelstein-Keshet. Analysis of a minimal Rho-GTPase circuit regulating cell shape. *Physical Biology*, 13(4):046001, Jul 2016. doi:10.1088/1478-3975/13/4/046001. → pages 9, 11, 71, 72, 74, 84, 94, 120

[34] W. R. Holmes, J. Park, A. Levchenko, and L. Edelstein-Keshet. A mathematical model coupling polarity signaling to cell adhesion explains diverse cell migration patterns. *PLOS Computational Biology*, 13(5):e1005524, May 2017. doi:10.1371/journal.pcbi.1005524. → pages 9, 11, 69, 70, 71, 74, 84, 95, 120

[35] A. R. Houk, A. Jilkine, C. O. Mejean, R. Boltyanskiy, E. R. Dufresne, S. B. Angenent, S. J. Altschuler, L. F. Wu, and O. D. Weiner. Membrane tension maintains cell polarity by confining signals to the leading edge during neutrophil migration. *Cell*, 148(1-2):175–188, Jan 2012. doi:10.1016/j.cell.2011.10.050. → pages 8, 69, 89

[36] A. Jilkine, A. F. M. Marée, and L. Edelstein-Keshet. Mathematical model for spatial segregation of the Rho-family GTPases based on inhibitory crosstalk. *Bulletin of Mathematical Biology*, 69(6):1943–1978, 2007. doi:10.1007/s11538-007-9200-6. → page 72

[37] A. Katsumi, J. Milanini, W. B. Kiosses, M. A. del Pozo, R. Kaunas, S. Chien, K. M. Hahn, and M. A. Schwartz. Effects of cell tension on the small GTPase Rac. *The Journal of Cell Biology*, 158(1):153–164, Jul 2002. doi:10.1083/jcb.200201105. → pages 8, 69

[38] R. Kaunas, P. Nguyen, S. Usami, and S. Chien. From the cover: Cooperative effects of Rho and mechanical stretch on stress fiber organization. *Proceedings of the National Academy of Sciences*, 102(44):15895–15900, Oct 2005. doi:10.1073/pnas.0506041102. → page 92

[39] T.-H. Kim, N. Monsefi, J.-H. Song, A. von Kriegsheim, D. Vandamme, O. Pertz, B. N. Kholodenko, W. Kolch, and K.-H. Cho. Network-based identification of feedback modules that control RhoA activity and cell migration. *Journal of Molecular Cell Biology*, 7(3):242–252, Mar 2015. doi:10.1093/jmcb/mjv017. → page 90

[40] S. Klumpp and R. Lipowsky. Cooperative cargo transport by several molecular motors. *Proceedings of the National Academy of Sciences*, 102(48):17284–17289, Nov 2005. doi:10.1073/pnas.0507363102. → pages 2, 18

[41] A. Kumar, M. Ouyang, K. Van den Dries, E. J. McGhee, K. Tanaka, M. D. Anderson, A. Groisman, B. T. Goult, K. I. Anderson, and M. A. Schwartz. Talin tension sensor reveals novel features of focal adhesion force transmission and mechanosensitivity. *The Journal of Cell Biology*, 213(3):371–383, May 2016. doi:10.1083/jcb.201510012. → page 69

[42] Y. Kuramoto. *Chemical Oscillations, Waves, and Turbulence*, volume 19. Springer Berlin Heidelberg, 1984. doi:10.1007/978-3-642-69689-3. → pages 82, 122

[43] B. Ladoux, R.-M. Mège, and X. Trepat. Front–rear polarization by mechanical cues: From single cells to tissues. *Trends in Cell Biology*, 26(6):420–433, Jun 2016. doi:10.1016/j.tcb.2016.02.002. → page 92

[44] C. Leduc, K. Padberg-Gehle, V. Varga, D. Helbing, S. Diez, and J. Howard. Molecular crowding creates traffic jams of kinesin motors on microtubules. *Proceedings of the National Academy of Sciences*, 109(16):6100–6105, Mar 2012. doi:10.1073/pnas.1107281109. → page 19

[45] P. M. Lushnikov, N. Chen, and M. Alber. Macroscopic dynamics of biological cells interacting via chemotaxis and direct contact. *Physical Review E*, 78(6), Dec 2008. doi:10.1103/physreve.78.061904. → page 95

[46] M. Machacek, L. Hodgson, C. Welch, H. Elliott, O. Pertz, P. Nalbant, A. Abell, G. L. Johnson, K. M. Hahn, and G. Danuser. Coordination of Rho GTPase activities during cell protrusion. *Nature*, 461(7260):99–103, Aug 2009. doi:10.1038/nature08242. → page 71

[47] R. Magno, V. A. Grieneisen, and A. F. Marée. The biophysical nature of cells: potential cell behaviours revealed by analytical and computational studies of cell surface mechanics. *BMC Biophysics*, 8(1):8, May 2015. doi:10.1186/s13628-015-0022-x. → pages 79, 121

[48] R. Mallik, A. K. Rai, P. Barak, A. Rai, and A. Kunwar. Teamwork in microtubule motors. *Trends in Cell Biology*, 23(11):575–582, Nov 2013. doi:10.1016/j.tcb.2013.06.003. → pages 2, 18

[49] A. F. M. Marée, A. Jilkine, A. Dawes, V. A. Grieneisen, and L. Edelstein-Keshet. Polarization and movement of keratocytes: A multiscale modelling approach. *Bulletin of Mathematical Biology*, 68(5):1169–1211, Jun 2006. doi:10.1007/s11538-006-9131-7. → pages 5, 71, 94

[50] A. F. M. Marée, V. A. Grieneisen, and L. Edelstein-Keshet. How cells integrate complex stimuli: The effect of feedback from phosphoinositides and cell shape on cell polarization and motility. *PLoS Computational Biology*, 8(3):e1002402, Mar 2012. doi:10.1371/journal.pcbi.1002402. → page 90

[51] P. K. Mattila and P. Lappalainen. Filopodia: molecular architecture and cellular functions. *Nature Reviews Molecular Cell Biology*, 9(6):446–454, May 2008. doi:10.1038/nrm2406. → page 26

[52] J. McCormack, N. J. Welsh, and V. M. M. Braga. Cycling around cell-cell adhesion with Rho GTPase regulators. *Journal of Cell Science*, 126(2):379–391, Jan 2013. doi:10.1242/jcs.097923. → page 92

[53] D. P. McVicker, L. R. Chrin, and C. L. Berger. The nucleotide-binding state of microtubules modulates kinesin processivity and the ability of tau to inhibit kinesin-mediated transport. *Journal of Biological Chemistry*, 286(50):42873–42880, Oct 2011. doi:10.1074/jbc.m111.292987. → page 19

[54] Y. Mori, A. Jilkine, and L. Edelstein-Keshet. Wave-pinning and cell polarity from a bistable reaction-diffusion system. *Biophysical Journal*, 94(9):3684–3697, May 2008. doi:10.1529/biophysj.107.120824. → pages 8, 9, 11, 68, 72, 89

[55] M. J. I. Müller, S. Klumpp, and R. Lipowsky. Motility states of molecular motors engaged in a stochastic tug-of-war. *Journal of Statistical Physics*, 133(6):1059–1081, Dec 2008. doi:10.1007/s10955-008-9651-7. → pages 2, 18

[56] R. Nambiar, R. E. McConnell, and M. J. Tyska. Myosin motor function: the ins and outs of actin-based membrane protrusions. *Cellular and Molecular Life Sciences*, 67 (8):1239–1254, Jan 2010. doi:10.1007/s00018-009-0254-5. → page 26

[57] J. Newby and P. C. Bressloff. Local synaptic signaling enhances the stochastic transport of motor-driven cargo in neurons. *Physical Biology*, 7(3):036004, Aug 2010. doi:10.1088/1478-3975/7/3/036004. → pages 18, 19, 22, 30, 63, 64, 93

[58] J. M. Newby and P. C. Bressloff. Quasi-steady state reduction of molecular motor-based models of directed intermittent search. *Bulletin of Mathematical Biology*, 72(7):1840–1866, Feb 2010. doi:10.1007/s11538-010-9513-8. → pages 2, 3, 65

[59] C. D. Nobes and A. Hall. Rho GTPases control polarity, protrusion, and adhesion during cell movement. *The Journal of Cell Biology*, 144(6):1235–1244, Mar 1999. doi:10.1083/jcb.144.6.1235. → pages 8, 68

[60] G. Odell, G. Oster, B. Burnside, and P. Alberch. A mechanical model for epithelial morphogenesis. *Journal of Mathematical Biology*, 9(3):291–295, May 1980. doi:10.1007/bf00276030. → pages ix, 9, 10, 11, 12, 13, 14, 69, 89, 95

[61] G. Odell, G. Oster, P. Alberch, and B. Burnside. The mechanical basis of morphogenesis. *Developmental Biology*, 85(2):446–462, Jul 1981. doi:10.1016/0012-1606(81)90276-1. → pages 9, 69, 77, 90

[62] K. Ohashi, S. Fujiwara, and K. Mizuno. Roles of the cytoskeleton, cell adhesion and Rho signalling in mechanosensing and mechanotransduction. *Journal of Biochemistry*, 161(3):mvw082, Jan 2017. doi:10.1093/jb/mvw082. → pages 8, 69, 72, 90

[63] G. F. Oster, J. D. Murray, and A. K. Harris. Mechanical aspects of mesenchymal morphogenesis. *Development*, 78:83–125, 1983. → pages 9, 69, 90

[64] M. Otsuji, S. Ishihara, C. Co, K. Kaibuchi, A. Mochizuki, and S. Kuroda. A mass conserved reaction–diffusion system captures properties of cell polarity. *PLoS Computational Biology*, 3(6):e108, 2007. doi:10.1371/journal.pcbi.0030108. → pages 8, 68

[65] J. Park, W. R. Holmes, S. H. Lee, H.-N. Kim, D.-H. Kim, M. K. Kwak, C. J. Wang, L. Edelstein-Keshet, and A. Levchenko. Mechanochemical feedback underlies coexistence of qualitatively distinct cell polarity patterns within diverse cell populations. *Proceedings of the National Academy of Sciences*, 114(28): E5750–E5759, Jun 2017. doi:10.1073/pnas.1700054114. → pages 9, 69, 70, 71

[66] A. Parmeggiani, T. Franosch, and E. Frey. Totally asymmetric simple exclusion process with langmuir kinetics. *Physical Review E*, 70(4), Oct 2004. doi:10.1103/physreve.70.046101. → pages 2, 18

[67] M. Parri and P. Chiarugi. Rac and Rho GTPases in cancer cell motility control. *Cell Communication and Signaling*, 8(1):23, 2010. doi:10.1186/1478-811x-8-23. → pages 71, 84

[68] O. Pertz. Designing biosensors for Rho family proteins – deciphering the dynamics of rho family gtpase activation in living cells. *Journal of Cell Science*, 117(8): 1313–1318, Mar 2004. doi:10.1242/jcs.01117. → page 69

[69] M. Pines, R. Das, S. J. Ellis, A. Morin, S. Czerniecki, L. Yuan, M. Klose, D. Coombs, and G. Tanentzapf. Mechanical force regulates integrin turnover in drosophila in vivo. *Nature Cell Biology*, 14(9):935–943, Aug 2012. doi:10.1038/ncb2555. → page 69

[70] N. A. Reed, D. Cai, T. L. Blasius, G. T. Jih, E. Meyhofer, J. Gaertig, and K. J. Verhey. Microtubule acetylation promotes kinesin-1 binding and transport. *Current Biology*, 16(21):2166–2172, Nov 2006. doi:10.1016/j.cub.2006.09.014. → page 19

[71] M. Reffay, M. C. Parrini, O. Cochet-Escartin, B. Ladoux, A. Buguin, S. Coscoy, F. Amblard, J. Camonis, and P. Silberzan. Interplay of RhoA and mechanical forces in collective cell migration driven by leader cells. *Nature Cell Biology*, 16(3): 217–223, Feb 2014. doi:10.1038/ncb2917. → page 92

[72] T. Reichenbach, E. Frey, and T. Franosch. Traffic jams induced by rare switching events in two-lane transport. *New Journal of Physics*, 9(6):159–159, Jun 2007. doi:10.1088/1367-2630/9/6/159. → pages 2, 18

[73] A. J. Ridley. Rho family proteins: coordinating cell responses. *Trends in Cell Biology*, 11(12):471–477, 2001. doi:10.1016/S0962-8924(01)02153-5. → pages 8, 68

[74] A. J. Ridley. Rho GTPase signalling in cell migration. *Current Opinion in Cell Biology*, 36:103–112, Oct 2015. doi:10.1016/j.ceb.2015.08.005. → pages 8, 68

[75] K. Rottner, A. Hall, and J. Small. Interplay between Rac and Rho in the control of substrate contact dynamics in the control of substrate contact dynamics. *Current Biology*, 9(12):640–S1, Jun 1999. doi:10.1016/s0960-9822(99)80286-3. → page 71

[76] A. K. Rzadzinska, M. E. Schneider, C. Davies, G. P. Riordan, and B. Kachar. An actin molecular treadmill and myosins maintain stereocilia functional architecture and self-renewal. *The Journal of Cell Biology*, 164(6):887–897, Mar 2004. doi:10.1083/jcb.200310055. → page 26

[77] B. Sabass, M. L. Gardel, C. M. Waterman, and U. S. Schwarz. High resolution traction force microscopy based on experimental and computational advances. *Biophysical Journal*, 94(1):207–220, Jan 2008. doi:10.1529/biophysj.107.113670. → page 69

[78] H. Sailem, V. Bousgouni, S. Cooper, and C. Bakal. Cross-talk between Rho and Rac GTPases drives deterministic exploration of cellular shape space and morphological heterogeneity. *Open Biology*, 4(1):130132–130132, Jan 2014. doi:10.1098/rsob.130132. → pages 8, 9, 70, 71, 84

[79] M. E. Schneider, A. C. Dose, F. T. Salles, W. Chang, F. L. Erickson, B. Burnside, and B. Kachar. A new compartment at stereocilia tips defined by spatial and temporal patterns of myosin IIIa expression. *Journal of Neuroscience*, 26(40): 10243–10252, Oct 2006. doi:10.1523/jneurosci.2812-06.2006. → page 19

[80] M. Schuster, S. Kilaru, G. Fink, J. Collemare, Y. Roger, and G. Steinberg. Kinesin-3 and dynein cooperate in long-range retrograde endosome motility along a nonuniform microtubule array. *Molecular Biology of the Cell*, 22(19):3645–3657, Aug 2011. doi:10.1091/mbc.e11-03-0217. → page 18

[81] M. Schuster, R. Lipowsky, M.-A. Assmann, P. Lenz, and G. Steinberg. Transient binding of dynein controls bidirectional long-range motility of early endosomes. *Proceedings of the National Academy of Sciences*, 108(9):3618–3623, Feb 2011. doi:10.1073/pnas.1015839108. → pages 18, 22, 24

[82] M. Schwander, B. Kachar, and U. Müller. The cell biology of hearing. *The Journal of Cell Biology*, 190(1):9–20, Jul 2010. doi:10.1083/jcb.201001138. → page 26

[83] L. A. Segel and M. Slemrod. The quasi-steady-state assumption: A case study in perturbation. *SIAM Review*, 31(3):446–477, Sep 1989. doi:10.1137/1031091. → page 5

[84] G. Shubeita and S. Gross. Intracellular transport: Relating single-molecule properties to in vivo function. *Comprehensive Biophysics*, 4:287–297, 2012. doi:10.1016/b978-0-12-374920-8.00418-5. → page 18

[85] D. Smith and R. Simmons. Models of motor-assisted transport of intracellular particles. *Biophysical Journal*, 80(1):45–68, Jan 2001. doi:10.1016/s0006-3495(01)75994-2. → pages 2, 18

[86] G. Steinberg. Motors in fungal morphogenesis: cooperation versus competition. *Current Opinion in Microbiology*, 14(6):660–667, Dec 2011. doi:10.1016/j.mib.2011.09.013. → pages 2, 18, 22

[87] G. Steinberg, R. Wedlich-Soldner, M. Brill, and I. Schulz. Microtubules in the fungal pathogen Ustilago maydis are highly dynamic and determine cell polarity. *Journal of Cell Science*, 114(3):609–622, 2001. → page 18

[88] M. C. Stone, F. Roegiers, and M. M. Rolls. Microtubules have opposite orientation in axons and dendrites of drosophila neurons. *Molecular Biology of the Cell*, 19(10): 4122–4129, Jul 2008. doi:10.1091/mbc.e07-10-1079. → page 18

[89] S. H. Strogatz. From Kuramoto to Crawford: exploring the onset of synchronization in populations of coupled oscillators. *Physica D: Nonlinear Phenomena*, 143(1-4): 1–20, Sep 2000. doi:10.1016/s0167-2789(00)00094-4. → pages 82, 122

[90] M. H. Swat, G. L. Thomas, J. M. Belmonte, A. Shirinifard, D. Hmeljak, and J. A. Glazier. *Multi-Scale Modeling of Tissues Using CompuCell3D*, chapter Multi-Scale Modeling of Tissues Using CompuCell3D, pages 325–366. Elsevier, 2012. doi:10.1016/b978-0-12-388403-9.00013-8. → pages 15, 79, 81, 85, 118, 120

[91] A. Tomar and D. D. Schlaepfer. Focal adhesion kinase: switching between GAPs and GEFs in the regulation of cell motility. *Current Opinion in Cell Biology*, 21(5): 676–683, Oct 2009. doi:10.1016/j.ceb.2009.05.006. → page 69

[92] K. Tsujita, T. Takenawa, and T. Itoh. Feedback regulation between plasma membrane tension and membrane-bending proteins organizes cell polarity during leading edge formation. *Nature Cell Biology*, 17(6):749–758, May 2015. doi:10.1038/ncb3162. → page 69

[93] M. A. Tsyganov, W. Kolch, and B. N. Kholodenko. The topology design principles that determine the spatiotemporal dynamics of G-protein cascades. *Molecular BioSystems*, 8(3):730, 2012. doi:10.1039/c2mb05375f. → page 90

[94] S. Turner, J. A. Sherratt, K. J. Painter, and N. J. Savill. From a discrete to a continuous model of biological cell movement. *Physical Review E*, 69(2), Feb 2004. doi:10.1103/physreve.69.021910. → page 95

[95] A. Van Keymeulen, K. Wong, Z. A. Knight, C. Govaerts, K. M. Hahn, K. M. Shokat, and H. R. Bourne. To stabilize neutrophil polarity, PIP3 and Cdc42 augment RhoA activity at the back as well as signals at the front. *The Journal of Cell Biology*, 174(3):437–445, Jul 2006. doi:10.1083/jcb.200604113. → pages 8, 68

[96] F. M. Vega, M. Thomas, N. Reymond, and A. J. Ridley. The Rho GTPase RhoB regulates cadherin expression and epithelial cell-cell interaction. *Cell Communication and Signaling*, 13(1):6, 2015. doi:10.1186/s12964-015-0085-y. → page 92

[97] V. Vogel and M. Sheetz. Local force and geometry sensing regulate cell functions. *Nature Reviews Molecular Cell Biology*, 7(4):265–275, Feb 2006. doi:10.1038/nrm1890. → pages 8, 68, 69

[98] W. Wang, K. Tao, J. Wang, G. Yang, Q. Ouyang, Y. Wang, L. Zhang, and F. Liu. Exploring the inhibitory effect of membrane tension on cell polarization. *PLOS Computational Biology*, 13(1):e1005354, Jan 2017. doi:10.1371/journal.pcbi.1005354. → page 89

[99] K. Wong, O. Pertz, K. Hahn, and H. Bourne. Neutrophil polarization: Spatiotemporal dynamics of RhoA activity support a self-organizing mechanism. *Proceedings of the National Academy of Sciences*, 103(10):3639–3644, Feb 2006. doi:10.1073/pnas.0600092103. → pages 8, 68

[100] S. Woolner, A. Jacinto, and P. Martin. The small GTPase Rac plays multiple roles in epithelial sheet fusion—dynamic studies of Drosophila dorsal closure. *Developmental Biology*, 282(1):163–173, Jun 2005. doi:10.1016/j.ydbio.2005.03.005. → page 91

[101] A. Yochelis, S. Ebrahim, B. Millis, R. Cui, B. Kachar, M. Naoz, and N. S. Gov. Self-organization of waves and pulse trains by molecular motors in cellular protrusions. *Scientific Reports*, 5(1), Sep 2015. doi:10.1038/srep13521. → pages 2, 24, 26, 27, 66

[102] A. Yochelis, T. Bar-On, and N. S. Gov. Reaction–diffusion–advection approach to spatially localized treadmilling aggregates of molecular motors. *Physica D: Nonlinear Phenomena*, 318-319:84–90, Apr 2016. doi:10.1016/j.physd.2015.10.023. → pages 3, 24, 26, 27, 52, 66

[103] S. M. Zehnder, M. Suaris, M. M. Bellaire, and T. E. Angelini. Cell volume fluctuations in MDCK monolayers. *Biophysical Journal*, 108(2):247–250, Jan 2015. doi:10.1016/j.bpj.2014.11.1856. → pages 91, 96

[104] S. M. Zehnder, M. K. Wiatt, J. M. Uruena, A. C. Dunn, W. G. Sawyer, and T. E. Angelini. Multicellular density fluctuations in epithelial monolayers. *Physical Review E*, 92(3):1–8, Sep 2015. doi:10.1103/physreve.92.032729. → pages 91, 96

[105] C. Zihni and S. J. Terry. RhoGTPase signalling at epithelial tight junctions: Bridging the GAP between polarity and cancer. *The International Journal of Biochemistry & Cell Biology*, 64:120–125, Jul 2015. doi:10.1016/j.biocel.2015.02.020. → page 92

[106] C. Zmurchok, T. Small, M. J. Ward, and L. Edelstein-Keshet. Application of quasi-steady-state methods to nonlinear models of intracellular transport by molecular motors. *Bulletin of Mathematical Biology*, 79(9):1923–1978, Jul 2017. doi:10.1007/s11538-017-0314-1. → page v

[107] C. Zmurchok, D. Bhaskar, and L. Edelstein-Keshet. Coupling mechanical tension and GTPase signaling to generate cell and tissue dynamics. *Physical Biology*, Feb 2018. doi:10.1088/1478-3975/aab1c0. → page v

Appendix A

Supporting Materials for the Application of Quasi-Steady-State Methods to Nonlinear Models of Intracellular Transport

A.1 Convergence of the Kinesin Model to the QSS for $\varepsilon \to 0$

As discussed in §2.6, one advantage of the QSS methodology is that it is not necessary to perform the possibly numerically expensive task of computing time-dependent or steady-state solutions to the full PDE system for each small value of the parameter ε. Computational savings would be amplified if the methodology was extended to 2 or 3 dimensions or the methodology was required in an experimental context or being fit to data. Since numerical computations for the full models and the QSS PDEs herein require approximately the same amount of computational time, there is hardly a computational advantage to using the QSS PDE as a proxy for the full model. Nonetheless, repeated time-dependent numerical simulations of the regularized myosin model for the creation of Figure 2.17 did require a significant amount of computational time. The need for repeated numerical simulations for different initial conditions or for different parameters is suggestive of the computational advantages of the QSS approximation.

Using the QSS as a proxy for the full PDE system does incur errors that depend on the size of ε. To illustrate this, I compare the steady-state solution of the QSS PDE (2.29) and (2.30) with corresponding steady-state results computed from the full model (2.15) with (2.25) for a few values of ε in Figure A.1. These results show that as ε decreases the QSS PDE accurately predicts the steady-state of the full model.

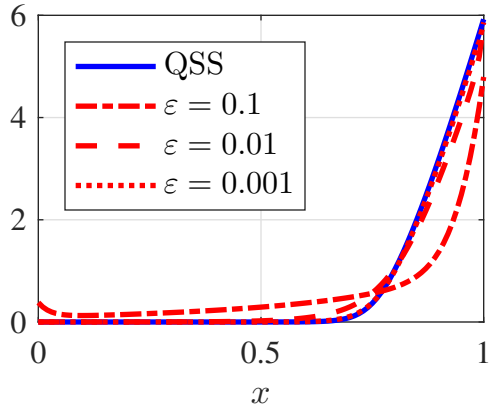

Figure A.1: The steady-state solution to the full nonlinear model (2.15) with (2.25) converges to the steady-state of the QSS PDE (2.29) with (2.30) as $\varepsilon \to 0$. Here $g(\alpha) = \alpha/(1+\alpha)$, $P = 0.6$, $k_\mathrm{b} = 0.5$, $k_\mathrm{u} = 0.3$, and $D = 0.01$.

A.2 Numerical Methods for the QSS

In this appendix, I show how to numerically compute the steady-state solution of the QSS PDEs by recasting the nonlocal problem into an initial-boundary value problem (IBVP), which is amenable to a numerical shooting method.

For the QSS PDE associated with the **kinesin model** (2.29) of §2.4.1, the steady-state problem is

$$\frac{d\alpha}{dx} = \frac{k_\mathrm{a}}{D}\left[2P(x) - 1\right] g(\alpha), \qquad \int_0^1 \left(k_\mathrm{a} g(\alpha) + \alpha\right)\, dx = 1, \tag{A.1}$$

where $g(\alpha)$ is either the saturated binding model (2.34) or the Hill function (2.47). To reformulate (A.1), define $N(x)$ by

$$N(x) \equiv \int_0^x \left(k_\mathrm{a} g[\alpha(\eta)] + \alpha(\eta)\right)\, d\eta - 1. \tag{A.2}$$

Then, (A.1) is equivalent to the ODE system

$$\frac{d\alpha}{dx} = \frac{k_\mathrm{a}}{D}\left[2P(x) - 1\right] g(\alpha), \qquad \frac{dN}{dx} = k_\mathrm{a} g(\alpha) + \alpha, \tag{A.3}$$

with $N(0) = -1$. In order to find a solution $\alpha(x)$ that satisfies (A.1), it is necessary to find $\alpha(0)$ such that when the initial value problem (IVP) for $\alpha(x)$ is solved, $N(1) = 0$. Specify $\alpha(0) = \beta$, where β is a value to be determined. Next, solve the IBVPs (A.3) for various values of β and output the quantity $N(1;\beta)$. In this numerical shooting procedure, Newton's method on β is then used to satisfy the required terminal constraint $N(1;\beta) = 0$. Once this β is found, the steady-state solution $\alpha(x)$ can be calculated by solving the IVP with the initial condition $\alpha(0) = \beta$.

A similar approach can be used to compute steady-state solutions of the QSS PDE (2.53) for the **kinesin-dynein model** of §2.4.2 subject to the total mass constraint $\int_0^1 y(x)\,dx = 1$. In place of (A.3), obtain

$$\frac{d\alpha}{dx} = -\frac{k_\mathrm{a}}{D}\frac{[v(k\alpha+1-Q)-Q]}{(k\alpha+1-Q)^2+Q(1-Q)}\,(k\alpha+1-Q)\,\alpha, \qquad \frac{dN}{dx} = \left(1+\frac{1}{k_\mathrm{a}}\right)\frac{(k\alpha+1)\alpha}{k\alpha+1-Q}, \tag{A.4}$$

with $N(0) = -1$ and $\alpha(0) = \beta$. As before, β is a shooting parameter determined numerically by satisfying the terminal constraint $N(1;\beta) = 0$.

Finally, we consider steady-state solutions of the QSS PDE (2.67a) for the **myosin model** of §2.4.3 subject to the total mass constraint $\int_0^1 y(x)\,dx = 1$. In place of (A.3), obtain

$$\frac{d\alpha}{dx} = -\frac{k_\mathrm{b}}{D}\frac{\left(vk_\mathrm{bw}\alpha^2-1\right)}{k_\mathrm{bw}\alpha^2-1}\alpha, \qquad \frac{dN}{dx} = \frac{(k_\mathrm{b}+1)}{k_\mathrm{b}k_\mathrm{bw}}\frac{(k_\mathrm{bw}\alpha^2+1)}{\alpha}, \tag{A.5}$$

with $N(0) = -1$ and $\alpha(0) = \beta$, again where β is computed numerically to satisfy the constraint $N(1;\beta) = 0$. A steady-state solution exists only when $k_\mathrm{bw}\alpha^2 > 1$ on $0 \le x \le 1$.

To numerically determine the boundary in parameter space where $k_\mathrm{bw}\alpha^2 > 1$ holds on $0 \le x \le 1$ for the steady-state when $0 < v < 1$, it is convenient to reformulate (A.5). Define $A(x) \equiv \sqrt{k_\mathrm{bw}}\alpha(x)$ to transform (A.5) to

$$\frac{dA}{dx} = -c_1\frac{\left(vA^2-1\right)}{A^2-1}A\,, \qquad \frac{dN}{dx} = c_2\frac{\left(A^2+1\right)}{A}\,, \qquad \text{where} \qquad c_1 \equiv \frac{k_\mathrm{b}}{D}\,, \qquad c_2 \equiv \frac{k_\mathrm{b}+1}{k_\mathrm{b}\sqrt{k_\mathrm{bw}}}\,. \tag{A.6}$$

A steady-state solution to the QSS PDE exists only when $A(x) > 1$ on $0 \le x \le 1$. Since (A.6) implies that $A(x)$ is monotonic in x whenever $A > 1$, then it is possible that $A \to 1^+$ only for $x \to 0^+$ or $x \to 1^-$. However, since $A \to 1/\sqrt{v} > 1$ on the infinite line as $x \to \infty$, it follows that $A \to 1^+$ as $x \to 0^+$. To determine the local behaviour as $A \to 1^+$ and $x \to 0^+$, note that (A.6) implies $dA/dx \sim c_1(1-v)/[2(A-1)]$ and $dN/dx \sim 2c_2$. This yields the local behaviour

$$A \sim 1 + \sqrt{c_1(1-v)x}, \qquad N \sim -1 + 2c_2x, \qquad \text{as} \quad x \to 0^+. \tag{A.7}$$

For a fixed v and $D > 0$, with $0 < v < 1$, the region in the parameter space k_bw versus k_b where $A(x) > 1$ on $0 \le x \le 1$, is determined as follows. Fix c_1 in (A.6), numerically integrate the IBVPs (A.6) with the local behavior (A.7) imposed at some $x = \delta$, with $0 < \delta \ll 1$, and numerically shoot on the value of c_2 for which $N(1;c_2) = 0$. From (A.6), this determines k_b and k_bw as $k_\mathrm{b} = c_1D$ and $k_\mathrm{bw} = [(k_\mathrm{b}+1)/(k_\mathrm{b}c_2)]^2$.

A.3 Microtubule Density and Binding by Motor Complexes

A.3.1 Kinesin Model with Nonuniform MT Density

To explicitly incorporate the possibility that MT density, $m(x)$ (as well as fraction of MT pointing to the right, $P(x)$) varies across the cell, it is possible to write the kinesin-model equations as

$$\frac{\partial p^{\mathrm{R}}}{\partial t} = -v\frac{\partial p^{\mathrm{R}}}{\partial x} + P(x)k_{\mathrm{bm}}m(x)g(p^{\mathrm{U}}) - k_{\mathrm{u}}p^{\mathrm{R}}, \tag{A.8a}$$

$$\frac{\partial p^{\mathrm{L}}}{\partial t} = v\frac{\partial p^{\mathrm{L}}}{\partial x} + (1-P(x))k_{\mathrm{bm}}m(x)g(p^{\mathrm{U}}) - k_{\mathrm{u}}p^{\mathrm{L}}, \tag{A.8b}$$

$$\frac{\partial p^{\mathrm{U}}}{\partial t} = D_0\frac{\partial^2 p^{\mathrm{U}}}{\partial x^2} - k_{\mathrm{bm}}m(x)g(p^{\mathrm{U}}) + k_{\mathrm{u}}p^{\mathrm{R}} + k_{\mathrm{u}}p^{\mathrm{L}}. \tag{A.8c}$$

This modification of the model introduces another factor into coefficients that are already spatially-dependent, but otherwise leaves the model structure unchanged. Hence, the techniques in the paper apply as before with $k_{\mathrm{bm}}m(x)$ replacing the parameter k_{b}.

For the purposes of the proof-of-concept QSS reduction, now restrict attention to uniform MT density so that $m(x) \equiv m_0$ is a constant. Then the model for kinesin is given by (A.9) as below, with the assignment

$$k_{\mathrm{b}} = k_{\mathrm{bm}}m_0.$$

That is, the binding constant k_{b} is understood to represent the net rate of binding, which includes both the per-MT-binding rate and the MT density.

A.3.2 Kinesin-Dynein Model and the Function $Q(x)$

The kinesin-dynein model simplifies the binding of free motor complexes into states that move right with probability $Q(x)$, and left with probability $1-Q(x)$. I consider the case of motor complexes that all have n_k kinesin and n_d dynein components (the case of complexes with a variety of motor numbers can be handled by considering the mean composition of a complex or the mean ratio between the two motor types). Also define the parameters k_{bd} and k_{bk} as the binding rates for a (single) dynein and for a (single) kinesin to a MT, and consider $m(x)$ as the local MT density. Then the quantity $k_{\mathrm{b}}Q$ in the model can be decomposed as follows:

$$k_{\mathrm{b}}Q(x) = m(x)\left[P(x)n_k k_{bk} + (1-P(x))n_d k_{bd}\right].$$

This relates the aggregate binding rate to the probability that a kinesin binds to right-pointing MT and that dynein binds to left-pointing MT. Similarly,

$$k_{\mathrm{b}}(1-Q(x)) = m(x)\left[(1-P(x))n_k k_{bk} + P(x)n_d k_{bd}\right].$$

Since such details merely substitute one spatially-dependent function for another, the QSS analysis previously described carries over as before.

A.4 Scaling the QSS Models

In this section, details of the scaling of the molecular motor transport models is presented.

A.4.1 The Kinesin Model

Consider the kinesin model with uniform MT density. This system is

$$\frac{\partial p^{\mathrm{R}}}{\partial t} = -v\frac{\partial p^{\mathrm{R}}}{\partial x} + Pk_{\mathrm{b}}g(p^{\mathrm{U}}) - k_{\mathrm{u}}p^{\mathrm{R}}, \tag{A.9a}$$

$$\frac{\partial p^{\mathrm{L}}}{\partial t} = v\frac{\partial p^{\mathrm{L}}}{\partial x} + (1-P)k_{\mathrm{b}}g(p^{\mathrm{U}}) - k_{\mathrm{u}}p^{\mathrm{L}}, \tag{A.9b}$$

$$\frac{\partial p^{\mathrm{U}}}{\partial t} = D_0\frac{\partial^2 p^{\mathrm{U}}}{\partial x^2} - k_{\mathrm{b}}g(p^{\mathrm{U}}) + k_{\mathrm{u}}p^{\mathrm{R}} + k_{\mathrm{u}}p^{\mathrm{L}}. \tag{A.9c}$$

Define T to the total amount of motors inside the cell:

$$T \equiv \int_0^{L_0} \left(p^{\mathrm{R}}(x) + p^{\mathrm{L}}(x) + p^{\mathrm{U}}(x)\right)\, dx \equiv \int_0^{L_0} y(x)\, dx,$$

and $\rho = T/L_0$ to be the average density of motors in the cell.

Scale space, time, and densities as follows:

$$x^\star = \frac{x}{L_0}, \quad t^\star = \frac{tv}{L_0}, \quad p^{J\star} = \frac{p^J}{\rho}, \quad y^\star = \frac{y}{\rho}$$

where $y^\star = p^{\mathrm{R}\star} + p^{\mathrm{L}\star} + p^{\mathrm{U}\star}$ is the total scaled density. Here, distance has been scaled by the cell length and time by the time that a motor takes to walk across the cell. The densities of motors in each state is scaled by the average motor density across the cell.

With this scaling, the total amount of motors is

$$T = \int_0^1 \left(\rho p^{\mathrm{R}\star}(x^\star) + \rho p^{\mathrm{L}\star}(x^\star) + \rho p^{\mathrm{U}\star}(x^\star)\right) d(L_0 x^\star).$$

Taking out the constant factor of $\rho L_0 \equiv T$ from the integral results in

$$T = \rho L_0 \int_0^1 \left(p^{\mathrm{R}\star}(x^\star) + p^{\mathrm{L}\star}(x^\star) + p^{\mathrm{U}\star}(x^\star) \right) dx^\star,$$

which leads to

$$\int_0^1 y^\star dx^\star = \int_0^1 \left(p^{\mathrm{R}\star}(x^\star) + p^{\mathrm{L}\star}(x^\star) + p^{\mathrm{U}\star}(x^\star) \right) dx^\star = 1.$$

With this scaling, the integral of the total scaled density is unity, which is assumed throughout the numerical computations above.

Substituting the scaled variables into the PDE system (A.9) leads to

$$\frac{v}{L_0}\frac{\partial(\rho p^{\mathrm{R}\star})}{\partial t^\star} = \frac{-v}{L_0}\frac{\partial(\rho p^{\mathrm{R}\star})}{\partial x^\star} + k_{\mathrm{u}}\left(P(x)\frac{k_{\mathrm{b}}}{k_{\mathrm{u}}} g(\rho p^{\mathrm{U}\star}) - (\rho p^{\mathrm{R}\star}) \right), \tag{A.10a}$$

$$\frac{v}{L_0}\frac{\partial(\rho p^{\mathrm{L}\star})}{\partial t^\star} = \frac{v}{L_0}\frac{\partial(\rho p^{\mathrm{L}\star})}{\partial x^\star} + k_{\mathrm{u}}\left((1-P(x))\frac{k_{\mathrm{b}}}{k_{\mathrm{u}}} g(\rho p^{\mathrm{U}\star}) - (\rho p^{\mathrm{L}\star}) \right), \tag{A.10b}$$

$$\frac{v}{L_0}\frac{\partial(\rho p^{\mathrm{U}\star})}{\partial t^\star} = \frac{D_0}{L_0^2}\frac{\partial^2(\rho p^{\mathrm{U}\star})}{\partial x^{\star 2}} + k_{\mathrm{u}}\left(\rho p^{\mathrm{R}\star} + \rho p^{\mathrm{L}\star} - \frac{k_{\mathrm{b}}}{k_{\mathrm{u}}} g(\rho p^{\mathrm{U}\star}) \right). \tag{A.10c}$$

This leads to two cases, depending on whether the function g is linear or not.

Case I: g is linear. In this case, it is possible to eliminate the factor ρ from every term. Dividing each term in the equations by $v\rho/L_0$ and dropping the stars leads to

$$\frac{\partial p^{\mathrm{R}}}{\partial t} = -\frac{\partial p^{\mathrm{R}}}{\partial x} + \frac{1}{\varepsilon}\left(P(x) k_{\mathrm{a}} p^{\mathrm{U}} - p^{\mathrm{R}} \right), \tag{A.11a}$$

$$\frac{\partial p^{\mathrm{L}}}{\partial t} = \frac{\partial p^{\mathrm{L}}}{\partial x} + \frac{1}{\varepsilon}\left((1-P(x)) k_{\mathrm{a}} p^{\mathrm{U}} - p^{\mathrm{L}} \right), \tag{A.11b}$$

$$\frac{\partial p^{\mathrm{U}}}{\partial t} = D\frac{\partial^2 p^{\mathrm{U}}}{\partial x^2} + \frac{1}{\varepsilon}\left(p^{\mathrm{R}} + p^{\mathrm{L}} - k_{\mathrm{a}} p^{\mathrm{U}} \right), \tag{A.11c}$$

where D, ε, and k_{a} are defined by

$$D \equiv \frac{D_0}{vL_0}, \qquad \varepsilon \equiv \frac{v}{L_0 k_{\mathrm{u}}}, \qquad k_{\mathrm{a}} \equiv \frac{k_{\mathrm{b}}}{k_{\mathrm{u}}}. \tag{A.12}$$

In this case, these dimensionless parameters represent, respectively, the ratio of (time to be transported : time to diffuse) across the cell (D), the ratio of (time spent unbound : time to walk) across the cell (ε), and the ratio of (time spent unbound : time spent bound) (k_{a}).

Case II: g is Michaelian or Hill. In this case,

$$g(p) = g_{\mathrm{m}} \frac{p^n}{K^n + p^n}, \quad n = 1, 2, \ldots.$$

Then, (A.10) becomes

$$\frac{v}{L_0}\frac{\partial(\rho p^{\mathrm{R}\star})}{\partial t^\star} = \frac{-v}{L_0}\frac{\partial(\rho p^{\mathrm{R}\star})}{\partial x^\star} + k_{\mathrm{u}}\left(P(x)\frac{k_{\mathrm{b}}}{k_{\mathrm{u}}}\frac{g_{\mathrm{m}}(\rho p^{\mathrm{U}\star})^n}{[K^n + (\rho p^{\mathrm{U}\star})^n]} - (\rho p^{\mathrm{R}\star})\right), \tag{A.13a}$$

$$\frac{v}{L_0}\frac{\partial(\rho p^{\mathrm{L}\star})}{\partial t^\star} = \frac{v}{L_0}\frac{\partial(\rho p^{\mathrm{L}\star})}{\partial x^\star} + k_{\mathrm{u}}\left((1-P(x))\frac{k_{\mathrm{b}}}{k_{\mathrm{u}}}\frac{g_{\mathrm{m}}(\rho p^{\mathrm{U}\star})^n}{[K^n + (\rho p^{\mathrm{U}\star})^n]} - (\rho p^{\mathrm{L}\star})\right), \tag{A.13b}$$

$$\frac{v}{L_0}\frac{\partial(\rho p^{\mathrm{U}\star})}{\partial t^\star} = \frac{D_0}{L_0^2}\frac{\partial^2(\rho p^{\mathrm{U}\star})}{\partial x^{\star 2}} + k_{\mathrm{u}}\left(\rho p^{\mathrm{R}\star} + \rho p^{\mathrm{L}\star} - \frac{k_{\mathrm{b}}}{k_{\mathrm{u}}}\frac{g_{\mathrm{m}}(\rho p^{\mathrm{U}\star})^n}{[K^n + (\rho p^{\mathrm{U}\star})^n]}\right). \tag{A.13c}$$

Define a new constant $A \equiv K/\rho$. This constant is the ratio of the motor concentration at which the binding rate is half-maximal to the average motor density in the cell. Divide numerator and denominator of the Hill function by ρ^n. Further, divide every term in the equations by $v\rho/L_0$ as before. After rearranging and dropping the starred notation, obtain

$$\frac{\partial p^{\mathrm{R}}}{\partial t} = -\frac{\partial p^{\mathrm{R}}}{\partial x} + \frac{1}{\varepsilon}\left(P(x)k_{\mathrm{a}}\frac{(p^{\mathrm{U}})^n}{[A^n + (p^{\mathrm{U}})^n]} - p^{\mathrm{R}}\right), \tag{A.14a}$$

$$\frac{\partial p^{\mathrm{L}}}{\partial t} = \frac{\partial p^{\mathrm{L}}}{\partial x} + \frac{1}{\varepsilon}\left((1-P(x))k_{\mathrm{a}}\frac{(p^{\mathrm{U}})^n}{[A^n + (p^{\mathrm{U}})^n]} - p^{\mathrm{L}}\right), \tag{A.14b}$$

$$\frac{\partial p^{\mathrm{U}}}{\partial t} = D\frac{\partial^2 p^{\mathrm{U}}}{\partial x^2} + \frac{1}{\varepsilon}\left(p^{\mathrm{R}} + p^{\mathrm{L}} - k_{\mathrm{a}}\frac{(p^{\mathrm{U}})^n}{[A^n + (p^{\mathrm{U}})^n]}\right), \tag{A.14c}$$

where D and ε are as before, but k_{a} now depends on whether g is a Michaelis-Menten or a Hill function. This holds for any Hill coefficient n. Note that, in particular, for the case $n = 1$, which is the Michaelian case considered,

$$\frac{\partial p^{\mathrm{R}}}{\partial t} = -\frac{\partial p^{\mathrm{R}}}{\partial x} + \frac{1}{\varepsilon}\left(P(x)k_{\mathrm{a}}\frac{p^{\mathrm{U}}}{[1 + cp^{\mathrm{U}}]} - p^{\mathrm{R}}\right), \tag{A.15a}$$

$$\frac{\partial p^{\mathrm{L}}}{\partial t} = \frac{\partial p^{\mathrm{L}}}{\partial x} + \frac{1}{\varepsilon}\left((1-P(x))k_{\mathrm{a}}\frac{p^{\mathrm{U}}}{[1 + cp^{\mathrm{U}}]} - p^{\mathrm{L}}\right), \tag{A.15b}$$

$$\frac{\partial p^{\mathrm{U}}}{\partial t} = D\frac{\partial^2 p^{\mathrm{U}}}{\partial x^2} + \frac{1}{\varepsilon}\left(p^{\mathrm{R}} + p^{\mathrm{L}} - k_{\mathrm{a}}\frac{p^{\mathrm{U}}}{[1 + cp^{\mathrm{U}}]}\right), \tag{A.15c}$$

where $c \equiv 1/A = \rho/K$. In (A.14) and (A.15) k_{a} is defined by

$$k_{\mathrm{a}} \equiv \frac{k_{\mathrm{b}} g_{\mathrm{m}}}{k_{\mathrm{u}}\rho} \quad \text{(Hill)}, \qquad k_{\mathrm{a}} \equiv \frac{k_{\mathrm{b}} g_{\mathrm{m}}}{k_{\mathrm{u}} K}, \quad \text{(Michaelis-Menten)}. \tag{A.16}$$

In either case, the parameter k_{a} describes the ratio of time spent bound to the time spent unbound, mediated by the nonlinear binding kinetics.

Finally, scale the boundary conditions in (2.5) to get

$$\left(p^{\mathrm{R}} - p^{\mathrm{L}} - D\frac{\partial p^{\mathrm{U}}}{\partial x}\right)\Big|_{x=0,1} = 0, \tag{A.17}$$

together with

$$p^{\mathrm{R}}(0,t) = 0 \qquad \text{and} \qquad p^{\mathrm{L}}(1,t) = 0. \tag{A.18}$$

A.4.2 Kinesin-Dynein Model Scaling

Define $k_{\mathrm{c}} \equiv k_{\mathrm{rl}} - k_{\mathrm{lr}}$. Then the model can be written as

$$\frac{\partial p^{\mathrm{R}}}{\partial t} = -v_{\mathrm{r}}\frac{\partial p^{\mathrm{R}}}{\partial x} + k_{\mathrm{b}}Qp^{\mathrm{U}} - k_{\mathrm{u}}p^{\mathrm{R}} - k_{\mathrm{c}}p^{\mathrm{R}}p^{\mathrm{L}}, \tag{A.19a}$$

$$\frac{\partial p^{\mathrm{L}}}{\partial t} = v_{\mathrm{l}}\frac{\partial p^{\mathrm{L}}}{\partial x} + k_{\mathrm{b}}(1-Q)p^{\mathrm{U}} - k_{\mathrm{u}}p^{\mathrm{L}} + k_{\mathrm{c}}p^{\mathrm{R}}p^{\mathrm{L}}, \tag{A.19b}$$

$$\frac{\partial p^{\mathrm{U}}}{\partial t} = D_0\frac{\partial^2 p^{\mathrm{U}}}{\partial x^2} - k_{\mathrm{b}}p^{\mathrm{U}} + k_{\mathrm{u}}(p^{\mathrm{R}} + p^{\mathrm{L}}). \tag{A.19c}$$

Scale all variables as before. Then terms of the form $(k_{\mathrm{c}}/k_{\mathrm{u}})p^{\mathrm{R}}p^{\mathrm{L}}$ will lead to the form $(k_{\mathrm{c}}/k_{\mathrm{u}})\rho p^{\mathrm{R}\star}\rho p^{\mathrm{L}\star}$, so that what remains, after canceling out a factor of $v_{\mathrm{r}}\rho/L_0$ from every term in each equation, and dropping the starred quantities, is

$$\frac{\partial p^{\mathrm{R}}}{\partial t} = -\frac{\partial p^{\mathrm{R}}}{\partial x} + \frac{1}{\varepsilon}\left(k_{\mathrm{a}}Qp^{\mathrm{U}} - p^{\mathrm{R}} - kp^{\mathrm{R}}p^{\mathrm{L}}\right), \tag{A.20a}$$

$$\frac{\partial p^{\mathrm{L}}}{\partial t} = v\frac{\partial p^{\mathrm{L}}}{\partial x} + \frac{1}{\varepsilon}\left(k_{\mathrm{a}}(1-Q)p^{\mathrm{U}} - p^{\mathrm{L}} + kp^{\mathrm{R}}p^{\mathrm{L}}\right), \tag{A.20b}$$

$$\frac{\partial p^{\mathrm{U}}}{\partial t} = D\frac{\partial^2 p^{\mathrm{U}}}{\partial x^2} + \frac{1}{\varepsilon}\left(p^{\mathrm{R}} + p^{\mathrm{L}} - k_{\mathrm{a}}p^{\mathrm{U}}\right), \tag{A.20c}$$

where the parameters are

$$v \equiv \frac{v_{\mathrm{l}}}{v_{\mathrm{r}}}, \qquad D \equiv \frac{D_0}{v_{\mathrm{r}}L_0}, \qquad \varepsilon \equiv \frac{v_{\mathrm{r}}}{k_{\mathrm{u}}L_0}, \qquad k_{\mathrm{a}} \equiv \frac{k_{\mathrm{b}}}{k_{\mathrm{u}}}, \qquad k \equiv \frac{k_{\mathrm{c}}\rho}{k_{\mathrm{u}}} = \frac{(k_{\mathrm{rl}} - k_{\mathrm{lr}})\rho}{k_{\mathrm{u}}}. \tag{A.21}$$

Here ρ is the average density of motors inside the cell. These dimensionless parameters represent, respectively, the (left:right) walking speed ratio (v), the ratio of (time to be transported : time to diffuse) across the cell (D), the ratio of (time spent unbound : time to walk) across the cell (ε), the ratio of (time spent unbound : time spent bound) (k_{a}), and the turning parameter k, which represents the ratio of (net right-left direction switches : unbinding rate). Note that the average density of motors ρ enters into the turning rate parameter due to the nonlinearity of the model with respect to the turning of motors when

they collide on a MT.

Details of QSS Reduction of Kinesin-Dynein Model

This section provides some details of the QSS reduction of the kinesin-dynein model. Upon setting $f_2 = f_3 = 0$ in (2.48), obtain the two equations

$$kp^{\mathrm{R}}p^{\mathrm{L}} = p^{\mathrm{L}} - k_{\mathrm{a}}(1-Q)p^{\mathrm{U}}, \qquad -k_{\mathrm{a}}p^{\mathrm{U}} + p^{\mathrm{R}} + p^{\mathrm{L}} = 0. \tag{A.22}$$

It is convenient to let p^{L} be the free variable and parameterize the quasi-steady-state in terms of $p^{\mathrm{L}} = \alpha$. By solving (A.22) for p^{R} and p^{U}, the quasi-steady-state solution $\mathbf{p}^0$ as given in (2.50). The non-zero eigenvalues $\lambda_{\pm}$ of the Jacobian of the kinetics satisfy the quadratic equation given in (2.51) and (2.52). A necessary and sufficient condition for $\mathrm{Re}(\lambda_{\pm}) < 0$ is that $\sigma_1 < 0$ and $\sigma_2 > 0$ in (2.52). To establish this result, consider some properties of $H(Q)$ defined in (2.52). First observe that $H(0) = 1$, so that trivially $\sigma_1 < 0$ and $\sigma_2 > 0$ when $Q = 0$. Then, since $H'(Q) = -(1+k\alpha)/(1+k\alpha-Q)^2 < 0$, it follows that $\sigma_1 < 0$ and $\sigma_2 > 0$ on $0 \le Q \le 1$ provided that $\sigma_1 < 0$ and $\sigma_2 > 0$ when $Q = 1$. These inequalities do hold at $Q = 1$, since by using $H(1) = (k\alpha - 1)/(k\alpha)$, one finds that $\sigma_1 = -1 - k_{\mathrm{a}} - k\alpha$ and $\sigma_2 = k\alpha(1 + k_{\mathrm{a}}) > 0$ when $Q = 1$. This proves that $\mathrm{Re}(\lambda_{\pm}) < 0$ for any Q in $0 \le Q \le 1$. As a result, $\mathbf{p}^0$ defined in (2.50) is a slow manifold in the sense of Definition (2.3.1) for any Q in $0 \le Q \le 1$. Finally, by using $\mathbf{p}^0$ and the operator M, as defined in (2.48), in the solvability condition (2.24), the QSS PDE can be derived (2.53).

A.4.3 Myosin Model Scaling

The myosin model is

$$\frac{\partial p^{\mathrm{W}}}{\partial t} = -v_{\mathrm{w}}\frac{\partial p^{\mathrm{W}}}{\partial x} - \hat{k}_{\mathrm{bw}}\left(p^{\mathrm{B}}\right)^2 p^{\mathrm{W}} + \hat{k}_{\mathrm{b}}p^{\mathrm{U}} - k_{\mathrm{u}}p^{\mathrm{W}}, \tag{A.23a}$$

$$\frac{\partial p^{\mathrm{B}}}{\partial t} = v_{\mathrm{b}}\frac{\partial p^{\mathrm{B}}}{\partial x} + \hat{k}_{\mathrm{bw}}\left(p^{\mathrm{B}}\right)^2 p^{\mathrm{W}} - k_{\mathrm{u}}p^{\mathrm{B}}, \tag{A.23b}$$

$$\frac{\partial p^{\mathrm{U}}}{\partial t} = D_{\mathrm{f}}\frac{\partial^2 p^{\mathrm{U}}}{\partial x^2} - \hat{k}_{\mathrm{b}}p^{\mathrm{U}} + k_{\mathrm{u}}(p^{\mathrm{B}} + p^{\mathrm{W}}). \tag{A.23c}$$

Using the scaling as before, the terms $\left(p^{\mathrm{B}}\right)^2 p^{\mathrm{W}}$ will lead to the forms $\left(\rho p^{\mathrm{B}\star}\right)^2 (\rho p^{\mathrm{W}\star})$. This will result in a constant factor ρ^2 that remains after canceling out ρ from all terms in the

equation. As a result, upon dropping the starred quantities,

$$\frac{\partial p^{\mathrm{W}}}{\partial t} = -\frac{\partial p^{\mathrm{W}}}{\partial x} + \frac{1}{\varepsilon}\left(-k_{\mathrm{bw}}\left(p^{\mathrm{B}}\right)^2 p^{\mathrm{W}} + k_{\mathrm{b}} p^{\mathrm{U}} - p^{\mathrm{W}}\right), \tag{A.24a}$$

$$\frac{\partial p^{\mathrm{B}}}{\partial t} = v\frac{\partial p^{\mathrm{B}}}{\partial x} + \frac{1}{\varepsilon}\left(k_{\mathrm{bw}}\left(p^{\mathrm{B}}\right)^2 p^{\mathrm{W}} - p^{\mathrm{B}}\right), \tag{A.24b}$$

$$\frac{\partial p^{\mathrm{U}}}{\partial t} = D\frac{\partial^2 p^{\mathrm{U}}}{\partial x^2} + \frac{1}{\varepsilon}\left(p^{\mathrm{B}} + p^{\mathrm{W}} - k_{\mathrm{b}} p^{\mathrm{U}}\right), \tag{A.24c}$$

where the dimensionless parameters v, D, ε, k_{bw}, and k_{b} are defined by

$$v \equiv \frac{v_{\mathrm{b}}}{v_{\mathrm{w}}}, \qquad D \equiv \frac{D_{\mathrm{f}}}{v_{\mathrm{w}} L_0}, \qquad \varepsilon \equiv \frac{v_{\mathrm{w}}}{k_{\mathrm{u}} L_0}, \qquad k_{\mathrm{bw}} \equiv \frac{\hat{k}_{\mathrm{bw}}\rho^2}{k_{\mathrm{u}}}, \qquad k_{\mathrm{b}} \equiv \frac{\hat{k}_{\mathrm{b}}}{k_{\mathrm{u}}}. \tag{A.25}$$

Recall that ρ is the average density of motors inside the cell. These dimensionless parameters represent, respectively, the bound:walking motor speed ratio (v), the ratio of (time to be transported : time to diffuse) across the cell (D), the ratio of (time spent unbound : time to walk) across the cell (ε), the interaction parameter k_{bw}, which represents the ratio of (net rate of collisions that result in direction change : unbinding rate), and the ratio of (time spent unbound : time spent bound) (k_{b}). Note that the average density of motors ρ enters into the interaction rate parameter due to the nonlinearity of the model with motor-motor interaction.

A.4.4 Non-spatial Myosin Model

In §2.4.3, I seek to determine whether the Type I or Type II QSS PDE better approximates the behaviour of the full myosin system. To understand the behaviour, I study the non-spatial myosin model kinetics through a phase-plane analysis, where the advection and diffusive processes in (A.24) are neglected.

The non-spatial myosin model kinetics are described by the following system of ODEs:

$$\frac{dp^{\mathrm{W}}}{dt} = -k_{\mathrm{bw}}\left(p^{\mathrm{B}}\right)^2 p^{\mathrm{W}} + k_{\mathrm{b}} p^{\mathrm{U}} - p^{\mathrm{W}}, \qquad \frac{dp^{\mathrm{B}}}{dt} = k_{\mathrm{bw}}\left(p^{\mathrm{B}}\right)^2 p^{\mathrm{W}} - p^{\mathrm{B}}, \qquad \frac{dp^{\mathrm{U}}}{dt} = p^{\mathrm{B}} + p^{\mathrm{W}} - k_{\mathrm{b}} p^{\mathrm{U}}, \tag{A.26}$$

where time has been scaled to remove the ε-dependence. Due to conservation of mass, it is possible to write $p^{\mathrm{U}} = 1 - p^{\mathrm{W}} - p^{\mathrm{B}}$. This facilitates the reduction of this system of three equations to a system of two equations:

$$\frac{dp^{\mathrm{W}}}{dt} = -k_{\mathrm{bw}}\left(p^{\mathrm{B}}\right)^2 p^{\mathrm{W}} + k_{\mathrm{b}}\left(1 - p^{\mathrm{W}} - p^{\mathrm{B}}\right) - p^{\mathrm{W}}, \tag{A.27a}$$

$$\frac{dp^{\mathrm{B}}}{dt} = k_{\mathrm{bw}}\left(p^{\mathrm{B}}\right)^2 p^{\mathrm{W}} - p^{\mathrm{B}}. \tag{A.27b}$$

With $k_{\mathrm{bw}} = 25$ and $k_{\mathrm{b}} = 3$, a phase-plane analysis (see Figure A.2) reveals the existence of an unstable manifold which divides the $(p^{\mathrm{W}}, p^{\mathrm{B}})$ plane into two regions. For initial conditions below this unstable manifold, the system converges to a steady-state with $p^{\mathrm{B}} = 0$, but $p^{\mathrm{W}} > 0$, as in Type I QSS. For initial conditions above this unstable manifold, the system converges to a steady-state with $p^{\mathrm{B}} > 0$, as in Type II QSS.

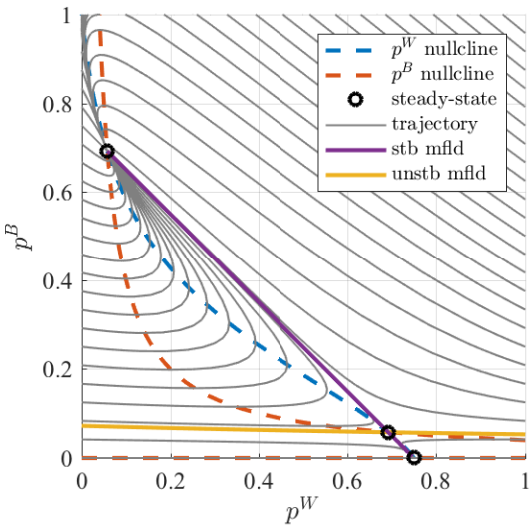

Figure A.2: A phase-plane analysis of the non-spatial myosin model (A.27) reveals the existence of an unstable manifold that divides $(p^{\mathrm{W}}, p^{\mathrm{B}})$ space into two regions. For initial conditions below the unstable manifold, the system tends to a steady-state with $p^{\mathrm{B}} = 0$, but for initial conditions above the unstable manifold, the system tends to a steady-state with $p^{\mathrm{B}} > 0$.

Appendix B

Supporting Materials for Coupling Mechanical Tension and GTPase Signalling to Generate Cell and Tissue Dynamics

B.1 Numerical Methods

Numerical integration of the single cell models and bifurcation analysis was preformed using PyDSTool [13]. Numerical integration of the single-cell and multicellular models was preformed using MATLAB 2017a (The MathWorks, Inc. Natick, Massachusetts, United States). Cellular Potts model simulations were produced with CompuCell3D [90].

B.2 Scaling the GTPase Model

The dynamics of active GTPase are governed by the following differential equation:

$$\frac{dG}{dt} = \left(\hat{b} + \hat{\gamma}\frac{G^n}{G_0^n + G^n}\right)(G_T - G) - \delta G. \tag{B.1}$$

Here, $\hat{b}$ is a basal activation rate, $\hat{\gamma}$ gives the magnitude of the positive feedback upon the activation rate, and G_0 describes the concentration of GTPase at which positive feedback reaches its half-maximal effect. $G_T - G$ gives the total concentration of inactive GTPase.

To reduce the size of parameter space, scale GTPase concentration by the half-max quantity G_0, and scale time by the active GTPase residence time $1/\delta$, respectively. The

equations become

$$\frac{dG}{dt} = \left(b + \gamma \frac{G^n}{1+G^n}\right)(G_T - G) - G. \tag{B.2}$$

The mechanical stimulus term $f(T)$ was added to the activation rate, i.e., I assumed that it operates via a GEF. I considered several forms of mechanical feedback from cell deformation to GTPase activity. Based on the idea that the difference between the current cell "length" L and the current cell "rest-length" L_0 creates the tension that stimulates mechanosensitive pathways, express the feedback in terms of L and L_0. Consequently, I experimented with each of the following forms:

$$\begin{aligned}
f_0(L) &= \beta(L - L_0), && \text{Linear case;}\\
f_1(L) &= \beta \frac{L^m}{L_0^m + L^m}, && \text{Hill function;}\\
f_2(L) &= \beta \frac{1}{1 + \exp[\alpha(L - L_0)]}, && \text{Squashing function;}\\
f_3(L) &= \beta \frac{1}{1 + \exp\left[\alpha \frac{(L-L_0)}{L_0}\right]}, && \text{Strain-dependent squashing function.}
\end{aligned}$$

All four cases share the property that GTPase activation is amplified if $L \gg L_0$. The linear function f_0 has the property that both stretching ($L > L_0$) and compression ($L < L_0$) affect GTPase activation, albeit in opposite ways (stretching increases while compression decreases the GTPase activation rate.) The squashing function f_2 is predominately unidirectional, i.e., only $L > L_0$ has a significant effect, so stretching, but not compressing a cell affects its signalling. This function was used in the minimal model and has the advantage of specifically tracking tension. At the same time, f_1 has a similar effect as f_2, and was to a large extent indistinguishable in the dynamical results obtained (see Appendix Figure B.1(b) for a bifurcation diagram of the single-cell model with the Hill function response f_1). The noticeable difference occurs in the synchronization of large tissue simulations. Compare, for example, the simulation with the squashing function f_2 in Figure 3.5(e) and the simulation with the strain-dependent squashing function f_3 in Appendix Figure B.1(c).

The Hill function and strain-dependent squashing function, f_1 and f_3 have a similar shape for all L and L_0 and are approximately equal for the parameters used herein. The change that f_1 and f_3 can affect in the GTPase activation rate is relative to the current rest-length of the cell L_0. This is different from the squashing function f_2, which assumes a mechanosensing mechanism by which tension can activate GTPase signalling regardless of the current rest length, L_0.

The Rac-Rho mutual inhibition model in Section 3.5 Equation (3.6), is the scaled model. Details of this scaling are similar to scaling for the single GTPase model. The reader is

referred to [33, 34].

B.3 1D Methods: Multicellular Simulations

Equations (3.4) and (3.2a) were implemented in a collection of cells in 1D. Each cell has its own GTPase activity G_j, which is described by Equation (3.2a), with lengths given by $L_j = x_{j+1} - x_j$. Numerical integration was done using MATLAB 2017a (The MathWorks, Inc. Natick, Massachusetts, United States) for all 1D multicellular simulations.

For Figure 3.5(a)-(c), (e), and (f), and B.1(a) and (c), GTPase activity in each cell, G_j, affects the rest length through

$$L_{j,0} = \ell_0 - \phi \frac{G_j^p}{G_h^p + G_j^p}. \tag{B.3}$$

Tension is assumed to affect the GTPase activation rate through the squashing function response to tension (f_2 above, also Equation 3.2b). Parameter values for these simulations are $b = 0.1$, $\gamma = 1.5$, $n = p = 4$, $G_T = 2$, $\alpha = 10$, $\ell_0 = 1$, $\phi = 0.75$, $G_h = 0.3$, $k = 1$, $\lambda = 10$, and β varies. Initial conditions are $L_j(0) = 0.7$ and $G_j(0) = 1$ for the $N = 10$ simulations, and random initial lengths with $G_j(0) = 1$ for all the simulations with $N > 10$ and for the $N = 10$ case with one oscillatory cell, Figure B.1. Instead of the squashing function response to tension (f_2), the strain-dependent squashing function (f_3) was used in Figure B.1(c).

For Figure 3.5(d), we simulated $N = 14$ cells, and assumed linear responses for both GTPase-activation from tension (f_0) and for rest-length from GTPase activity:

$$L_{j,0} = \ell_0 - \phi G_j. \tag{B.4}$$

Initial conditions for this simulation were $L_j(0) = 0.68$, $G_j(0) = 0.45$ for all j with the exception of $G_j(0) = 1.2$ for $j = 13, 14$. Other parameters were $b = 0.3$, $\beta = 0.35$, $\phi = 0.7$, $n = 4$, $G_T = 1.75$, $\ell_0 = 1$, $k = 1$, and $\lambda = 10$.

B.4 2D Methods: Cellular Potts Model

CompuCell3D, an open-source implementation of the cellular Potts model, is used for 2D simulations of the GTPase-tension model [90]. The cellular Potts model is an individual cell-based model where each cell occupies one or more discrete lattice sites. Cells can expand outwards or contract inwards by adding or removing lattice sites at the cell perimeter.

The dynamics of each "cell" is governed by a Hamiltonian energy function, $\mathcal{H}$. The Hamiltonian for the 2D simulation consists of an area constraint term (also called volume

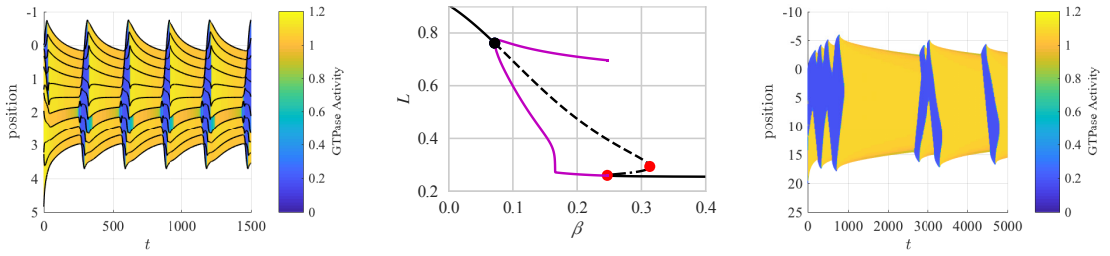

(a) All 10 cells have $\beta = 0.3$ except for one randomly chosen oscillatory cell with $\beta = 0.2$.

(b) Single cell bifurcation diagram with Hill function response from tension $f_1(T)$

(c) $\beta = 0.2$, 50 cells, with GTPase activation rate $f(T) = f_3(T)$.

Figure B.1: Additional 1D tissue dynamics result from mechanochemical interactions. Kymographs show the 1D position of each cell (vertical axis) with color indicating the GTPase activity within each cell. In (a), a single oscillatory cell with $\beta = 0.2$ can induce tissue-level oscillations among a population of contracted cells with $\beta = 0.3$. In (b), single cell dynamics with the Hill function response from tension, $f_1(T)$, qualitatively resemble the dynamics with the squashing function $f_2(T)$. In (c), waves of contraction propagate through the tissue of 50 oscillatory cells with the strain-dependent feedback, f_3. See also SI Movies 10 and 11, for (a) and (c) respectively.

deformation term in a general 3D context) and an adhesion energy term. The area constraint is implemented in terms of a (time-varying) target area. Target area represents the area (number of lattice sites) that each cell would occupy in an optimal lattice configuration. The adhesion energies specify the interactions between different cells and the surrounding medium (extra-cellular space, or "medium"). Additionally, a connectivity constraint is imposed that penalizes the Hamiltonian if lattice sites for each cell do not form a connected domain. This avoids fragmentation of the "cells".

Lattice sites are added or removed from cells in "spin-copy attempts". A spin-copy attempt is accepted if it decreases the overall energy of the system, as defined by the Hamiltonian. A spin-copy attempt is also accepted with a non-zero probability if it results in a small increase in the Hamiltonian. The temperature parameter in the Boltzmann distribution of accepted unfavourable spin-copies controls the degree of exploration of energetically unfavourable lattice configurations. Given N lattice sites, a collection of N spin-copy attempts constitutes one Monte-Carlo step (MCS) of the simulation. The Metropolis algorithm is used to determine the quasi-deterministic kinetics of lattice configurations evolving under the Hamiltonian. While CPM does not explicitly track forces, it has recently been shown to correspond to other vertex-based simulations where forces are made explicit [47].

In the case of single cells, the model parameters are $\tau = 2000$, $b = 0.1$, $m = 10$, $\gamma = 1.5$, $n = p = 4$, $G_T = 2$, $\varepsilon = 0.1$, $a_0 = 400$, $\phi = 0.75$, and $G_h = 0.3$. Single cell simulations ran for 250 MCS, with temperature parameter 30. The cell-cell and cell-medium adhesion

energies are set to 0.1 and 80 in the Hamiltonian $\mathcal{H}$, respectively, and I did not impose a perimeter (surface) constraint. The area constraint parameter in the Hamiltonian $\mathcal{H}$ was set to: $\lambda_A = 1$ and initial conditions were set as $G(0) = 1$, $A_T(0) = 320$, and $A(0) = 320$.

B.5 2D Methods: Patch Size and Synchronization

To explore the idea that adhesion strength could affect the extent of synchrony among the cells in the tissue, I varied the adhesion energy in the Hamiltonian $\mathcal{H}$ among a small tissue of 9 cells, with each cell in the oscillatory regime. Treating the tissue as a system of coupled oscillators and it is possible to numerically quantify the level of synchrony using the Kuramoto order parameter and the variance in the distribution of phase angles of the oscillators. The Kuramoto order parameter describes the degree of synchronization in a collection of coupled oscillators (see [42], or [89] for a review). As adhesion-strength increases, the oscillators are more synchronized, with an apparent increase in the Kuramoto order parameter, and a decrease in variance in the distribution of phase angles. See Figure B.3 and B.5-B.7.

To determine the Kuramoto order parameter for the small tissue, the dominant frequency of each oscillating cell (i.e., frequency with highest magnitude) is determined over time using a sliding window with the real-valued Fourier transform (RFFT). The fixed size window contains time series data roughly equivalent to 3 periods of oscillation. The Kuramoto order parameter and variance in phase is calculated by determining the phase corresponding to the dominant frequency for all nine oscillators.

Model parameters are as in Section B.4, except the initial conditions for cell areas are randomly chosen, initial conditions for GTPase are randomly chosen between 0 and 1 and initial target area is also randomly chosen between 350 and 450.

B.6 2D Methods: Large-Tissue Simulations

A circular tissue consisting of 373 cells with randomly chosen area (and $\beta = 0.2$, corresponding to the oscillatory regime) is used as the initial lattice configuration. Initial target area was set to the initial cell area for each cell. The simulation was carried out for 2000 MCS. Initial target area is set equal to the initial area. Initial GTPase concentration is randomly chosen between 0 and 1. The remaining model parameters are as in Section B.4.

B.7 Additional 2D Results

In this section, some additional 2D CPM simulation results are presented. Model parameters are as before, outlined in Section B.4. Each figure shows 8 snapshots of the cell behaviour, with the colour indicating the GTPase activity. Also shown are the cell area, target area,

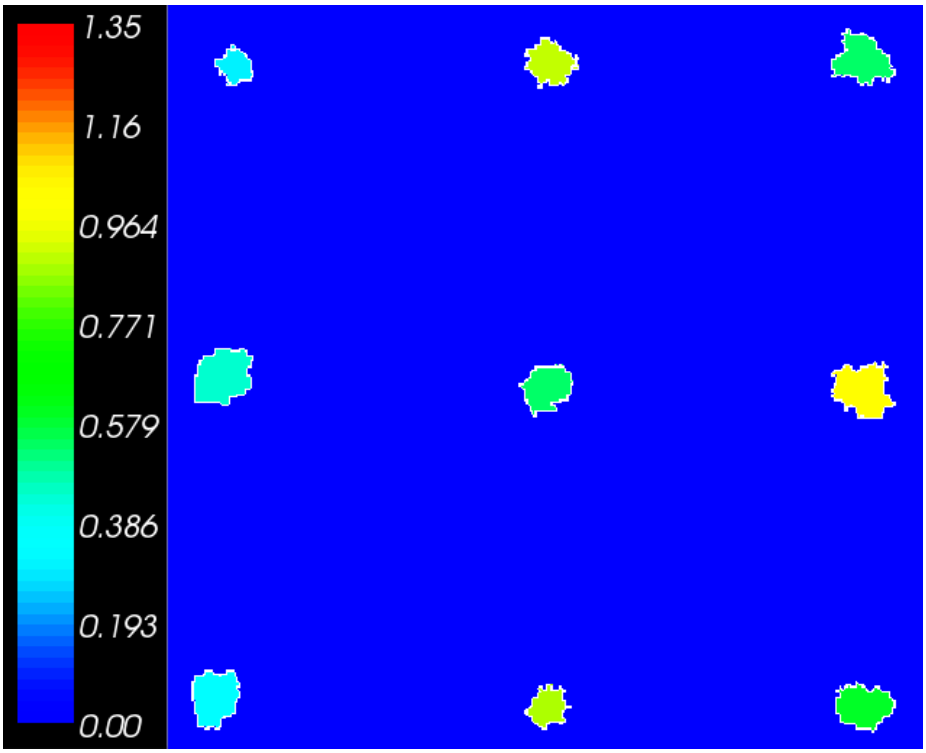

Figure B.2: CPM initial lattice configuration for 9 oscillating cells with no mechanical coupling or adhesion and randomly chosen initial cell area and GTPase activity.

and the GTPase activity over time. These results include:

1. Figure B.8: a single relaxed cell with large constant area and low GTPase activity with $\beta = 0.05$.

2. Figure B.9: damped oscillations occur for $\beta = 0.1$.

3. Figure B.10: a small amplitude limit cycle with $\beta = 0.15$.

4. Figure B.11: stochastic switching between a low amplitude limit cycle and high amplitude limit cycle with $\beta = 0.175$.

Also, a large tissue simulation similar to Figure 3.7 and 3.8 but with weak adhesion is shown in Figure B.12.

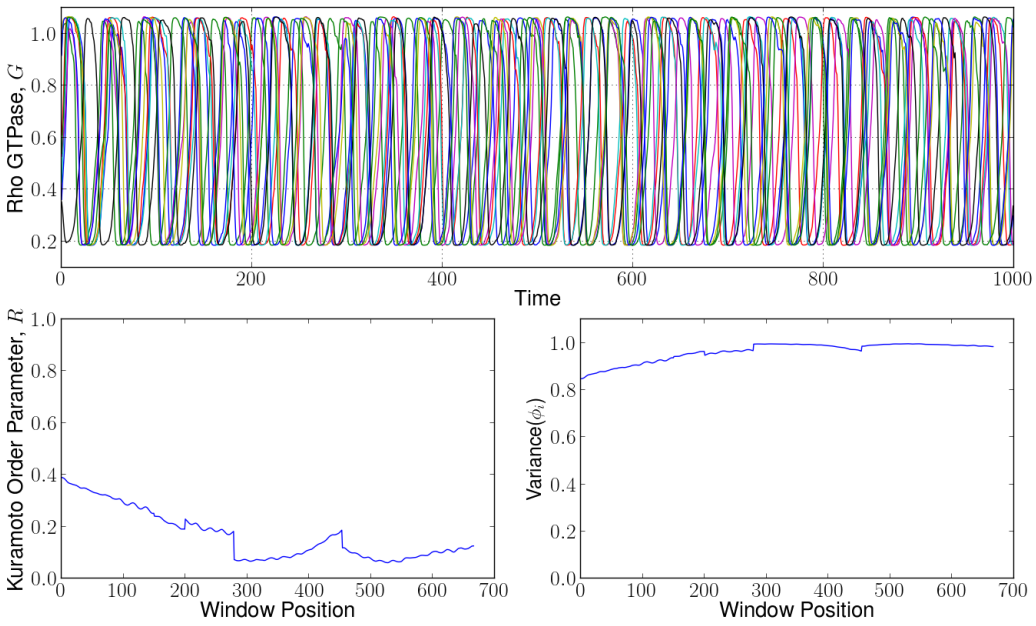

Figure B.3: Time series of GTPase activity, Kuramoto order parameter and variance in phase for 9 independent oscillators shown Figure B.2. Note that initial cell area is equal to initial cell target area, hence initial conditions are not fully randomized. Variance increases with time due to the stochastic nature of spin copy attempts that offset the initial conditions.

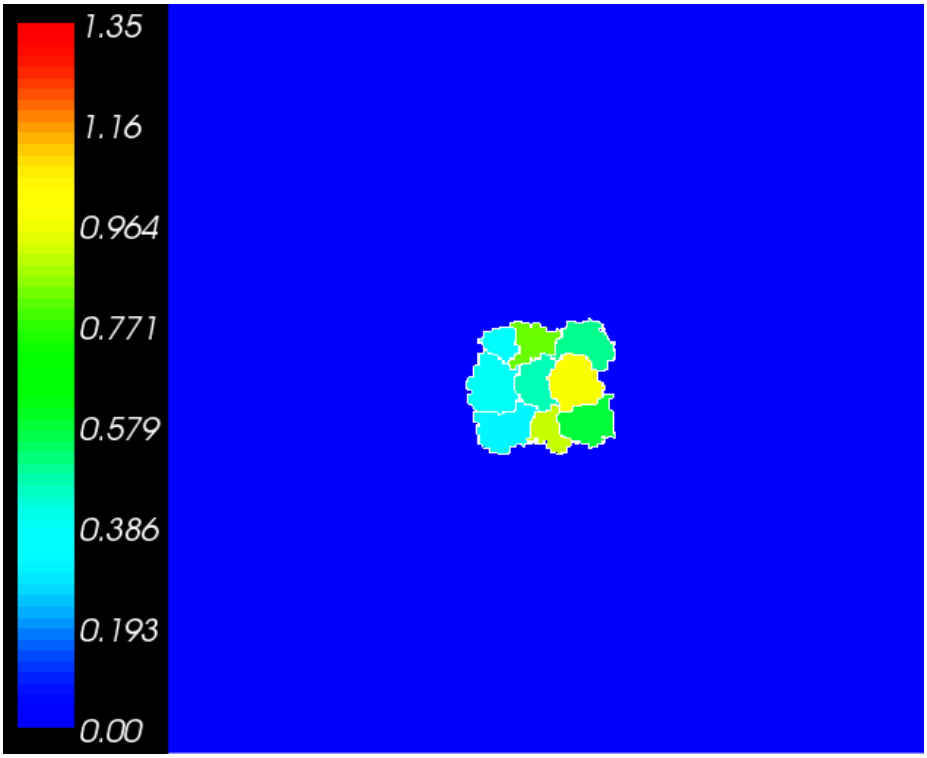

Figure B.4: CPM initial lattice configuration for 9 oscillating mechanically coupled cells with randomly chosen initial cell area and GTPase activity. Each lattice site can only be occupied by one cell and overlap is not allowed. Cell-cell and cell-medium adhesion parameters govern the mechanical interactions of the cells. Strength of adhesion between cells is higher if cell-cell adhesion energy is lower compared to cell-medium adhesion energy, and vice-versa.

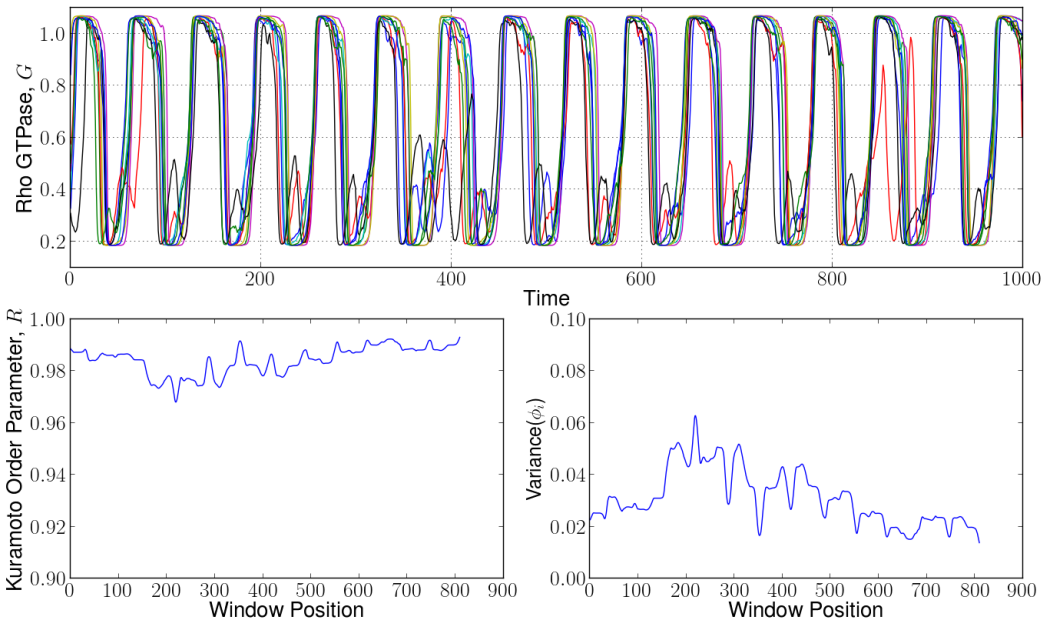

Figure B.5: Synchronized oscillations in the low adhesion regime in a simulation as in Figure B.4 over 1000 Monte Carlo "time steps". Cell-medium adhesion energy (40) is less than cell-cell adhesion energy (80) in the Hamlitonian $\mathcal{H}$. Adhesion strength is low, which implies less entrainment/synchrony.

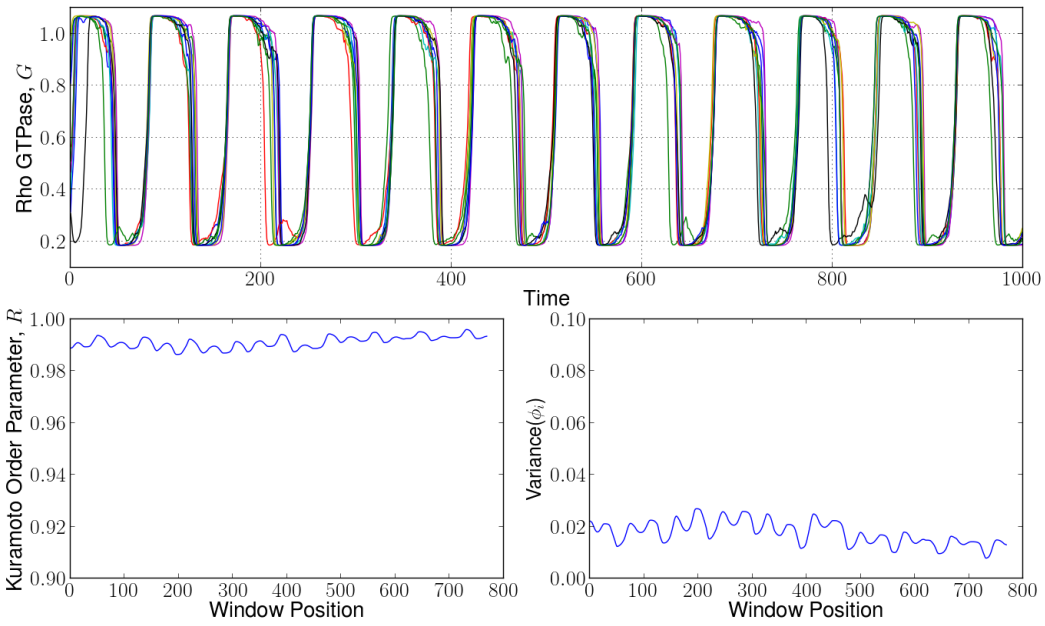

Figure B.6: Synchronization in the intermediate adhesion regime. Cell-medium adhesion energy (80) is equal to cell-cell adhesion energy (80) in the Hamlitonian $\mathcal{H}$.

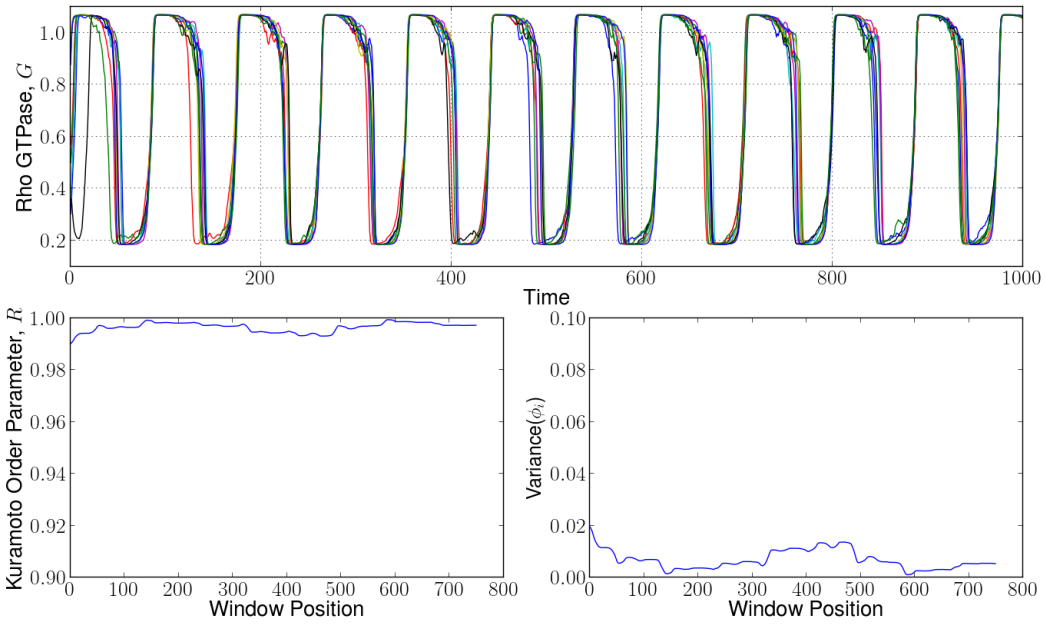

Figure B.7: Synchronization in the high adhesion regime. Cell-cell adhesion energy (60) is less than cell-medium adhesion energy (80) in the Hamlitonian $\mathcal{H}$. This implies high degree of adhesion strength between cells, leading to entrainment.

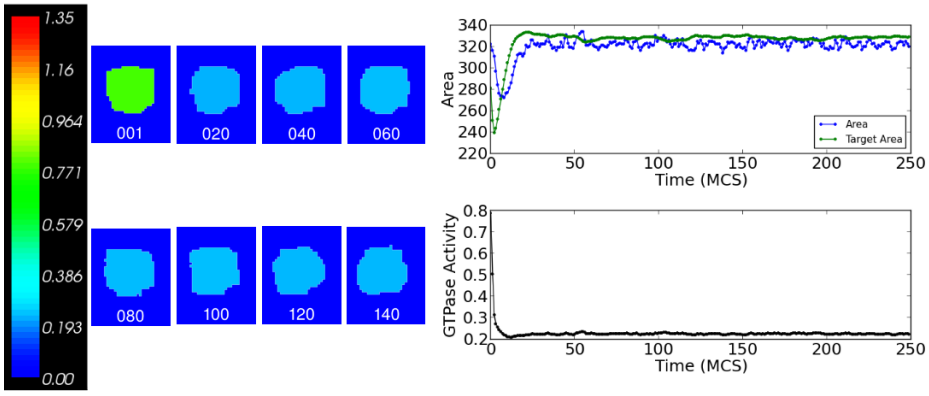

Figure B.8: Relaxed cell with low Rho GTPase activity, $\beta = 0.05$. Cells are coloured by GTPase activity. Cell area, target area, and GTPase activity are plotted over time.

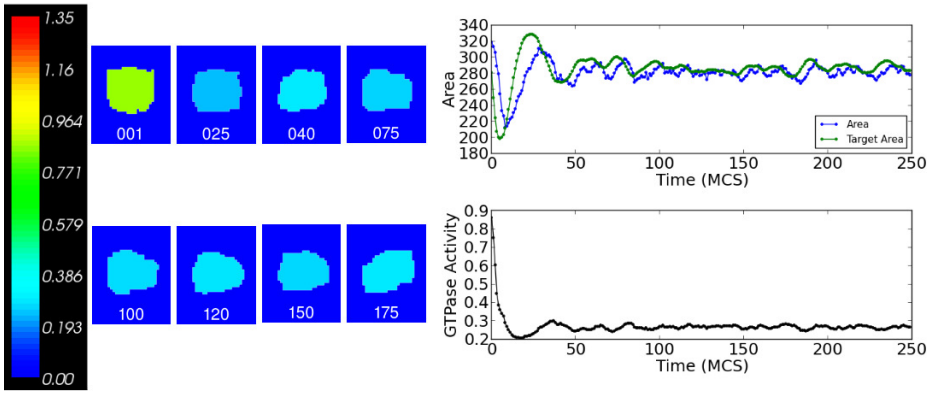

Figure B.9: Damped oscillations for $\beta = 0.1$. Cells are coloured by GTPase activity. Cell area, target area, and GTPase activity are plotted over time.

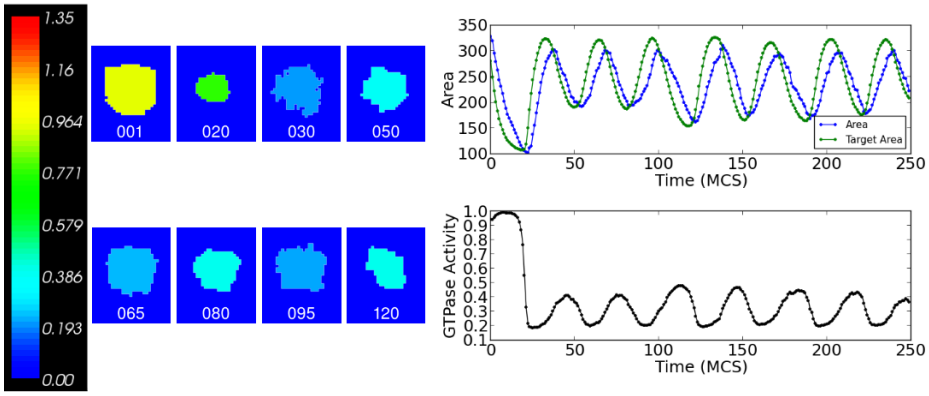

Figure B.10: Small amplitude limit cycle, $\beta = 0.15$. Cells are coloured by GTPase activity. Cell area, target area, and GTPase activity are plotted over time.

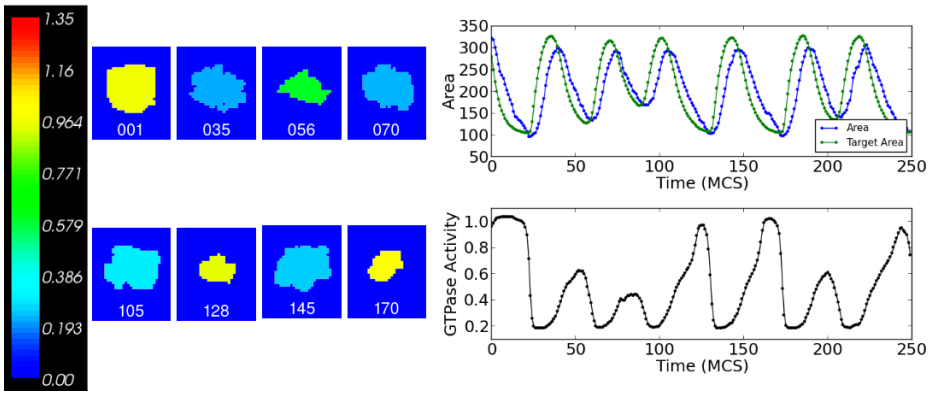

Figure B.11: Stochastic switching between low amplitude limit cycle and high amplitude limit cycle, $\beta = 0.175$. Cells are coloured by GTPase activity. Cell area, target area, and GTPase activity are plotted over time.

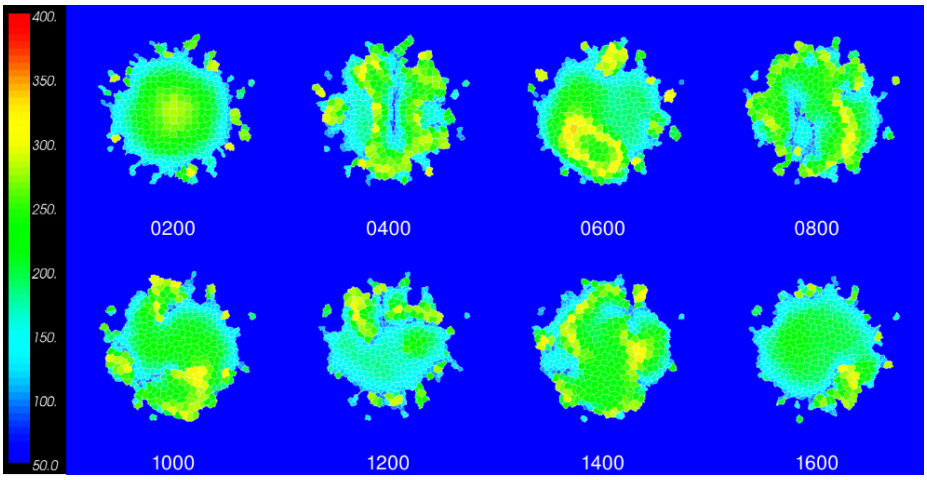

(a) Cell area in a 2D tissue over time.

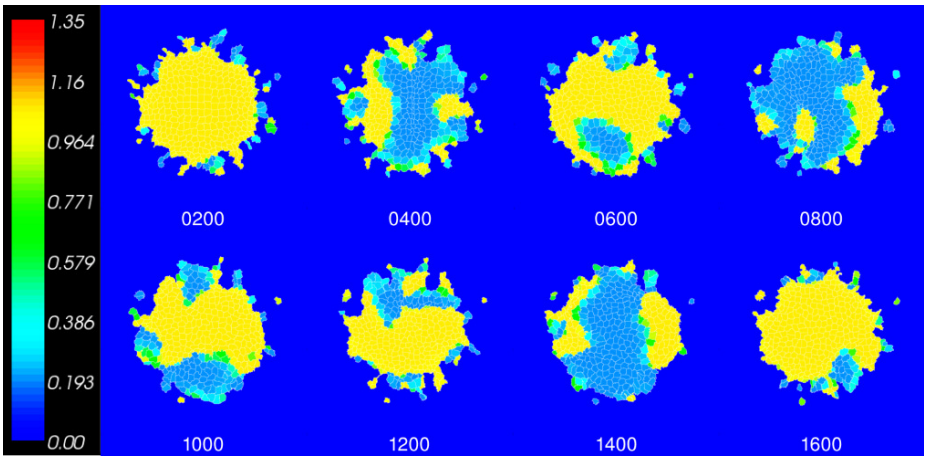

(b) GTPase activity in the same 2D tissue over time.

Figure B.12: As in Figure 3.7, but in the weak adhesion scenario. In (A), cells are coloured based on their current cell area, while in (B), cells are coloured based on the uniform level of GTPase activity within each cell. In the Hamiltonian, $\mathcal{H}$, cell-medium adhesion energy (60) is less than cell-cell adhesion energy (80). Notice that some cells detach from the tissue due to low adhesion strength. Patches of synchronized cell oscillations are still observed.